NASA CR - 165584

NASA-CR-165584
19820012368

NASA

ADVANCED SPACE PROPULSION THRUSTER RESEARCH

PREPARED FOR

LEWIS RESEARCH CENTER

NATIONAL AERONAUTICS AND SPACE ADMINISTRATION

GRANT NGR-06-002-112

Annual Report

December 1981

Paul J. Wilbur
Department of Mechanical Engineering
Colorado State University
Fort Collins, Colorado

1. Report No.	2. Government Accession No.	3. Recipient's Catalog No.
NASA CR 165584		

4. Title and Subtitle	5. Report Date
Advanced Space Propulsion Thruster Research	Dec. 1981
	6. Performing Organization Code

7. Author(s)	8. Performing Organization Report No.
Paul J. Wilbur	
	10. Work Unit No.

9. Performing Organization Name and Address	11. Contract or Grant No.
Department of Mechanical Engineering Colorado State University Fort Collins, Colorado 80523	NGR-06-002-112
	13. Type of Report and Period Covered
12. Sponsoring Agency Name and Address	Dec. 1, 1980 - Dec. 1, 1981
National Aeronautics and Space Administration Washington, D.C. 20546	14. Sponsoring Agency Code

15. Supplementary Notes

Grant Monitor - William Kerslake, NASA Lewis Research Center, Cleveland, Ohio 44135.

16. Abstract

The results of a series of experiments showing that stray magnetic fields can adversly affect the capacity of a hollow cathode neutralizer to couple to an ion beam are presented. The strength of the magnetic field at the neutralizer cathode orifice is proposed as a crucial factor influencing the coupling voltage. The effects of electrostatic accelerator grid aperture diameters on the ion current extraction capabilities are examined experimentally. Experiments describing the divergence, deflection and current extraction capabilities of grids with the screen and accelerator apertures displaced relative to one another are discussed and the results of these experiments are presented. Experiments performed in orificed, mercury hollow cathodes are shown to support the model of field enhanced thermionic electron emission from cathode inserts. Further tests support the validity of a thermal model of the cathode insert that includes the effects of ion heating and electron cooling. A theoretical justification of a Saha equation model relating cathode plasma properties is presented. A series of experiments that suggest ion loss rates to discharge chamber walls can be controlled by adjusting the discharge chamber magnetic field configuration are described. A series of new discharge chamber magnetic field configurations are generated in the flexible magnetic field thruster and their effect on performance is examined. A technique used in this thruster to measure ion currents to discharge chamber walls is described. Using these ion currents the fraction of ions produced that are extracted from the discharge chamber and the energy cost of plasma ions are computed.

17. Key Words (Suggested by Author(s))	18. Distribution Statement
Electrostatic Thruster Hollow Cathode	Unclassified - Unlimited

19. Security Classif. (of this report)	20. Security Classif. (of this page)	21. No. of Pages	22. Price*
Unclassified	Unclassified	156	

* For sale by the National Technical Information Service, Springfield, Virginia 22161

NASA-C-168 (Rev. 10-75)

TABLE OF CONTENTS

Table of Contents (Continued)

LIST OF FIGURES

List of Figures (Continued)

List of Figures (Continued)

LIST OF TABLES

THE INFLUENCE OF STRAY MAGNETIC FIELDS ON ION BEAM NEUTRALIZATION

Feng Yu-Cai

INTRODUCTION

Recent tests conducted in space on the SERT II spacecraft have included investigations of phenomena that were not identified in the original test plan. A particularly interesting one was the experiment in which distant neutralization of an ion beam was accomplished by using the neutralizer or unaccelerated thruster plasmas of a thruster located a meter or so away from the thruster operating at high voltage.[1,2] One of the results observed in this test was that the neutralizer coupling voltage (the difference between the neutralizer and beam plasma potentials) could be lower when the distant neutralizer was used than it was when the local neutralizer was used. This suggests that it is easier to neutralize the ion beam with a distant neutralizer than with a local one, located very close to the ion beam. It is however not immediately clear why the coupling voltage for distant neutralization should be lower. After conducting a theoretical study of this problem Kaufman[3] suggested that the improved coupling with the distant neutralizer was a consequence of stray magnetic fields that directed distant neutralizer electrons into the beam while electrons from the local neutralizer were directed away from it. In order to examine this theory in more detail and develop an understanding of neutralization phenomena that would aid in future neutralizer designs the study described herein was conducted. It is noteworthy that understanding remote neutralization phenomena could also be helpful in designing a neutralizer system composed of a few cathodes neutralizing a large number of thrusters.

This report presents test data comparing the ion beam neutralization characteristics of a local neutralizer (within $\sim$ 5 cm of the beam edge) with those associated with a distant one ($\sim$ 1 meter away). The effects of magnetic fields in the vicinity of both of these neutralizer configurations on their capacity to couple to the ion beam, as reflected in ion beam plasma potential profiles, were studied.

APPARATUS AND PROCEDURE

The experiments were conducted in the 1.2 m diameter by 4.6 m long stainless steel vacuum tank shown schematically in Fig. 1. The operating pressure in the vacuum system was in the range of $5 \sim 7 \times 10^{-6}$ torr during the tests. At this pressure the electron collision frequency is small compared to typical cyclotron frequencies so the conditions of this test should model the collisionless environment of the space tests adequately. Further the vacuum tank plasma was typically several volts above ground, so most neutralizer electrons should be reflected from the tank walls; a condition that also facilitates modelling of the space plasma. The SIT-8 mercury ion thruster[4] identified in Fig. 1 is located at one end of the test facility in such a way that its ion beam is directed along the tank axis. Neutralization of this beam is accomplished by either the standard SIT 8 hollow cathode mercury neutralizer[4] located adjacent to the thruster or by the distant neutralizer shown. The distance neutralizer is also a conventional 0.32 cm dia. mercury hollow cathode. It is equipped with a rolled tantalum foil insert, a 0.04 cm diameter orifice (compared to 0.025 cm for local one) and a toroidal keeper electrode located 0.08 cm downstream of the orifice plate. The distant neutralizer was operated at a mercury flow rate of $\sim$ 60 mA while the local one operated at $\sim$ 12 mA. These were the flow rates where

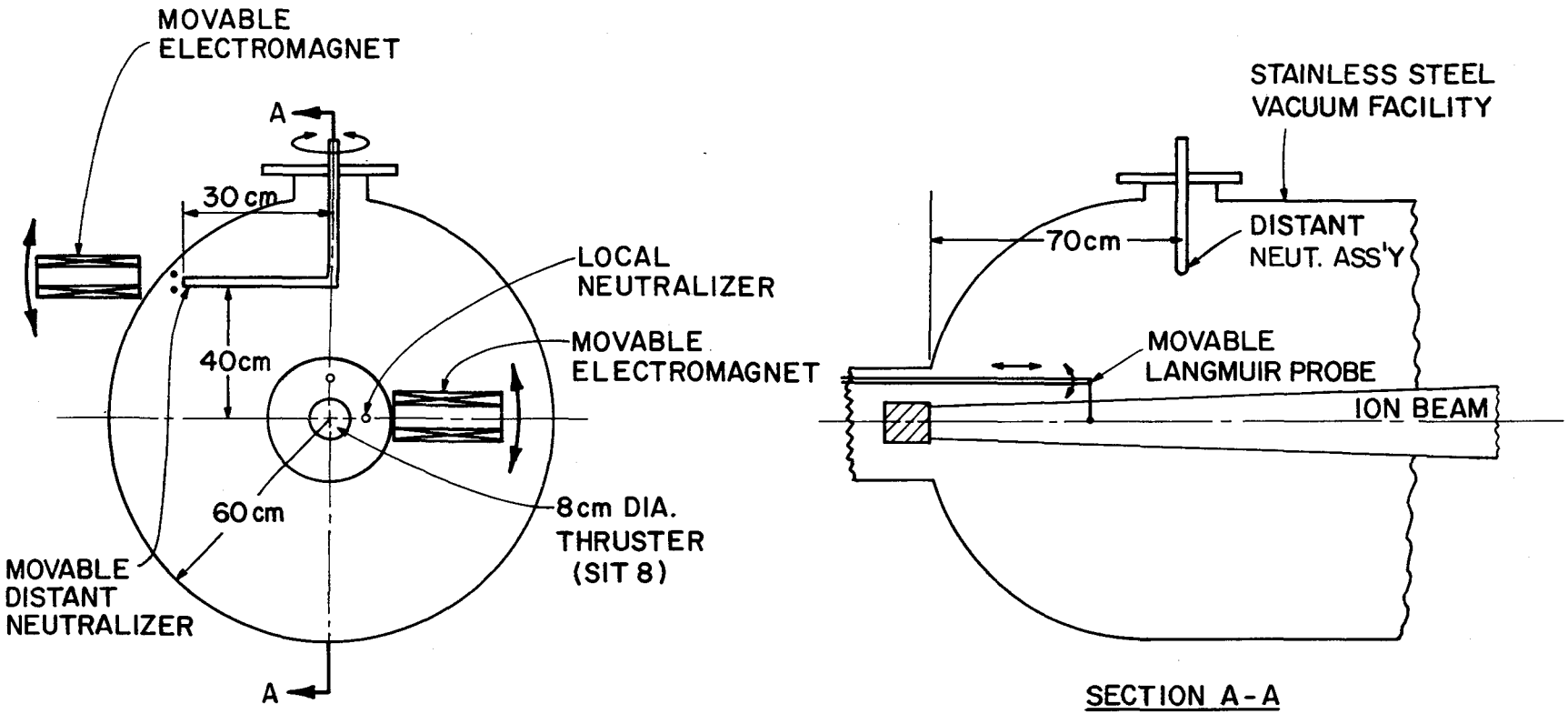

Figure 1. Neutralization Study Test Apparatus.

the neutralizers each seemed to operate well. The lower flow rate was presumably required for the local neutralizer because it had a smaller orifice diameter and because it utilized a closed keeper configuration. The distant neutralizer was attached to a rod passing through the top of the tank as shown in Figure 1. When this rod was rotated the neutralizer moved through a 180° arc from one side of the tank to the other. Because the vacuum tank is stainless steel the influence of the earth's magnetic field is felt within it. This field has a magnitude of $\sim$ 0.5 gauss and is inclined at an angle of 65° from the direction of the ion beam in the plane of Section A-A in Figure 1. Movement of the neutralizer support rod through its 180° travel is sufficient to place the neutralizer at positions where it lies on earth magnetic field lines that intersect the ion beam or miss it by distances up to $\sim$ 30 cm. Both neutralizer cathodes were equipped with power supplies that controlled keeper potential, cathode tip heater current and neutralizer bias potential. Keeper currents for the cathodes were maintained at 0.3 A and the neutralizer bias was adjusted so it was sufficiently negative to effect the neutralizer emission required to match the ion beam current.

Auxiliary magnetic fields of variable magnitude were generated in the experiments by using the two electromagnets shown in Figure 1. These two magnets were located immediately adjacent to the particular neutralizer they served. Both of them could be rotated to change the direction of the magnetic fields they produced. These fields were of the order of 20 gauss at the neutralizer cathodes. During the tests the magnets were rotated in such a way that their axis remained pointed at the cathode tip, i.e., their center of rotation was about the cathode tip.

Evaluation of the effects of parametric variations introduced in the experiments required the measurement of the neutralizer bias voltage, the plasma potential in the beam and magnetic field shapes and magnitudes. The neutralizer bias voltage could be measured directly but the beam plasma potential had to be measured using the Langmuir probe shown schematically in Fig. 1. The probe used was an emissive probe that could be swept through the beam at various axial locations. The details of the probe circuitry are described in Reference 5. The intensities and shapes of magnetic fields were determined using a gaussmeter in conjunction with iron filings maps.

EXPERIMENTAL RESULTS

Neutralization in the Unaltered Environment of the Magnetic Fields of the Thruster and the Earth

Initial investigations into the neutralization of the ion beam were conducted with the electromagnets shown in Figure 1 turned off. The magnetic field in the region between the distant neutralizer and ion beam is in this case the weak one ($\sim$ 0.5 gauss) associated with earth only. In the region between the local neutralizer and ion beam the net magnetic field determined by the thruster and earth magnetic fields was about 18 gauss. At a beam current of 100 mA with the distant neutralizer positioned as shown in Fig. 1, so electrons emitted from it would pass about 30 cm from the beam centerline, the plasma potential profiles represented by the dotted and dashed curves of Figure 2 were observed. During data collection for these curves, the local neutralizer was not operating. When the distant neutralizer was turned off and the local neutralizer was started the higher plasma potentials represented by the solid and center lines were observed at the two axial locations identified. This phenomenon of higher plasma potentials with the local neutralizer also seemed to occur during some of

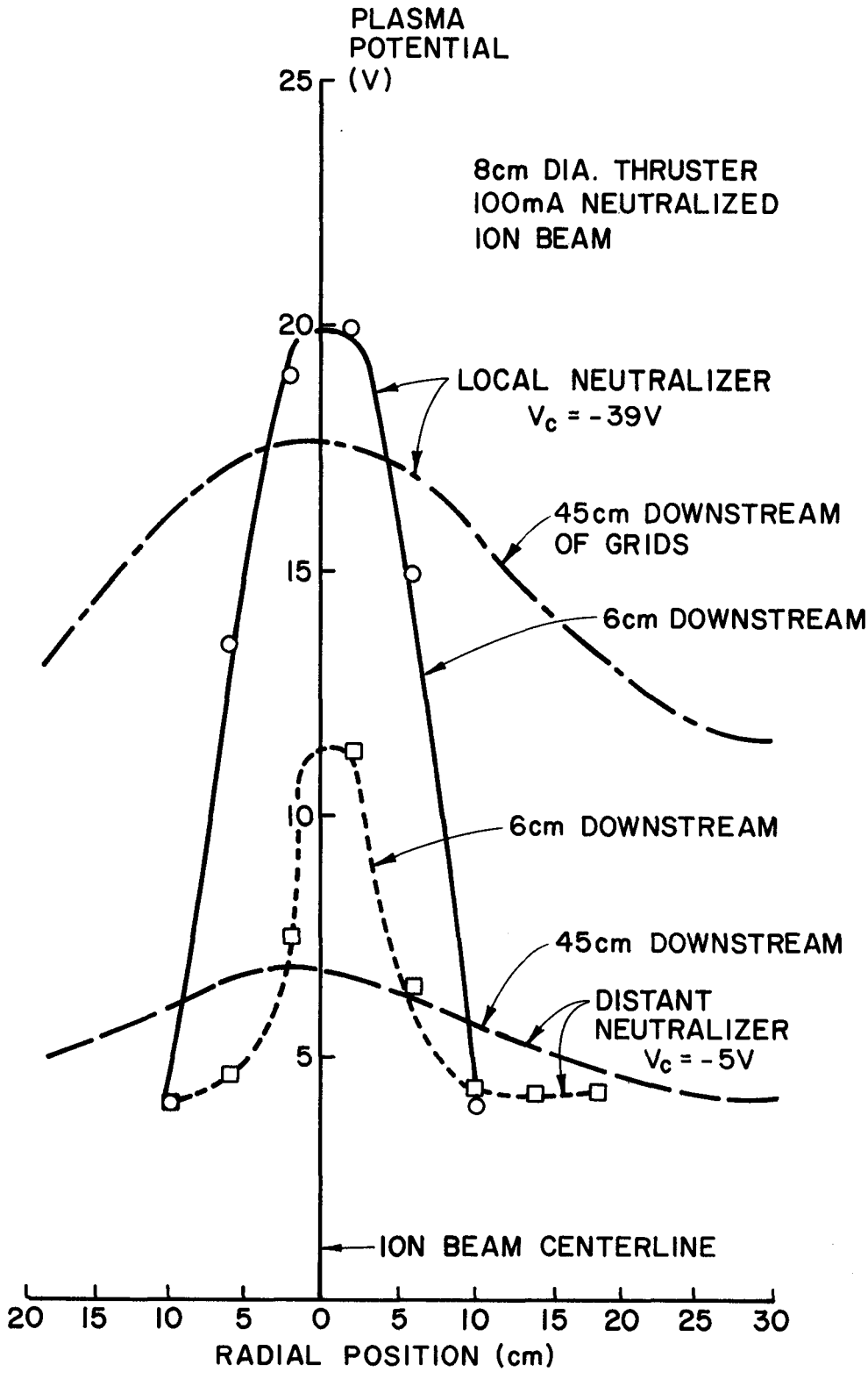

Figure 2. Effect of Neutralizer Location on Ion Beam Plasma Potentials.

the SERT II tests.[1,2] The plasma potential profile at the 6 cm location is also seen to be broader when the local neutralizer is being used, a condition that was also observed in the space tests. Both of these conditions are believed to be manifestations of a resistance between the beam and local neutralizer plasmas that is higher than the one between the distant neutralizer and beam plasmas. This postulate is also supported by the observation that the neutralizer cathode bias voltage (V_c) required to effect neutralization was also considerably lower in magnitude when the distant neutralizer was used.

In a second experiment the local neutralizer was secured, the distant neutralizer was moved with respect to the ion beam while the thruster was operating and the effect of this movement on the ion beam plasma profile was examined. This neutralizer movement was accomplished by rotating the arm supporting the distant neutralizer (Fig. 1) so the neutralizer plasma was moved from the earth magnetic field line missing the ion beam centerline by $\sim$ 30 cm to one passing through the ion beam centerline and the beam potential profiles shown in Fig. 3 were obtained. As indicated on the figure, profiles were measured at axial locations downstream from the grids (x) of 6, 29 and 52 cm. The results shown in this figure are as expected in that the beam plasma potentials dropped when the neutralizer was moved to the field line intercepting the beam axis. The fact that this drop was small ($\sim$ 3 v) could be due to the fact that the neutralizer plasma was not moved very far away from the edge of the beam plasma. In this regard it is noted that 1) the beam plasma potentials suggest substantial beam spreading with axial position* and 2) the electron gryo radius in the tank plasma and earth's magnetic field

---

* The fact that the plasma potential profile exhibits spreading however does not necessarily mean the ion density profile spreads similarly.

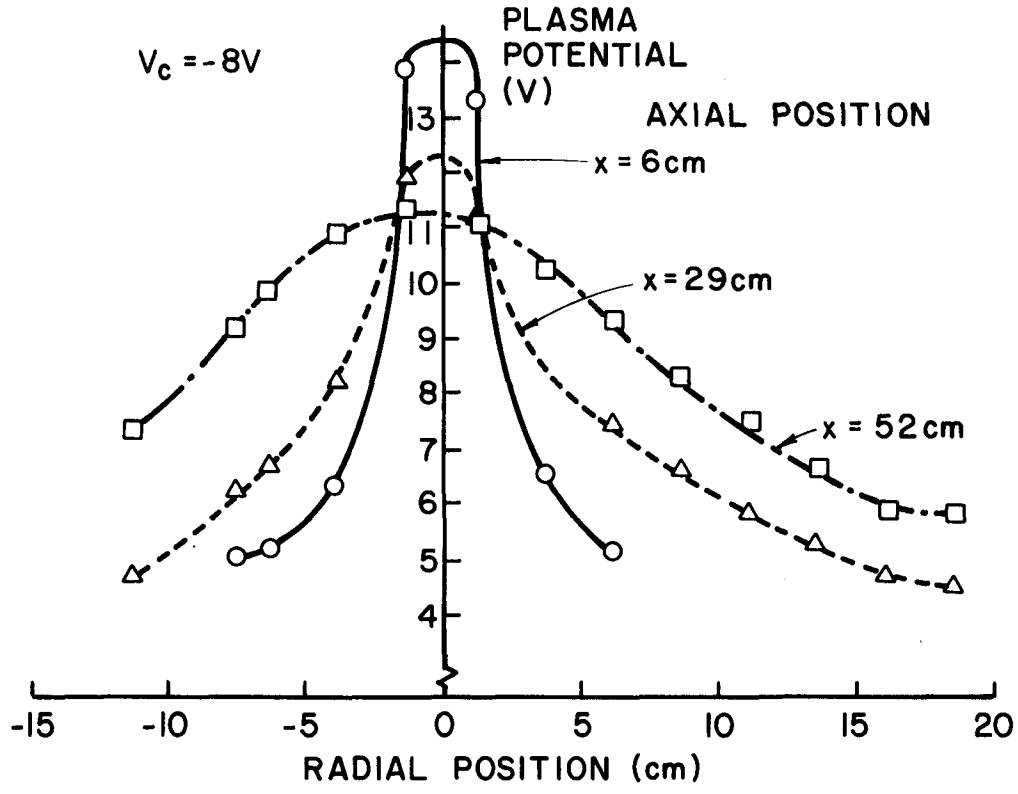

a. NEUTRALIZER ON FIELD LINE MISSING BEAM ℄ BY ~30cm

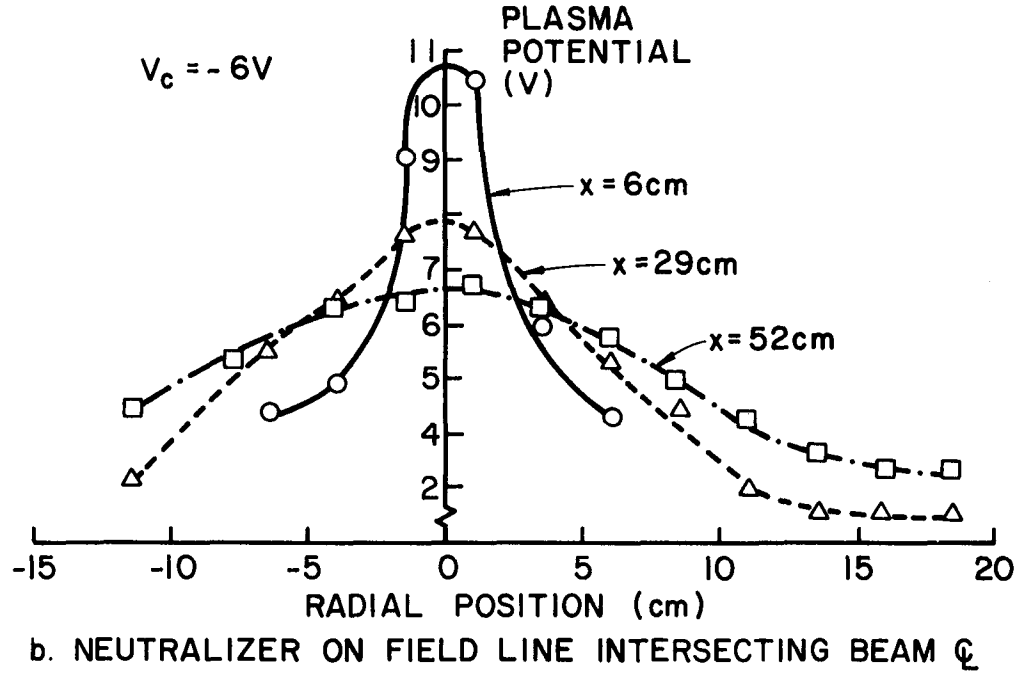

b. NEUTRALIZER ON FIELD LINE INTERSECTING BEAM ℄

Figure 3. Effect of Distant Neutralizer Position in the Earth's Magnetic Field.

is about 10 cm. The fact that the gyro radius is less than the 30 cm distance between the magnetic field line passing through the neutralizer plasma and the beam centerline is consistent with the observed change in the plasma potential profiles. It is also noted that the neutralizer bias voltage required to effect neutralization of the 100 mA beam current (V_c) tracked with the changes in plasma potentials. It has been suggested[6] that fluctuations in beam plasma potentials of the order of several volts observed during the SERT II space tests could have been caused by spacecraft motion in the earth's magnetic field. These fluctuations were originally attributed to a spacecraft wake effect but the relative motion of the distant neutralizer and beam in the earth's magnetic field could have also caused this effect in much the same way it was induced in the test just described.

The Influence of the Magnetic Field at the Distant Neutralizer

For this series of tests the electromagnet at the distant neutralizer was positioned so its solenoidal magnetic field was aligned with the neutralizer axis as suggested by the inset sketch in Figure 4. As the electromagnet current was varied the shapes of the field lines shown in Figure 4 were not altered but the field strengths did change. The beam plasma potential profiles at axial locations of 6, 29 and 52 cm downstream of the grids were measured as this change was effected. The relative shapes and magnitudes of these profiles at these three axial positions were however very similar to those shown in Figure 4. As a result the plasma potential at the beam centerline 6 cm downstream of the grids was selected as representative of the state of the beam. Figure 4 shows that the magnitudes of both this representative beam plasma potential and the neutralizer bias voltage increase as the magnitude of the solenoidal magnetic

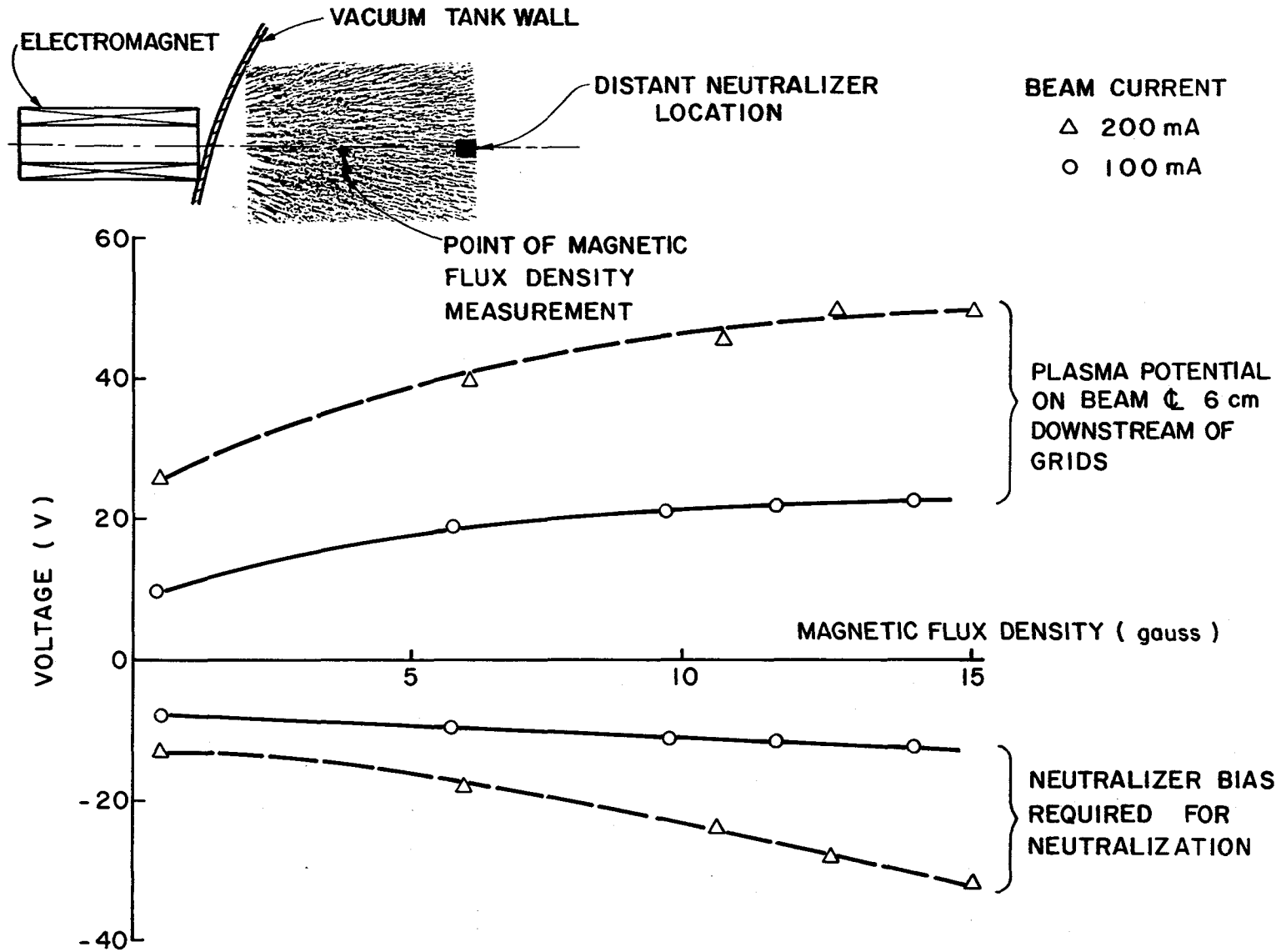

Figure 4. Effect of Magnetic Field at Distant Neutralizer on Beam Plasma and Neutralizer Bias Potentials.

field at the neutralizer tip is increased. The same behavior is observed at both beam current levels although the magnitudes of both voltages are higher at the higher beam current level.

Figure 5 shows that the coupling voltages between neutralizer and beam plasma (i.e. total voltage drop from beam plasma to neutralizer tip) taken from the data of Figure 4 are nearly directly proportional to magnetic flux density at both beam currents. Further, these voltage difference levels increase in direct proportion to the beam current level. Visual observation of the neutralizer plasma when the solenoidal magnetic field current was increased showed that increases in the field strength caused the luminous region associated with the cathode discharge to contract. As the magnetic field strength was increased to its maximum value the hollow cathode discharge appeared as a very tiny bright spot at the orifice. In a final phase of this experiment the electromagnet flux density was adjusted to 14 gauss and the electromagnet axis was rotated until it was at 90° to the neutralizer axis. As long as the solenoid axis was directed at the neutralizer cathode orifice the beam plasma and neutralizer biases remained at the high levels of Figure 4. Measurement of the magnetic fields at the neutralizer when the solenoid was rotated suggested the field direction at the point of measurement remained essentially as shown in the filings map of Figure 4.

The Influence of the Magnetic Field at the Local Neutralizer

The test results obtained with the local SIT 8 neutralizer showing the influence of stray magnetic fields in its vicinity on neutralization performance indicators are shown in Figure 6. In this case the neutralizer is located in the magnetic field associated with the thruster itself and the test involved altering this field with an external magnet and measuring the resulting changes in beam and neutralizer potentials. The central iron

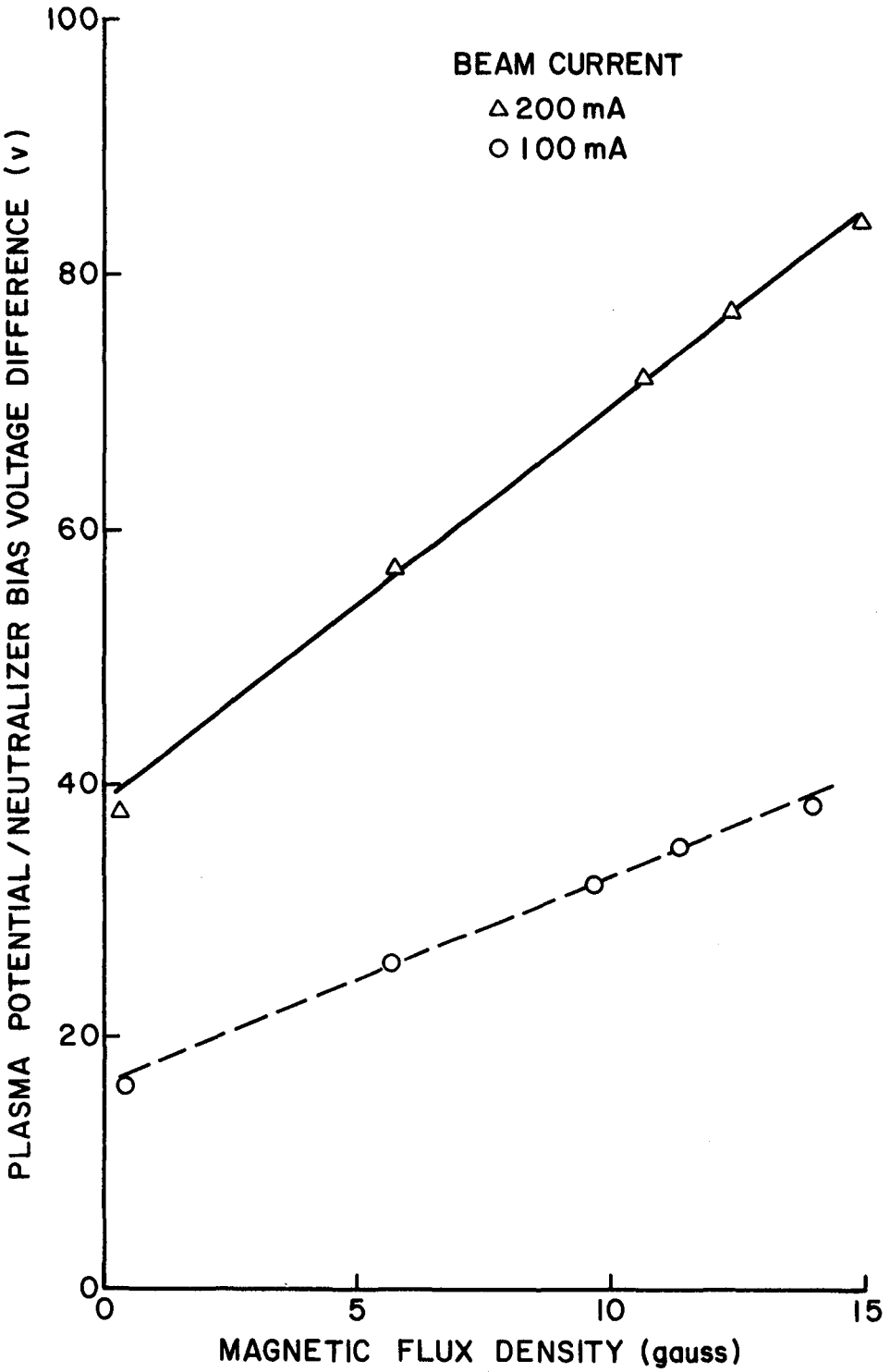

Figure 5. Effect of Magnetic Field at the Distant Neutralizer on the Coupling Voltage Between the Neutralizer and Ion Beam.

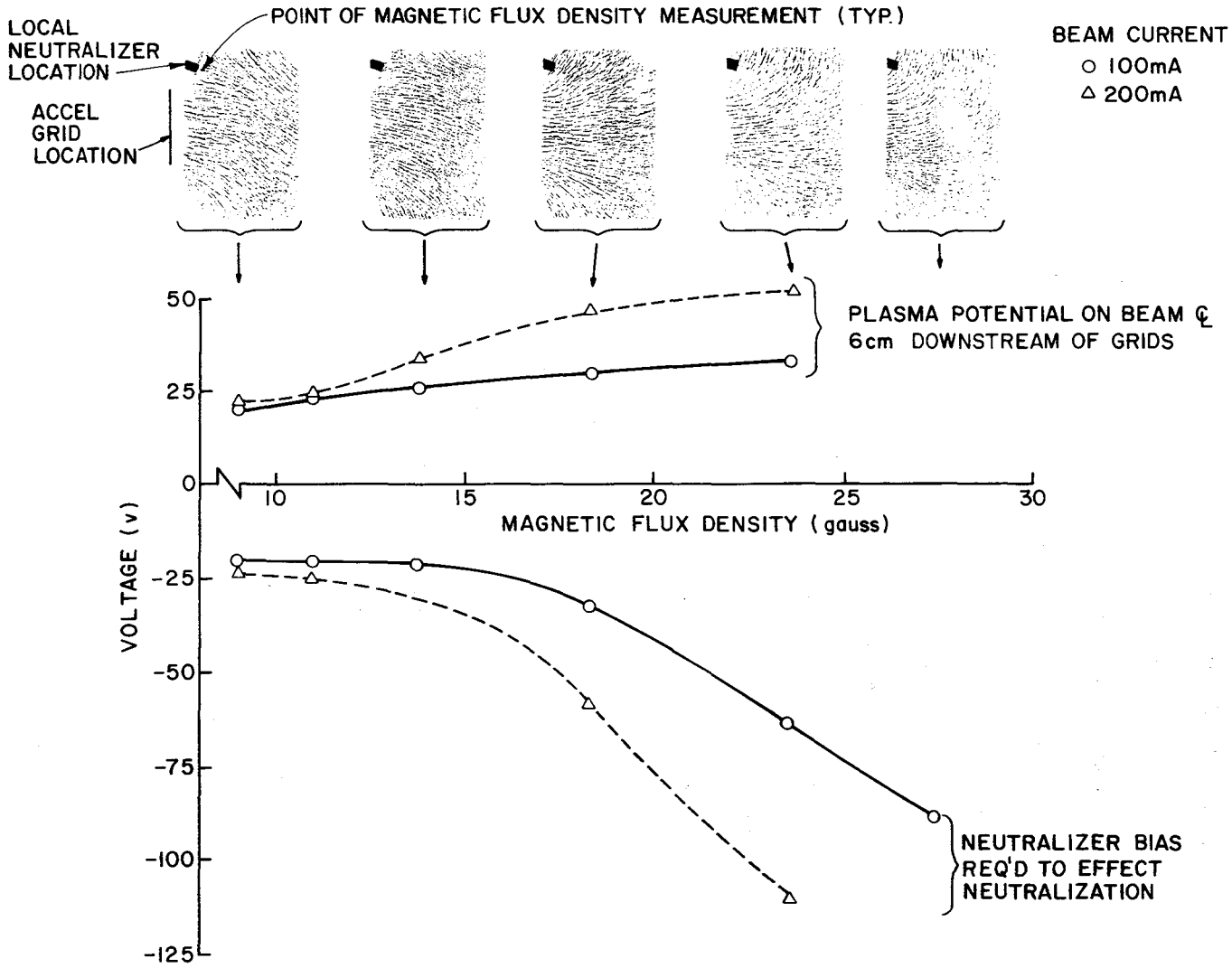

Figure 6. Effect of Magnetic Field at Local Neutralizer on Beam Neutralizer Bias Voltages.

filings map in Figure 6 shows the unaltered magnetic field associated with the thruster as well as the location of the neutralizer in this field. In the filings maps to the left of center the external magnet acts to cancel the thruster field thereby reducing the magnitude of magnetic flux density at the neutralizer and bending the field lines passing through the neutralizer toward the ion beam. In the filings maps on the right the external magnet is used to increase the magnetic field magnitude and draw the field lines passing through the neutralizer still further away from the beam. The arrows associated with each filings map indicate the magnetic flux density at the neutralizer corresponding to that filings map. Figure 6 shows that when the magnetic flux density magnitude is increased and field lines passing through the neutralizer are drawn further away from the beam, the neutralizer bias and beam plasma potentials are increased. Conversely, reducing the magnetic field flux densities and directing the field lines toward the beam reduces the magnitudes of these potentials somewhat. As with the distant neutralizer (Fig. 4), operation at higher beam currents requires higher potential differences between the beam and neutralizer in order to effect neutralization.

A PHENOMENOLOGICAL DISCUSSION OF TEST RESULTS

In the cases under consideration a neutralizer is operating at a given electron emission current level and hence the potential difference between the beam and neutralizer plasmas must increase as the resistance between these plasmas increases. The value of this resistance is difficult to compute from the plasma conditions because the current path involved is neither well defined nor readily measured. It can be stated however that the increase in resistance that must occur is induced by one or more of the following effects occurring along the current flow path 1) an increased

electron collision rate at a location where conduction current dominates, 2) an increased electron conduction path length or 3) the intervention of magnetic field components at right angles to the electric fields driving the electrons between the neutralizer and beam plasmas in regions of high Hall current. The test results described here do not seem to show unequivocally that one of these effects dominated and therefore led to the higher resistance observed when magnetic fields were altered at distant and local neutralizers. It is suggested however that all of these effects may be contributing to observed increases in resistance for these tests.

The total resistance along the current path from the neutralizer to the beam is a sum of the infinitesimal resistances over the total conduction path. At the neutralizer orifice the neutral density may be sufficiently high to yield a pressure approaching 1 torr, hence the electron collision frequency is high and conduction current dominates. When the magnetic field intensity is increased in this region, the electron flow is forced along field lines passing through the orifice. This reduces the cross-sectional area through which the current flows and results in a high resistance and hence a high potential drop at the neutralizer cathode itself. This appeared to be occurring when the magnetic field was increased at the distant neutralizer.

As the electrons leave the vicinity of the neutralizer they may find themselves on field lines carrying them away from the beam, a condition that could lead to increased resistance as a consequence of Effects (2) and (3). For the experiments associated with the local neutralizer it appears that any of these three effects could be accounting for observed increases in potential differences as the stray magnet fields associated with the thruster were altered.

CONCLUSIONS

The intensity of the magnetic field at a neutralizer cathode orifice influences its ability to couple to the ion beam. Stray magnetic fields associated with ion thrusters themselves are sufficiently large to cause a substantial increase in the voltage difference between the neutralizer and the beam plasma. In order to minimize this voltage difference a region as free of magnetic fields as possible should be selected for placement of the neutralizer. The neutralizer does not seem to have any difficulty coupling to the ion beam over distances of the order of 1 meter as long as the magnetic field levels are low (of order 0.5 gauss or less). If a neutralizer must be located in the region of a stray thruster magnetic field, an external magnet can be used to alter the magnetic field so it is directed toward the ion beam. This improves coupling and does not seem to alter thruster performance measurably. Magnetic fields of the order of those associated with the earth ($\sim$ 0.5 gauss) can effect small beam plasma potential charges (of order 1v) when they are interposed between an ion beam and a neutralizer located of order 1 meter away.

CURRENT DENSITY CAPABILITIES OF CLOSELY SPACED GRIDS

Dean Rovang

INTRODUCTION

In order to minimize the number of electrostatic thrusters required for a mission and hence the cost of the thruster subsystem it is generally desirable to increase the thrust densities of these devices above those attainable by currently available ion thrusters. In order to keep thrusters operating at their optimum specific impulse this should be accomplished by increasing the ion beam current density extracted from the ion optics system without increasing the exiting ion velocity. The current density of these accelerator systems is generally limited by Child's law

$$j \propto \frac{V_T^{3/2}}{(\ell_e')^2} \quad . \tag{1}$$

Here, "j" is the ion beam current density, "V_T" is the total accelerating potential between the two grids closest to the discharge plasma and "ℓ'_e" is the effective acceleration length associated with this grid pair. These grid parameters can also be related to the ion beam power requirement per unit area (P/A) by the expression

$$P/A \propto \frac{V_T^{5/2}}{(\ell_e')^2} \quad . \tag{2}$$

Since the total acceleration voltage influences the exiting ion velocity, it is constrained by the mission under consideration. Under this constraint Equations (1) and (2) suggest that the most efficient way to increase the beam current density is by decreasing the effective acceleration length. The problem with decreasing this length is that the trend in ion thrusters at the present time is toward larger diameter discharge chambers. Fabrication considerations dictate a constant span-to-gap ratio for the grids so this

trend dictates larger effective acceleration lengths and still lower current densities. To alleviate this problem a new design for an accelerator system has been proposed that would incorporate an array of small, closely spaced grid pairs mated together to form a larger composite grid system for a single thruster. Before design and testing of this facited grid system is attempted, however, it is desirable to determine the current density limits of small, closely spaced grids. This information in turn will facilitate evaluation of the performance benefits of the concept. It is for this purpose that the present experimental investigation was undertaken.

BACKGROUND AND THEORY

Ion Beam Formation

The essential components of a basic ion accelerator system are shown in Figure 7. Although the side view of a single aperture is depicted, it should be noted that a multi-aperture system is implied. The accelerator system is placed adjacent to a discharge chamber containing a low density ionized plasma at a potential of a few tens of volts above that of the screen grid. Potentials applied to the grids produce an electric field that accelerates the ions and repels the electrons coming from the discharge plasma. Around each screen hole a sheath is formed which defines the boundary between the plasma and the acceleration region. As suggested in Figure 7 the important geometrical parameters are the screen and accelerator grid hole diameters (d_s and d_a), the thicknesses of these grids (t_s and t_a) and their separation (ℓ_g). From Aston's work,[5] it was determined that the sheath shown schematically in Figure 7 never enters the screen hole except in conditions of extremely poor ion beam focusing. For this reason the effective acceleration length (ℓ_e') has been redefined here from previously

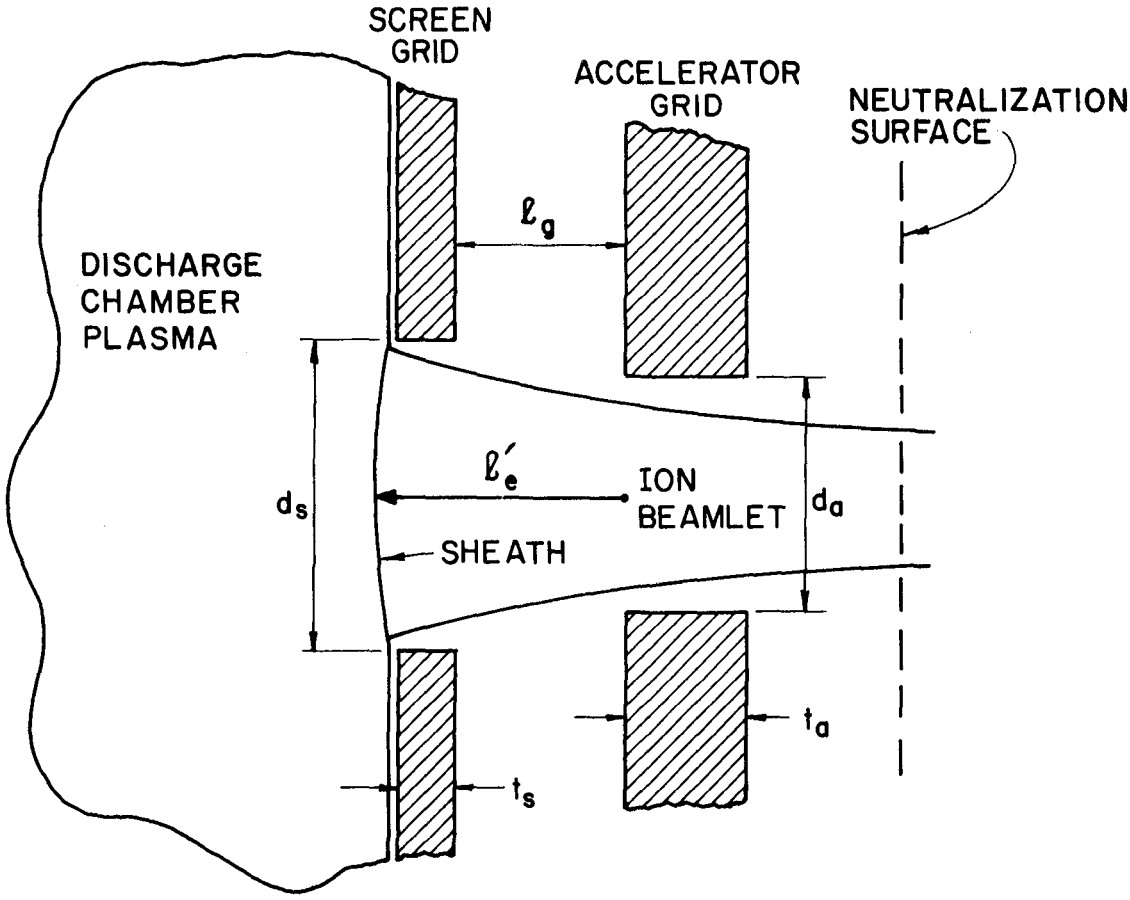

Figure 7. Optical System Schematic.

used values to include the thickness of the screen grid, i.e.,

$$\ell_e' = \left[(\ell_g + t_s)^2 + d_s^2/4\right]^{\frac{1}{2}} \quad . \tag{3}$$

The suitability of this new definition of effective acceleration length is discussed in Appendix A.

The mean beam current density capability (j) of a grid system like the one shown in Figure 7 is generally considered to be limited by space charge effects as described by Child's law in the form

$$j = \frac{4\varepsilon_o}{9}\left(\frac{2q}{m_i}\right)^{\frac{1}{2}} \frac{V_T^{3/2}}{(\ell_e')^2}\ \eta_o \quad . \tag{4}$$

In this equation describing the one-dimensional model of the ion acceleration process ε_o is the permittivity of free space, q is the ion charge, m_i is its mass and η_o is the effective open area fraction of the grid system to the ions. This equation does not represent the only limitation on the current density however. The current density of ions arriving at the plasma sheath, where the Child's law acceleration process begins (Fig. 7), is determined by the Bohm condition for a stable sheath, i.e.,

$$j = n_i q \eta_o \sqrt{\frac{eT_e}{m_i}} \quad . \tag{5}$$

In this equation the ion density (n_i) is equal to the electron density (n_e) of the discharge plasma and the electron temperature (T_e) of the plasma is in electron volts. The quantity "e" is the electron charge. Operating experience suggests it is generally Equation (5) that determines the current density associated with a thruster because this current is controlled by discharge chamber operating parameters. This observation leads one to the conclusion that the effective acceleration length ℓ_e' adjusts itself so that Child's Law will be satisfied. Considering only Equations (4) and (5) one

can conclude that essentially any reasonable value of current density could be achieved as the effective acceleration length is reduced by simply increasing the electron density and temperature of the discharge plasma. There are however other considerations that must be taken into account.

Previous ion optics work by Aston[7] shows that the value of the ratio of the effective acceleration length to screen aperture diameter (ℓ_e'/d_s) must fall within a certain range in order to produce an acceptably well-focused beam. This requires that as ℓ_e' is reduced the diameter of the screen hole must also be reduced. Previous investigators[7,8] have reported however that a reduction in the maximum attainable normalized perveance per hole* for screen hole diameters smaller than 2 mm. Since maximum normalized perveance per hole is directly related to the maximum beam current density, this means the current density begins to drop below the limiting value dictated by Child's Law. It has been suggested that this reduction in attainable current density with screen hole diameter might be caused by a plasma related blockage of the screen hole. The implication is that the area through which a beamlet is extracted depends not only on the geometrical open area fraction of the aperture (f) (ratio of total screen hole area to

---

* The maximum normalized perveance per hole (NP/H) given by

$$NP/H = \frac{J}{V_T^{3/2}} \left(\frac{\ell_e'}{d_s} \right)^2 = \frac{\pi \varepsilon_o}{9} \left(\frac{2q}{m_i} \right)^{1/2} \qquad (5a)$$

where J is the ion current per grid hole, has a theoretical limit a for a particular propellant given by the right hand side of this equation. In the case of argon, the theoretical limit has a value of 6.8×10^{-9} $A/V^{3/2}$. This parameter, maximum normalized perveance per hole, will be used to compare the ion extraction performance of the various grid sets investigated.

total grid area) but also on the properties of the discharge plasma as reflected through its Debye length.[8] For grid systems having circular holes it is suggested that this effective open area fraction might be modelled by considering the screen holes to be partially blocked by the discharge plasma in the manner suggested in Figure 8. In this figure, ℓ_h represents the center-to-center hole spacing, d_s, the screen hole diameter and λ_D, the Debye length of the discharge chamber plasma. The Debye length, determined by the discharge plasma properties, is given by

$$\lambda_D = \left(\frac{\varepsilon_o T_e}{n_e e} \right)^{\frac{1}{2}} \tag{6}$$

for T_e in electron volts. As suggested by the figure the effective diameter of the apertures through which ions are drawn is $d_s - 2\lambda_D$. Ions that enter the annular region within a Debye length of the hole circumference are assumed to be lost (probably to the screen grid webbing) so they are not drawn into the beam. The open area fraction of the grids can be calculated now by computing the fraction of the triangular section of Figure 8 through which the ions can flow, i.e.,

$$\eta_o = \frac{\pi}{2\sqrt{3}} \left(\frac{d_s}{\ell_h} \right)^2 \left(1 - \frac{2\lambda_D}{d_s} \right)^2 \equiv f \left(1 - \frac{2\lambda_D}{d_s} \right)^2 . \tag{7}$$

Presuming the correctness of this model, Equations (6) and (7) taken together point out the importance of establishing proper discharge plasma conditions in achieving high beam current densities. These conditions must be such that a high Bohm current density and a small Debye length are achieved, a condition associated with a high plasma density and a low Maxwellian electron temperature.

Finally there are two additional phenomena that need to be addressed when considering the limitations on the current density of an ion

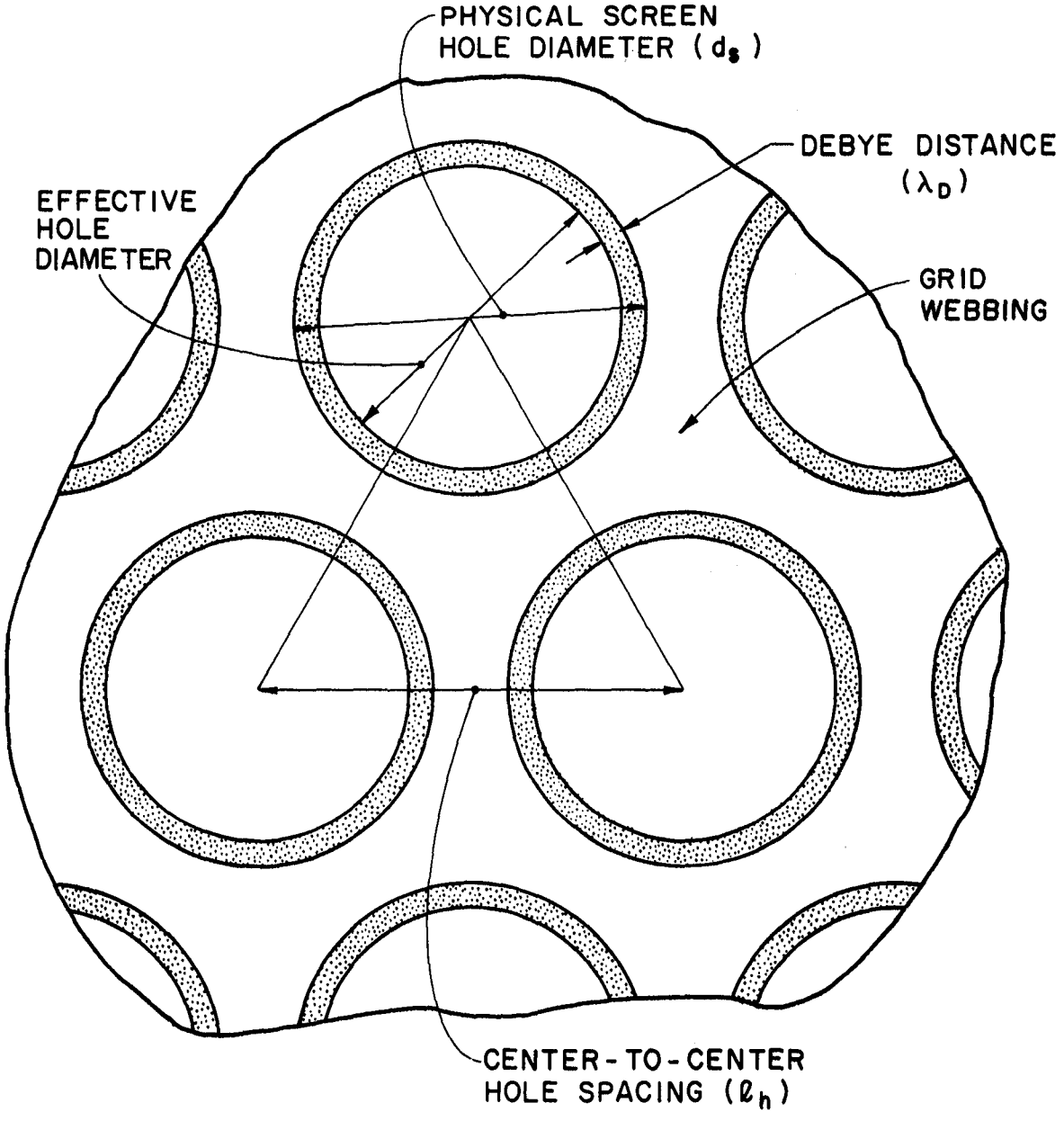

Figure 8. Schematic of Plasma Blockage Phenomenon.

acceleration system. These are electrical breakdown and electron backstreaming and their occurrence during the actual testing detracts from the absolute lower limits of grid separation distances that can be realized in practice. Electrical breakdown occurs when the electrical field strength between the grids (total accelerating voltage divided by the grid separation distance) exceeds the breakdown limit. When this occurs substantial electron currents begin to flow between the grids. This limit is determined by the geometry of the grids as well as such factors as the grid surface finish and density of charged and neutral particles between the grids. Electron backstreaming occurs when electrons in the ion beam plasma find a path along which they can be accelerated through grid apertures directly into the discharge chamber. This condition exists when the ratios of screen hole diameter-to-grid separation distance and/or net-to-total accelerating voltage ratio reach relatively high values.

APPARATUS

Ion Source

All testing has been conducted on a cylindrical multipole 8 cm diameter by 10 cm long ion source. Because very high current densities were being sought in this study it was essential that the discharge chamber be capable of meeting or exceeding the current density capacity of the grids. This, in turn, implied a chamber capable of producing very high discharge plasma densities. In order to achieve these high plasma densities it was desirable to make a small chamber incorporating several special features. The multipole magnet poles separating the cylindrical anodes in this design are 1.3 cm apart; this close pole piece spacing was selected so magnetic field peneration into the small diameter discharge chamber would not be sufficient to affect plasma conditions over the $\sim$ 1 cm diameter core of the discharge chamber from which

the ion beam is extracted. Because of the elevated temperatures expected at the high discharge power levels required, high temperature stainless steel-sheathed, oxygen-free copper wire was used for the electromagnet windings. Also, in an effort to enhance the removal of heat generated in the discharge chamber, a water-cooled copper jacket was wrapped around the thruster body. Leakage current from the thruster to ground through the water line to this jacket was found to be negligible under normal test conditions ($\lesssim$ 0.01 mA).

Optical System

During this investigation, the current extraction capability of three different nineteen aperture grid sets were investigated, each characterized by a different screen aperture diameter. The diameters selected were 2.0 mm, 1.5 mm, and 1.0 mm. Because of the desire to achieve the highest possible perveance from each grid set, the screen and accelerator grids were all made from the thinnest sheets of graphite commercially available (0.254 mm). For this same reason the diameter of the accelerator hole was set equal to that of the screen grid hole. The grid aperture pattern used was a hexagonal array with center-to-center hole spacings of 2.5 mm for all aperture diameters.

Because the grid separation distance was the focus of this study the test apparatus was designed so this parameter could be varied continuously while the ion source was being operated. This is accomplished by means of the apparatus shown schematically in Figure 9. The grid separation is varied using this apparatus by moving the fork-shaped wedge in the manner suggested by the large arrow. As this wedge is moved toward the grids it forces the accelerator and screen grid support plates apart and hence the screen and accelerator grids attached to these plates are also separated. For the reasons mentioned previously, all materials used in the construction of this

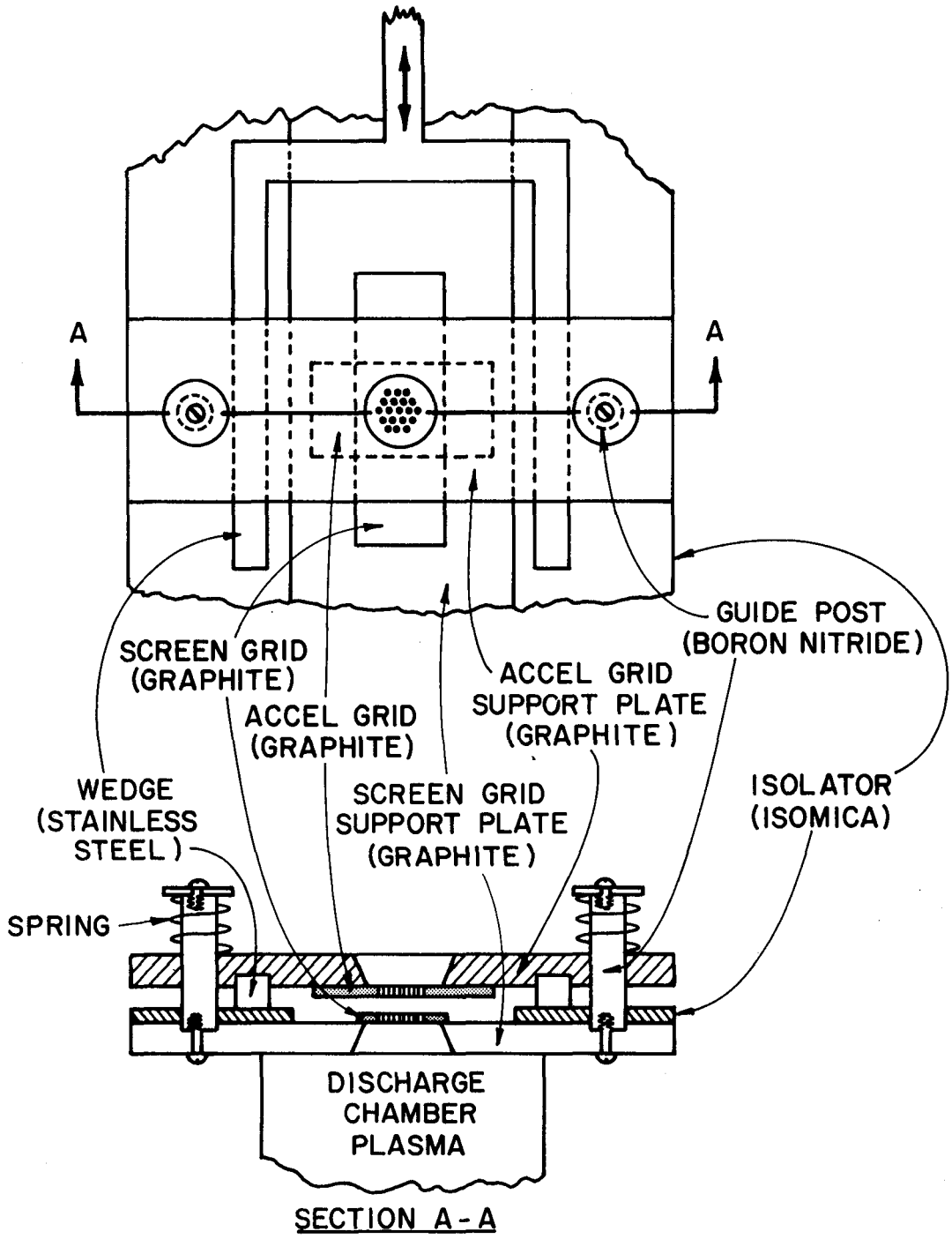

Figure 9. Variable Grid Spacing Apparatus.

apparatus are capable of withstanding high temperatures. Graphite was used for both the grids and grid support plates to minimize the differential thermal expansion between these components that could cause grid warpage. Initial alignment of the grids is accomplished manually by positioning and clamping each grid and then checking their alignment visually beneath a large illuminated magnifying glass. This alignment is maintained during operation by the boron nitride guide posts shown in Fig. 9. Electrical isolation is assured by the sheet of isomica between the screen grid support plate and the wedge. The wedge is mechanically connected to a micrometer used to measure and adjust its translation from the outside of the vacuum system. Immediately after each period of data collection, while the source was still hot, the grid separation distance was reduced until the measured electrical resistance between the grids went to essentially zero, i.e., grid separation distance equalled zero. This reference point on the micrometer along with the geometry of the wedge could then be used to calculate the grid spacings from the micrometer readings recorded during the testing.

Even though efforts were made to reduce grid warpage due to thermally induced forces by matching the material of the support plates to that of the grids there was still evidence of grid warpage on some test runs. The fact that it was not apparent on other runs suggests it may have been a function of the tightness of the screws that clamp the grids to their respective support plates. Evidence of grid warpage during thermal cycling was evidenced by such phenomena as changes in the impingement current when the grids were not being moved manually and by electrical breakdown occuring at unreasonably low electric fields. None of these effects were observed during the collection of data presented herein and while some warpage might have occurred, it is believed that actual grid spacings were close to those indicated by the micrometer readings.

OPERATING CONDITIONS AND PROCEDURE

Throughout this study, the ion source and accelerator system were operated at the following conditions

Screen Voltage	+ 500 V
Accelerator Voltage	- 250 V
Discharge Voltage	50 V
Propellant (Argon) Flow Rate	53 mA (equivalent)
Magnet Current	7 A
Bell Jar Pressure	$\sim 4 - 5 \times 10^{-5}$ torr

The test procedure involved setting the grid separation at an initial high value limited by the apparatus. The cathode emission was then increased in steps and this caused an increase in the discharge, beam and impingement currents. These currents were recorded manually from high accuracy digital gauges at each step. When the impingement current reached $\gtrsim$ 10% of the beam current the cathode emission was reduced, the grid separation distance was reduced and the process of increasing the emission current was repeated. The reduction in grid separation was continued until either electron backstreaming or high voltage breakdown was observed. The same test procedure was followed for each of the three grid sets studied.

RESULTS

The measured beam current divided by the number of grid holes (nineteen) and by the physical open area of each hole yields the beam ion current density being used for presentation of the data. Figure 10 shows typical curves of the impingement current (normalized using beam current) versus the beam current density determined in this way for grids having 2.0 mm dia. holes. Similar curves were generated for the other hole diameters investigated. The symbols in Figure 10 have been defined previously except for the quantity

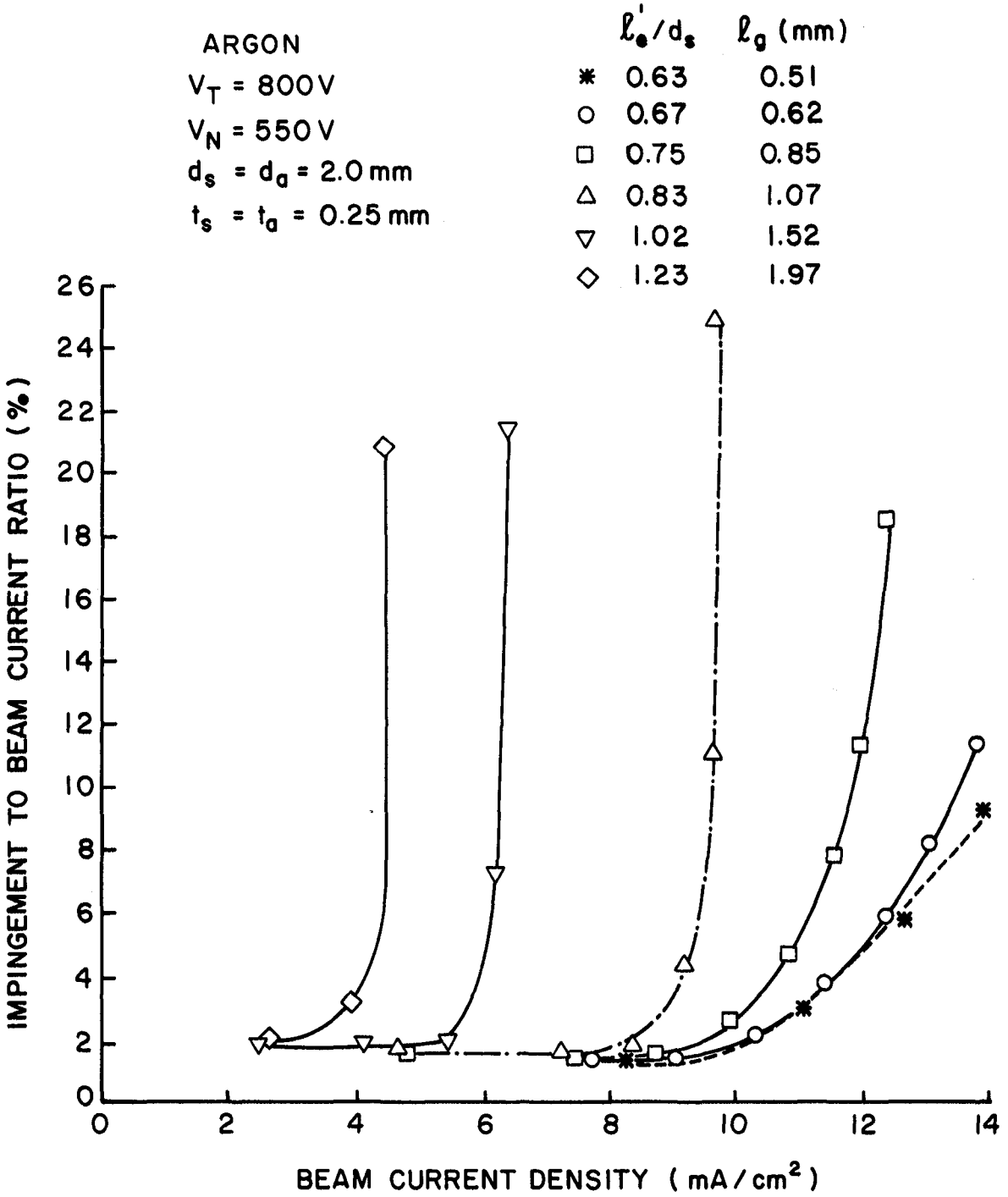

Figure 10. Current Density Capability of 2 mm dia. Grid Apertures.

V_N which represents the net accelerating voltage. It should be noted that the impingement currents of Figure 10 include both charge exchange and direct impingement components. Calculations and measurements made early in this study suggested the contribution of the charge exchange induced impingement current associated with neutral flow from the discharge chamber was about 1 percent of the beam current. This charge exchange component probably accounts for most of the impingement shown in the horizontal segments of the curves shown in Fig. 10. Figure 11 shows the data of Figure 10 replotted with normalized perveance per hole as the dependent variable. The suitability of this variable and the consistency of the data are demonstrated by the fact that the curves corresponding to grid separations (ℓ_g) of 1.07 mm and greater fall on top of one another and exhibit a knee at a perveance just over 8×10^{-9} Amps/volt$^{3/2}$. As the grid separation is reduced below 1.07 mm the impingement current begins to increase above the baseline value at progressively lesser perveance values. This indicates the onset of poor focusing and shows that unacceptably high impingement preceeds any limitation associated with electrical breakdown or electron backstreaming for this case of 2.0 mm dia. grid holes. As the hole diameter was reduced to 1.5 mm in subsequent tests, the grid separation distance could be reduced to lower values before the impingement current curves like those shown in Fig. 11 began to depart from the ideal case where the curves are coincident. For the 1.0 mm dia. hole diameter the emission capability of the ion source limited its capacity to reach the knee of the impingement vs. perveance curve. Hence in all three cases poor focusing of the ion beam or a discharge chamber condition limited the current density capability of the grids. Although electrical breakdown could be induced with any grid set by reducing the grid separation sufficiently the impingement current level always became excessive at lesser grid separations.

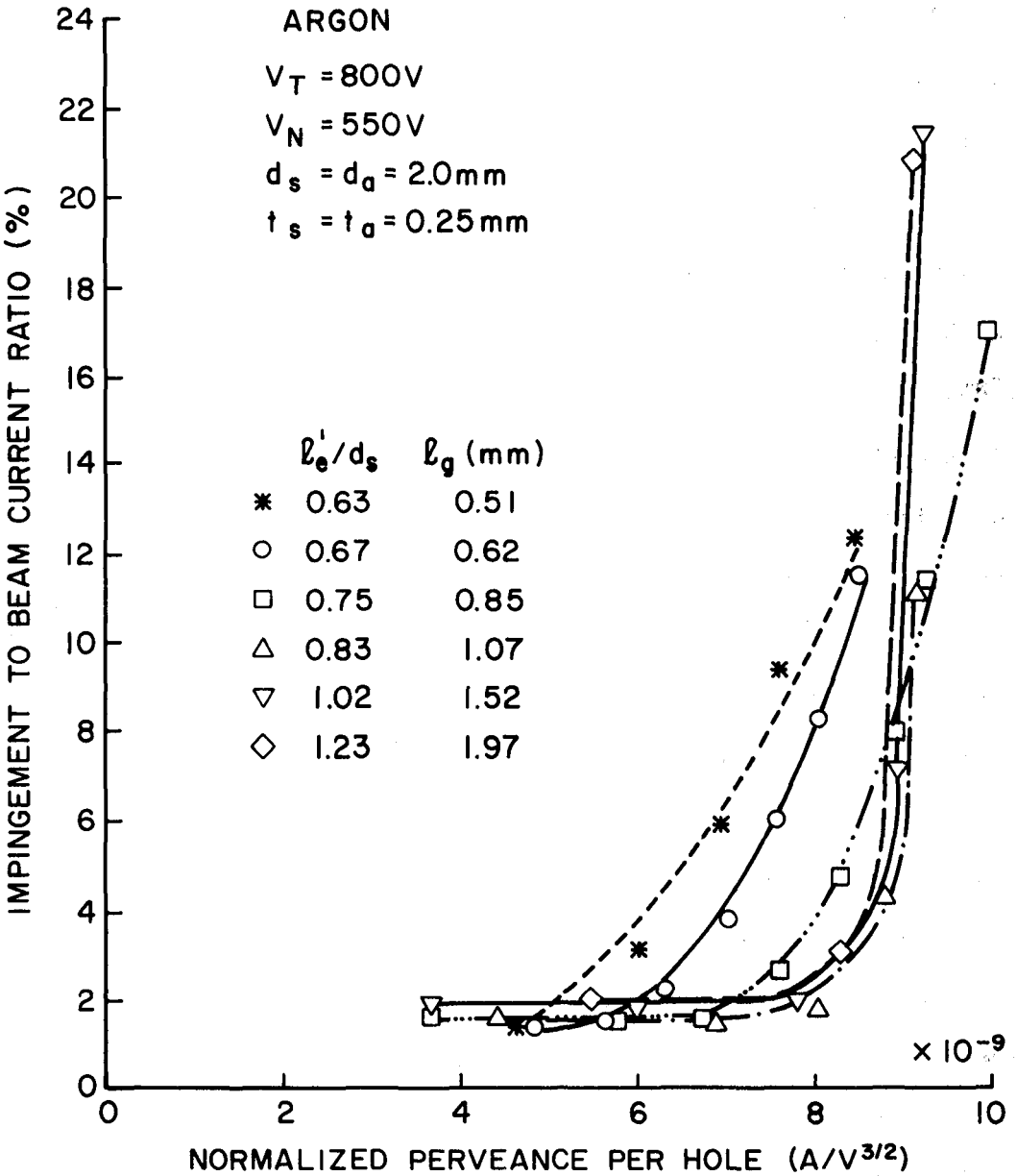

Figure 11. Perveance Characteristics of 2 mm Grid Apertures

With regard to the data in Figures 10 and 11, it should be noted that with the 2.0 mm dia. holes, electron backstreaming was observed at grid separation distances below a value of 0.62 mm. It is of interest to compare this preliminary backstreaming data with data reported by Kaufman.[8] The parameter defining the onset of backstreaming suggested by Kaufman is given by

$$(1 - R)\ (\ell_e/d_s)\ \exp(t_a/d_s) \quad . \tag{8}$$

The values obtained for this parameter at the onset of electron backstreaming in these tests were approximately 5 percent higher than those reported by Kaufman. Although a detailed correlation of electron backstreaming data was not the objective of this study, the variable grid spacing apparatus developed for the work have been found to be very suitable for the conduct of such a test. The collection of this data is planned during the coming year.

In order to compare the maximum current density capabilities of the three aperture sizes investigated, it is meaningful to define a maximum perveance condition, i.e., the perveance level at which the direct impingement becomes excessive. The rather arbitrary criterion adopted here is that the maximum current density corresponds to an impingement-to-beam current ratio of three percent. This usually represented slightly over a hundred percent increase in direct impingement current above its baseline (or charge exchange induced) value. Using this criterion, Figure 12 shows how the maximum beam current density increases as the diameter of the screen grid aperture and/or the effective acceleration length are reduced. The solid symbols on the curve for the 1.0 mm hole diameter case represent the operating points where the maximum current density obtainable was not limited by excessive impingement current but was instead limited by the

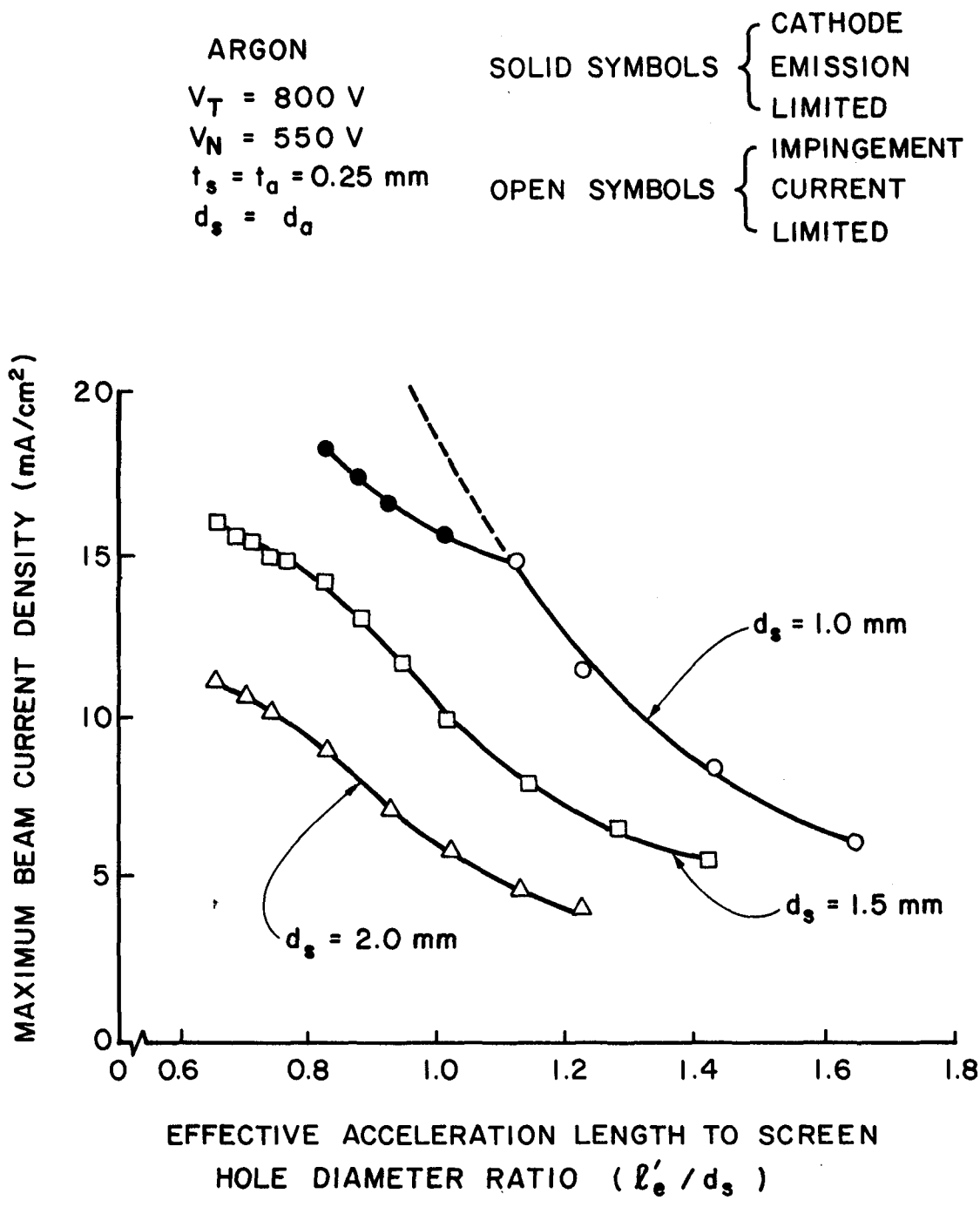

Figure 12. Effect of Screen Aperture Diameter on Extracted Ion Current Density.

electron emission capability of the ion source. The extrapolated dotted line suggests that even higher current densities could be expected with an ion source capable of producing the necessary Bohm current densities, i.e., higher plasma densities. The use of such an ion source is planned for future research on this topic. Finally, it is noted that the average current densities achievable in the beam downstream of the grids with a given grid set would be less than the values cited in Figure 12 by a factor determined by the open area fraction of the grids.

Even though electron backstreaming and electrical breakdown did not actually limit the current extraction capabilities of the grids they could be observed at close grid separations. Backstreaming was observed only with the 2.0 mm grids and electrical breakdown could be induced in the 1.5 mm and 1.0 mm dia. screen hole cases. The breakdown electric fields (V_T/ℓ_g) were just over 2 kv/mm for both of these screen hole sizes. While they were repeatable, these electric fields are considerably lower than those achieved previously at this facility ($\sim$ 6 kv/mm) with grids of comparable size operated at similar background pressures.[9] Although the explanation for this is uncertain, it might be an indication of grid warpage induced by differential thermal expansion. It is considered more likely however that it was related to the high impingement current condition that existed when breakdown occurred in the present tests. It is also considered likely that grid outgassing induced by the higher temperatures that existed in the present tests contributed to the lower breakdown electric fields observed.

A more useful comparison of the current extraction capability of the various grid sets than that given in Figure 12 can be made using maximum normalized perveance per hole to describe the grid performance. Using this parameter, Figure 13 compares the performances of the three grid sets

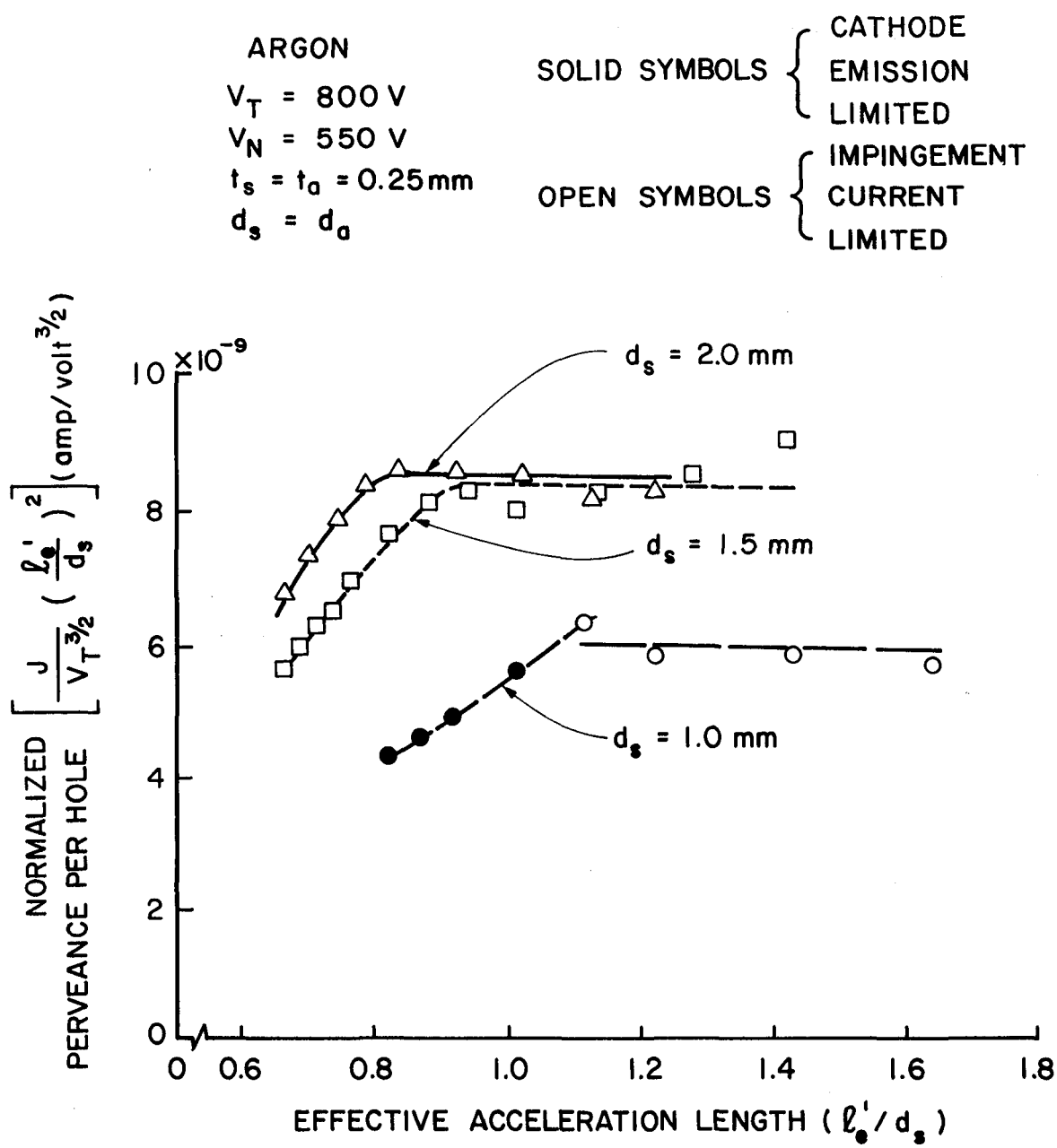

Figure 13. Effect of Screen Aperture Diameter on Ion Extraction Performance.

investigated as a function of normalized effective acceleration length (ℓ_e'/d_s). The curves corresponding to screen hole diameters of 1.5 and 2.0 mm show similar behavior. As the effective acceleration is reduced the perveance is at first constant at a value near 8.5×10^{-9} $A/V^{3/2}$, then it drops as the accelerator impingement begins to limit performance. With the 2.0 mm holes the effective acceleration length can be reduced to a slightly lower value ($\sim$ 0.8 vs. $\sim$ 0.9 for the 1.5 mm dia. holes) before this impingement induced perveance drop occurs. The fact that these effective acceleration lengths are as close as they are suggests this length is a good correlating parameter. Substantially poorer performance is observed with the 1.0 mm dia. grid holes. It is possible that some of this decrease is attributable to the postulated reduction in effective open area of the grid apertures due to the Debye shielding effect, but some of the decrease is also probably due to the increase in normalized screen and accelerator grid thickness ratios which occurs when the screen diameter is reduced at constant grid thickness. Because of the preliminary nature of this investigation and the limited amount of data that has been collected to date, no attempt will be made to separate these effects. In the future, however, such information will be necessary if an accurate model for the "Debye shielding effect" is to be developed.

Finally, it is noteworthy that most of the maximum normalized perveance per hole data given in Figure 13 lie above the theoretical Child's limit for argon of 6.8×10^{-9} $A/V^{3/2}$. This apparent violation of Child's Law is considered to be a consequence of the fact that the ion acceleration process is not one-dimensional as assumed in the development of Child's Law. In fact Aston[10] has observed that there is considerable focusing of ions away from the screen grid webbing and through the aperture under high current

density operating conditions. This condition would indeed tend to produce the sort of increase in current density above the Child's Law limit suggested by the data of Figure 13. It is also possible that the theoretical boundary condition of negligible ion velocity at the sheath is violated or that the effective acceleration length used in the expression for normalized perveance per hole doesn't describe the actual acceleration length properly.

CONCLUSION

Substantial increases in the current extraction capabilities of ion thruster systems can be realized by reducing grid hole diameters when accelerating voltages are in the 800 v range investigated. For screen and accelerator grid hole diameters from 2.0 mm to 1.0 mm accelerator grid impingement currents impose performance limit before electron backstreaming or electrical breakdown as the grid separation distance is reduced.

ION BEAMLET VECTORING BY GRID TRANSLATION

John Homa

The study of grid translation effects on ion beam optics has two important applications in the design of electrostatic thrusters. First, for a dished grid pair, hole misalignments are used to redirect the emerging beamlets in order to minimize off-axis thrust. A study that would yield correlations or a model of this phenomenon would facilitate design of these grids. Second, for some applications a vectorable beam is desired[11,12] and grid translation is an easily accomplished method of producing a moderate thrust vectoring capability. In addition, beam focusing may be desirable to increase the current density in such ground-based applications as sputtering.[13] Again a model or correlations describing the effects of hole misalignment on grid optics would be useful in designing the hardware needed for these tasks.

Work done by Aston[7,10] has shown the effects of such parameters as grid separation, grid hole diameter and net-to-total accelerating voltage ratio on the optical performance of a two-grid system with aligned apertures. Optical performance in this context was defined as the beamlet divergence variation with beam current as well as the maximum perveance that could be obtained. The present study of grid translation is intended to examine the effects of the operating and design parameters examined by Aston on grid performance for vectored beams. Of particular importance in this study is the degradation of optical performance as a function of relative grid displacement expressed in terms of beamlet divergence, beamlet deflection and maximum perveance capability of vectored beamlets compared to nonvectored ones.

For a simple two-grid system like the one shown in Figure 14 the beam deflection angle (β, in degrees) can be estimated using linear optics theory[8,14,15] by

$$\beta = - 14.3 \, (\varepsilon/\ell_g) \tag{9}$$

where ε, the relative accelerator grid displacement and ℓ_g, the grid separation distance are shown in Figure 14. The negative sign indicates that the beam deflection is directed opposite to the direction of relative accelerator grid displacement, the beamlet being attracted by the nearest edge of the accelerator grid hole. Figure 14 also illustrates pertinent grid dimensions including screen and accelerator grid aperture diameters (d_s and d_a), grid thicknesses (t_s and t_a), the grid separation distance (ℓ_g) and the grid offset angle δ. This angle is defined in terms of the linear grid displacement ε by the equation

$$\delta = \tan^{-1}\left\{ \frac{\varepsilon}{\ell_g + t_s} \right\} . \tag{10}$$

APPARATUS AND PROCEDURE

The beam vectoring study has been conducted on an 8 cm dia. ion source[10] in which the grids have been masked down to a 1 cm^2 aperture area. This masking of the grids results in very uniform plasma properties at each aperture and hence a uniform beam. The thruster uses a tungsten filament cathode and neutralizer and operates with argon as the propellant.

The grids are fabricated from graphite sheets with a hexagonal nineteen hole array. Spacing of the grids is provided by mica insulating sheets. While the accelerator is held fixed, the screen grid can be translated along one axis during thruster operation by a mechanical system coupled to a micrometer assembly in the manner suggested in Figure 15. The screen grid was

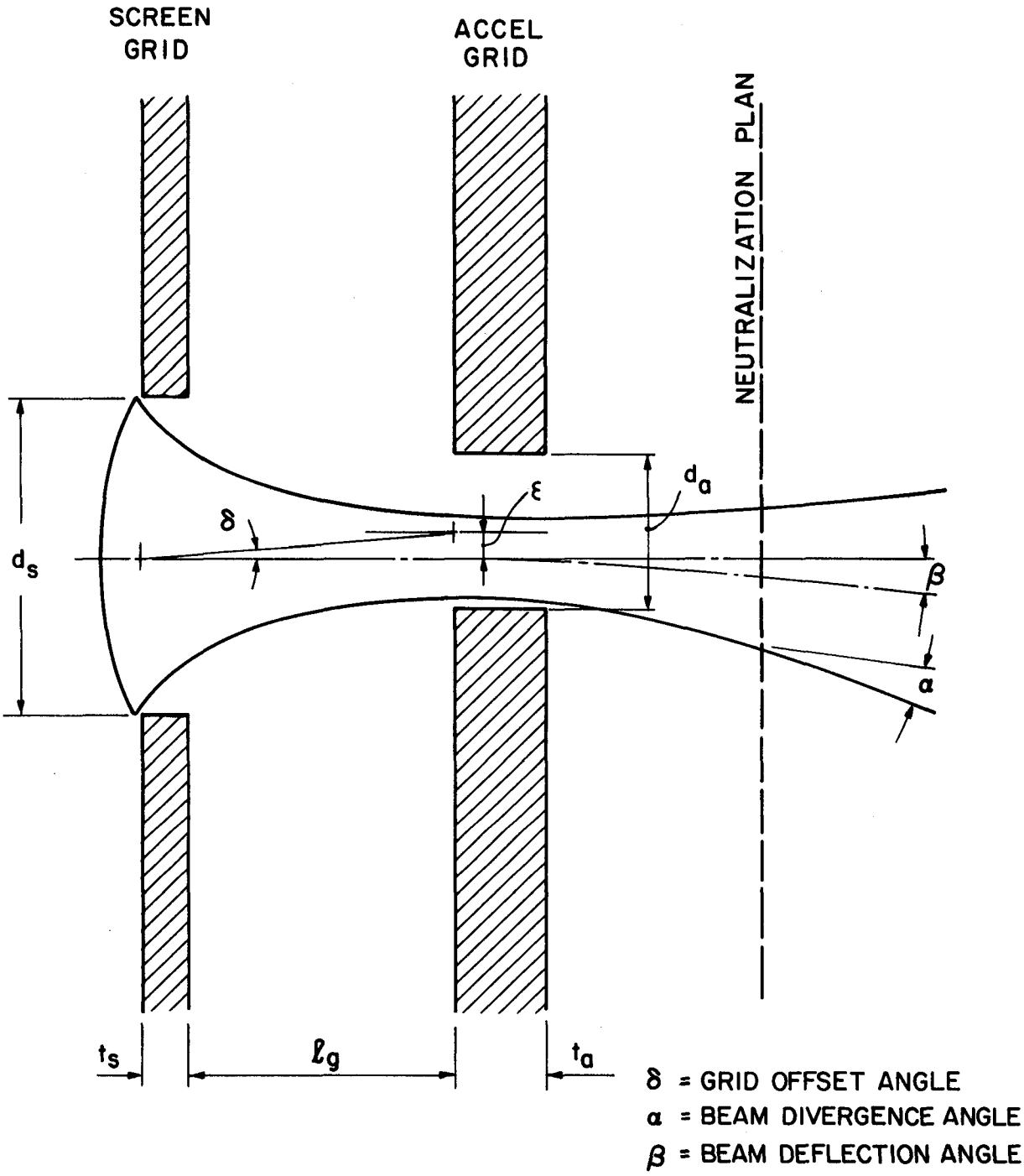

Figure 14. Deflecting Beamlet Nomenclature.

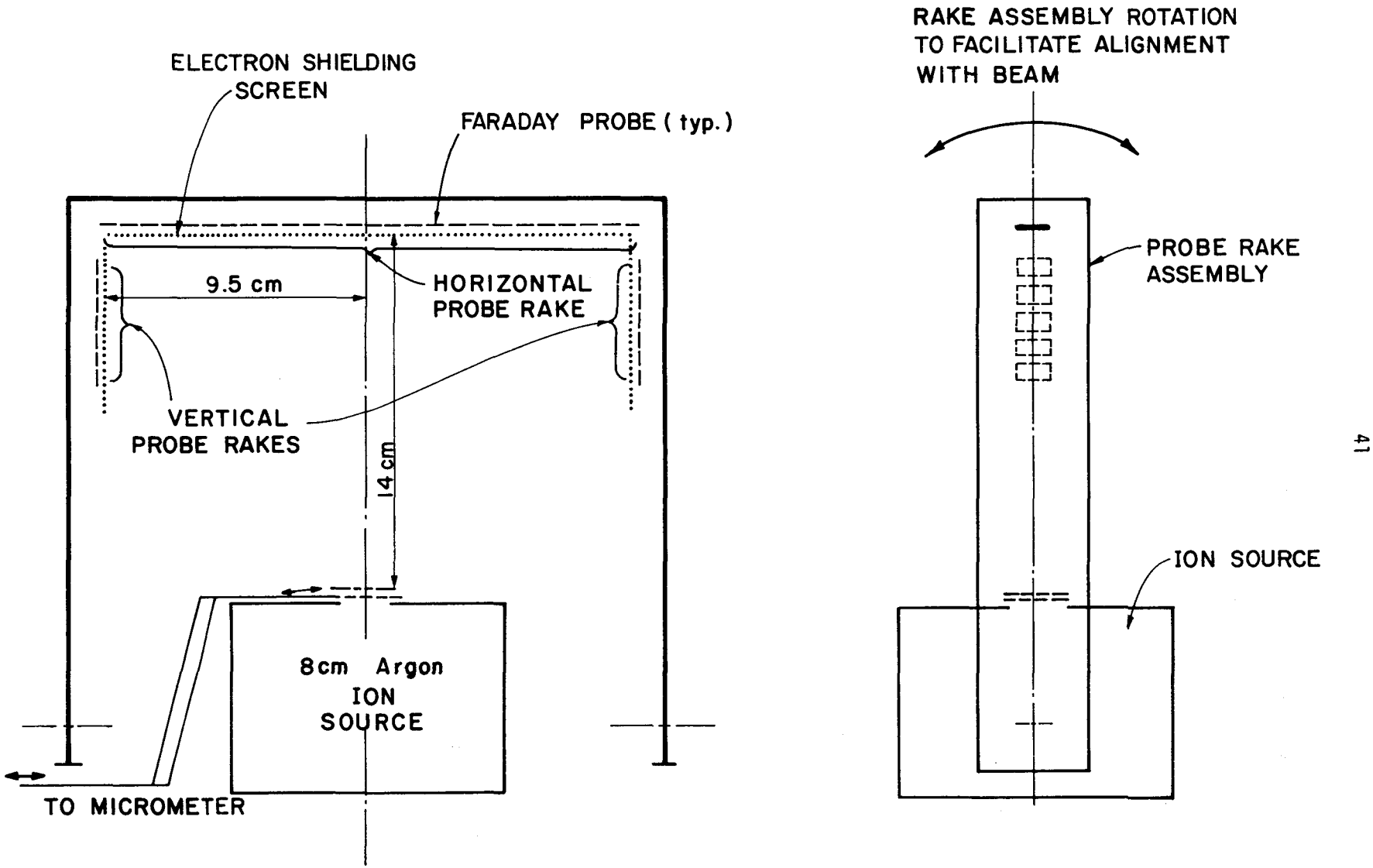

Figure 15. Deflecting Beamlet Test Apparatus.

selected as the translating grid, because such an arrangement facilitated grid spacing and accelerator grid alterations.

The beam emerging from the grids is probed by a collection of molybdenum, flat plate probes each 1 cm^2 in area, arranged in the manner suggested in Figure 15. Twenty of these probes are situated along a horizontal line 14 cm downstream from the grids. In addition, a line of probes extends vertically downward from each end of the horizontal probe rake. By using these three probe rakes it is possible to intercept the full beam profile over the complete range of grid translation. A 70% open area screen is placed in front of the probes, and is biased 24 v negative relative to ground in order to reflect neutralizer electrons. The probes themselves are biased 18 v positive relative to ground to reflect low energy, charge-exchange ions produced downstream of the grids. The rake assembly is designed so it can be rotated in the manner suggested in Figure 15 to facilitate rake axis alignment with the beam axis in the plane perpendicular to the direction of grid translation. Data was initially collected using only the horizontal probe rake, however beam profiles for vectored beams showed significant currents being collected on the end probes. The vertical probe rake elements were then added to ensure that the entire beam profile was being sensed.

A complete set of beam profiles is collected by first achieving stable ion source operation with the screen grid displaced to produce a substantial negative ion beam deflection. Once the ion beam has been probed, the screen grid is displaced in 0.05 mm increments and the beam is probed after each displacement. This process continues until the beam is displaced sufficiently positive so the accelerator grid impingement current reaches $\sim$ 25% of the beam current. Since a grid displacement of 0.05 mm has been shown to produce measurable beam deflection, careful alignment of the grids in the

direction perpendicular to the direction of grid translation and reduction of play in the movable grid are crucial to the generation of accurate data.

Beam current density profiles are analyzed using a computer routine. This routine first uses the current density data obtained from the three segment probe rake to compute the current density on a circular arc located 17 cm from the grid center. From this profile the point of maximum current density is identified. The deflection angle is then computed as the angle between the thruster axis and the line from the screen grid center through the point of maximum current density. Next the two segments of the current density profile on either side of the maximum are averaged and the total beam current is estimated by integrating this average profile for an assumed axi-symmetric distribution about the line of maximum current density. Inherent in this portion of the analysis is the assumption that the ions are drawn from a point source; this assumption does not introduce a significant error because the initial beam diameter is small compared to the distance to the probe rake. The beam current obtained in the analysis by integrating the current density is compared to the measured beam current to insure that they agree to within 5-10%. If they do not the data are discarded. The divergence angle (α in Fig. 14) is computed as the half angle of the cone enclosing 95% of the integrated beam current determined in the aforementioned analysis. This definition of half angle is the same as the one used in previous work.[7,10] The 95% criterion was selected as a compromise value that yielded a sensitive indicator of ion beam divergence. A thrust coefficient defined as the fraction of the integrated ion current that is directed along the deflected beam axis is also computed.

Initially current density data were collected manually by reading a meter that could be switched to read each Faraday probe in the rake.

These results showed the linear relationship between the grid offset angle (ε) and the deflection angle (β) suggested by Eq. (9) but, inconsistencies were observed when data from various runs were compared. It was determined that these inconsistencies were due in part at least to variations in ion source operating conditions that occurred while the probe currents were being read. In order to minimize this drift the manual data collection was eliminated in favor of automated collection using a Hewlett Packard 3054 Data Logger. Results obtained using the data logger have been very reproducible and self-consistent.

In order to isolate the effects of various parametric changes to be introduced in the experiment a standard grid geometry was selected and then one grid parameter was varied while other parameters were held at their standard value. The standard case selected is defined by the following geometrical and operating conditions:

Screen hole diameter (d_s)	2.06 mm
Total accelerating voltage (V_T)	600 volts
Net-to-total accelerating voltage ratio (R)	0.7
Screen grid thickness ratio (t_s/d_s)	0.185
Accelerator grid thickness ratio (t_a/d_s)	0.370
Accelerator grid hole diameter ratio (d_a/d_s)	0.642
Grid separation ratio (ℓ_g/d_s)	0.494

As suggested by the above list, the geometrical grid parameters of Fig. 14 are normalized using the screen hole diameter, which was held constant at 2.06 mm for all tests. The range of variation of the parameters to be investigated in this study are:

Total accelerating voltage	600 - 1100 volts
Net-to-total accelerating voltage ratio	0.5 - 0.9
Screen grid thickness ratio	0.123 - 0.370
Accelerator grid thickness ratio	0.123 - 0.740
Accelerator grid hole dia. ratio	0.642 - 1.00
Grid separation ratio	0.247 - 1.20

In addition, the discharge voltage is being maintained at 40 v and the bell jar pressures are being held between 6 - 8 x 10^{-6} torr. An argon flow rate of 10 mA equivalent is being used throughout the experiments because it is sufficiently high to produce stable discharge chamber operation while being low enough to keep the charge exchange ion production less than one percent of the beam current.

RESULTS

A typical beam ion current density profile collected in the manner outlined in the previous section is shown as Figure 16a. As this figure suggests the profiles are relatively symmetrical; not apparent is the observation that they retain this symmetry over a wide range of beam deflections. Using the information on this profile one can determine the beamlet divergence and deflection associated with this particular operating condition. The deflection angle is for example the arc tangent of the profile offset defined in the figure divided by seventeen cm. (the distance from the grids to mean sensing location for the current density). The quantity "NP/H" represents the normalized perveance per hole at which the grid is operating and is defined by Eq. 5a. A typical plot of deflection angle against grid offset angle is presented as Figure 16b; this one for the standard grid set operating at a perveance 1.02 x 10^{-9} $A/V^{3/2}$. This plot shows the expected

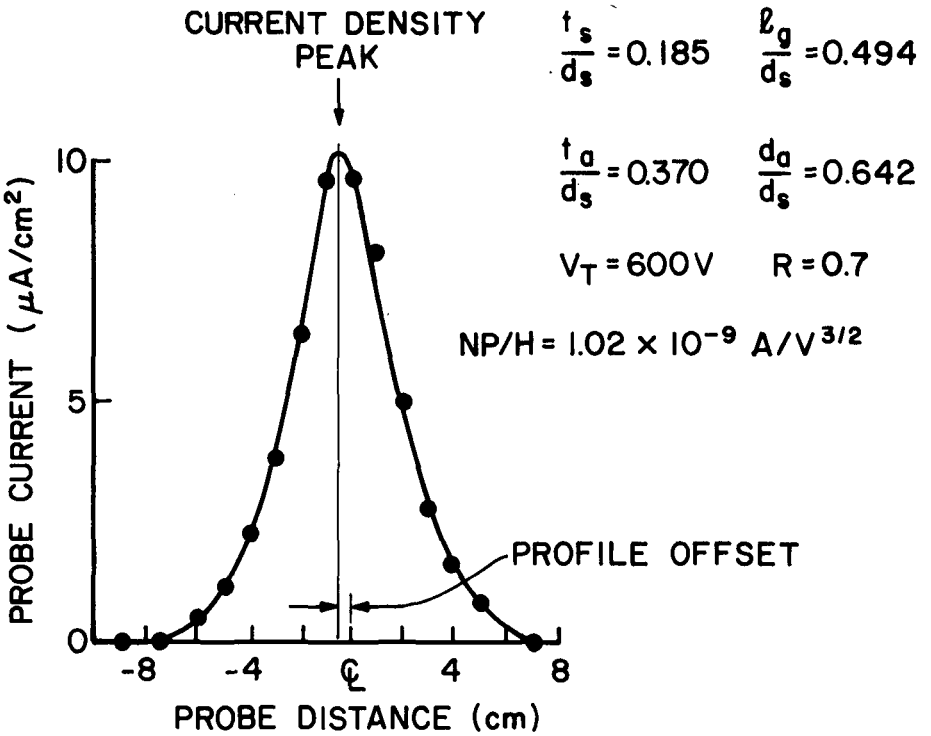

a. BEAM CURRENT DENSITY PROFILE

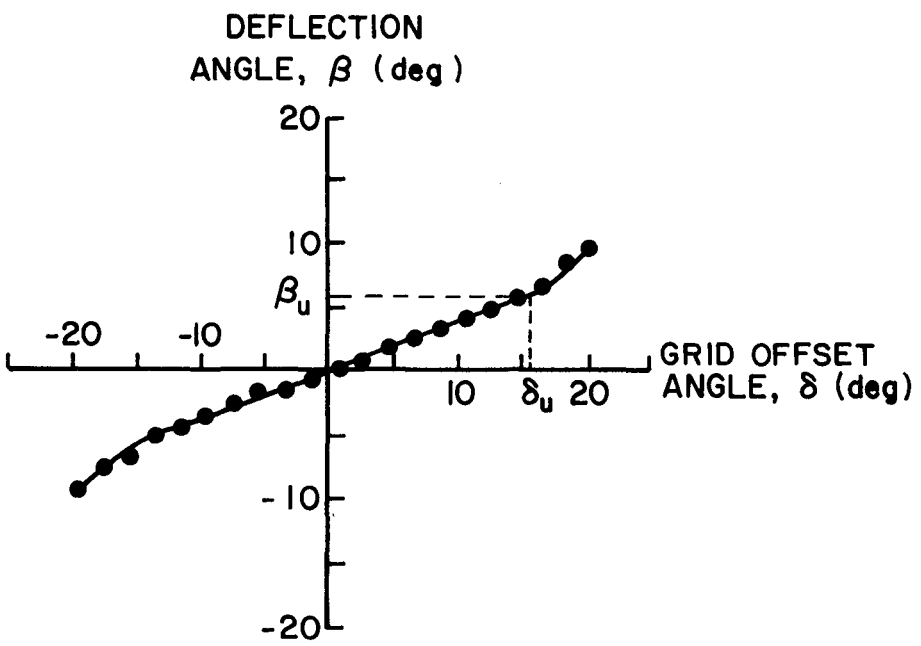

b. DEFLECTION CHARACTERISTIC

Figure 16. Typical Standard Grid Results.

linear relationship between beam deflection angle (β) and grid offset angle (δ) up to $\sim$ 15° where the beamlets begin to intercept the accelerator grid.

The deflection angle at the onset of this non-linear behavior is designated β_u (for β useful), as suggested on Figure 16b. The data shown is for an accelerator grid hole diameter ratio of 0.642. At accelerator hole ratios near 1.00 the beam deflection beyond β_u levels off rather than increasing as shown in Figure 16b. This change in the slopes above the point where impingement begins to increase is probably related to the observation that the beam profiles become increasingly asymmetrical at high grid offset angles for grids having larger accelerator grid hole ratios. It should be noted however that the non-linear beam deflection always occurs at relatively high impingement levels outside of the normal thruster operating regime.

Figures 17a and b show typical divergence and impingement characteristics for the same grid set that gave the data of Figure 16. It can be seen here that the divergence angle (α) does not vary significantly over the useful range of grid offset angles where the impingement currents are acceptably low and operation would normally occur. With a larger accelerator grid hole diameter ratio, the divergence angle drops slightly from the value at a significant offset to a minimum zero offset. Even in this case however the total variation in divergence angle over the useful range of grid offset angle has not exceeded two degrees. The rapid decrease in divergence angle apparent in Figure 17a at large grid offset angles is probably due to interception of the most divergent ions from the beamlets by the accelerator grid. In Figure 17b this rapid increase in accelerator grid impingement current is apparent and it defines the range of useful grid offset angles (δ_u). In order to quantify this range it is defined here rather arbitrarily as

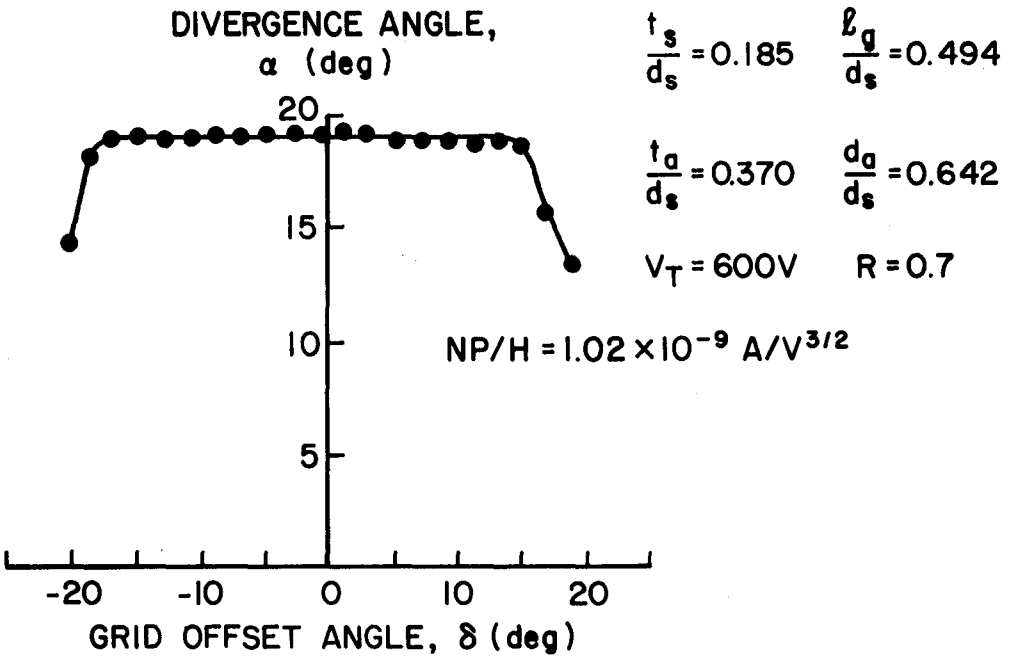

a. DIVERGENCE ANGLE DATA

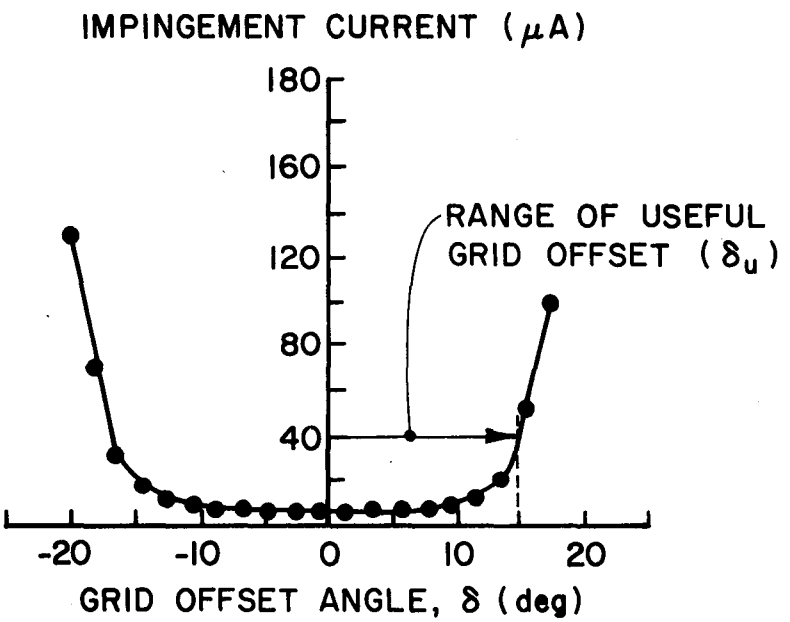

b. ACCELERATOR GRID IMPINGEMENT DATA

Figure 17. Typical Standard Grid Data.

the grid offset angle at which the impingement current reaches 10% of the beam current. At this same limit the beam deflection angle reaches its limiting value (β_u) as indicated in Figure 16b. Finally, with regard to Figures 16 and 17 it is important to note the symmetry the data they contain exhibits. This symmetry is considered indicative of the consistency of the experimental results.

The useful range of the grid offset angle (δ_u) is a function of both the geometrical parameters of the grids and perveance at which they are operating. Figure 18 illustrates the effect of perveance on typical impingement current vs. grid offset angle plots. The two values of useful range of grid offset angle (δ_u) appropriate to the two levels of perveance are identified and they show this limiting offset angle drop as perveance is increased. This presumably occurs because the beamlet more nearly fills the accelerator grid aperture at the higher perveance level.

Using data like those shown in Figures 16b and 17a and b one can define a group of parameters that characterize the optical behavior of deflected ion beamlets. The parameters that have been selected for use here are:

1. The useful ion beamlet deflection range (β_u)
2. Divergence angle in the useful range (α)
3. The grid deflection-to-offset angle ratio (β/δ)

The assumption that a single divergence angle characterizes the beamlets over the range of useful deflection (2 above) is supported by the results of Figure 19. These results, which are typical of those obtained to date, show that divergence angle is independent of grid offset over the full range of perveance. It is also noteworthy that the results of Figure 19 agree to within $\sim 1°$ with those obtained by Aston[10] using aligned grids.

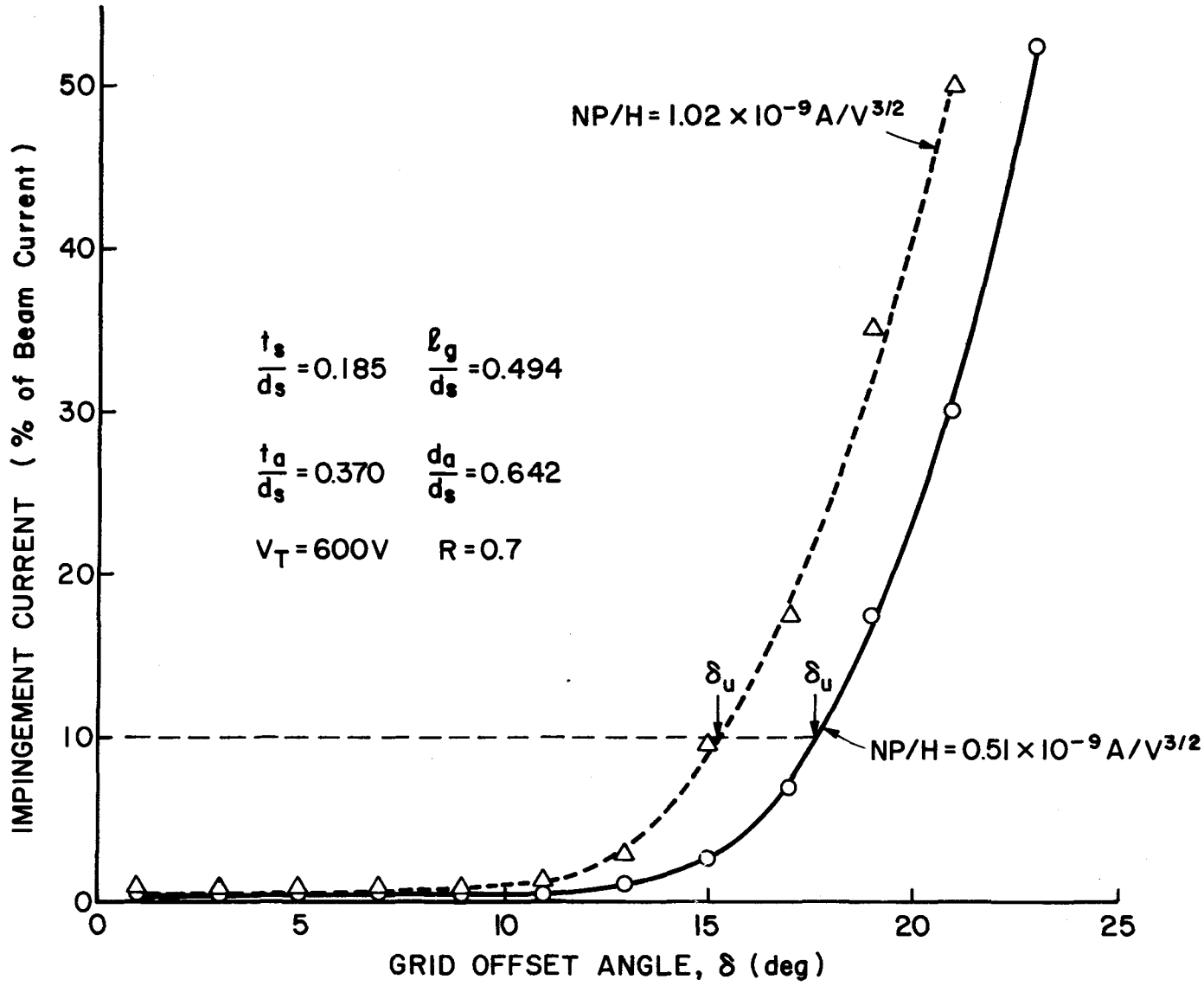

Figure 18. Effect of Grid Offset on Impingement Current.

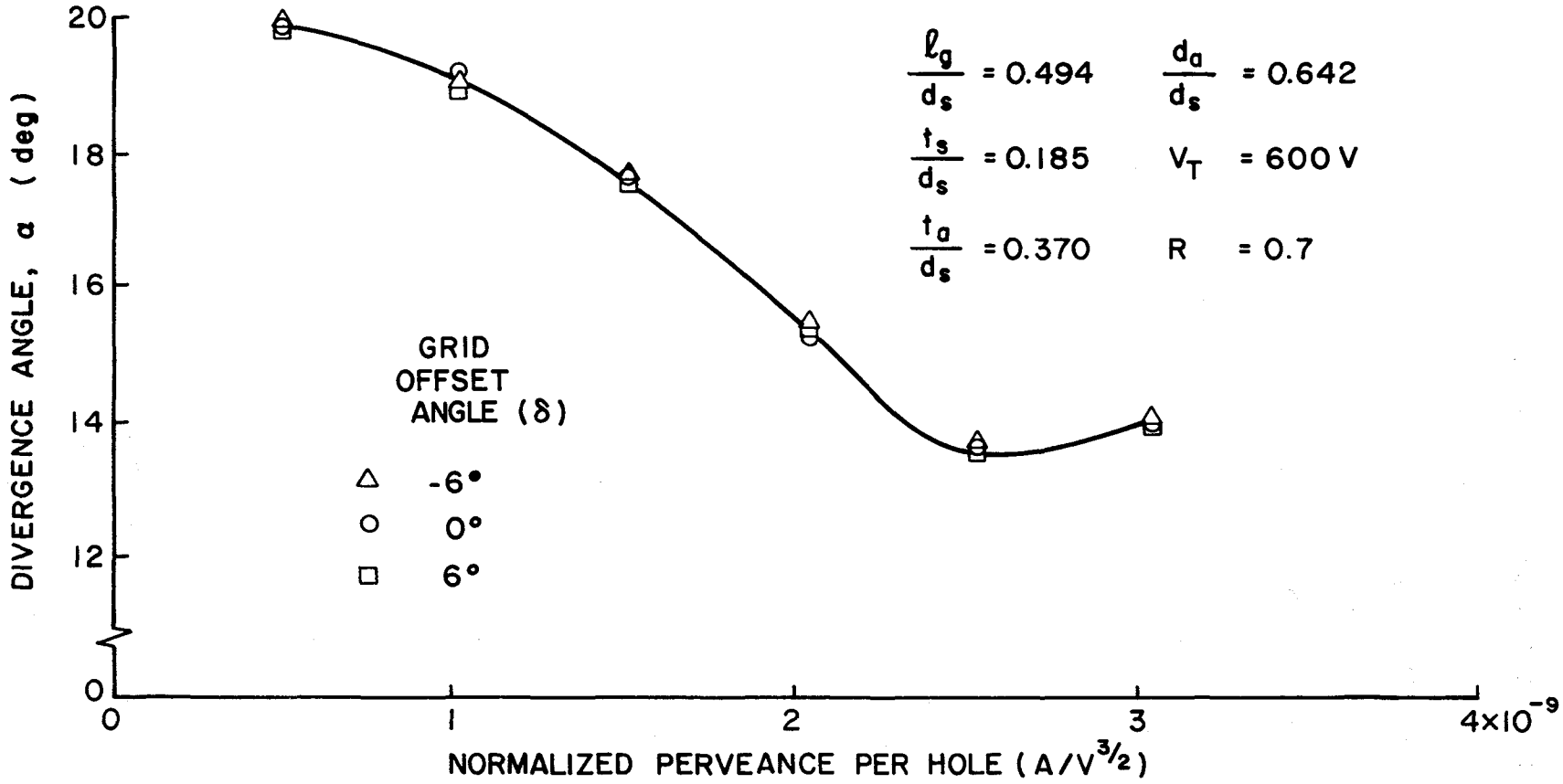

Figure 19. Effect of Offset on Divergence.

Figures 20 and 21 show the effects of net-to-total accelerating voltage ratio (R) and the grid separation ratio (ℓ_g/d_s) on the divergence characteristics of the grids. These curves again agree with results obtained by Aston[10] to within $\sim 1°$ of divergence angle except at high perveance levels where the present results differed from Aston's by $\sim 2°$ of divergence angle. In making these comparisons it should be remembered that perveances computed in Figures 19 through 21 use the new definition of effective acceleration length discussed in Appendix A while Aston's original results used the old definition.

All data obtained to date suggest that the beamlet deflection varies linearly with grid offset over the useful deflection range. Therefore the slope of this linear region (β/δ) is an important parameter that can be used to compare deflecting beamlet characteristics. Figures 22 and 23 show the effects of perveance and net-to-total accelerating voltage ratio on this ratio and both variables are observed to exert a minor influence on the ratio. The magnitude of slopes β/δ is in good agreement with the results obtained by Stewart, et al.[16] Referring to Eq. 10, it is seen that for a given grid displacement ε, the grid offset angle δ will vary with grid separation ratio (ℓ_g/d_s). So, while the deflection angle-to-grid offset displacement (β/ε) changes with the grid separation distance (ℓ_g) the ratio of deflection to offset angles (β/δ) is seen in Figure 23 to be independent of grid separation. This confirms the suitability of this ratio as a correlating factor.

The range of useful beam deflection (β_u) is a very important parameter required by designers; however, its definition is somewhat arbitrary, depending on the allowable accelerator grid impingement current for the design being considered. For results presented herein this range is defined

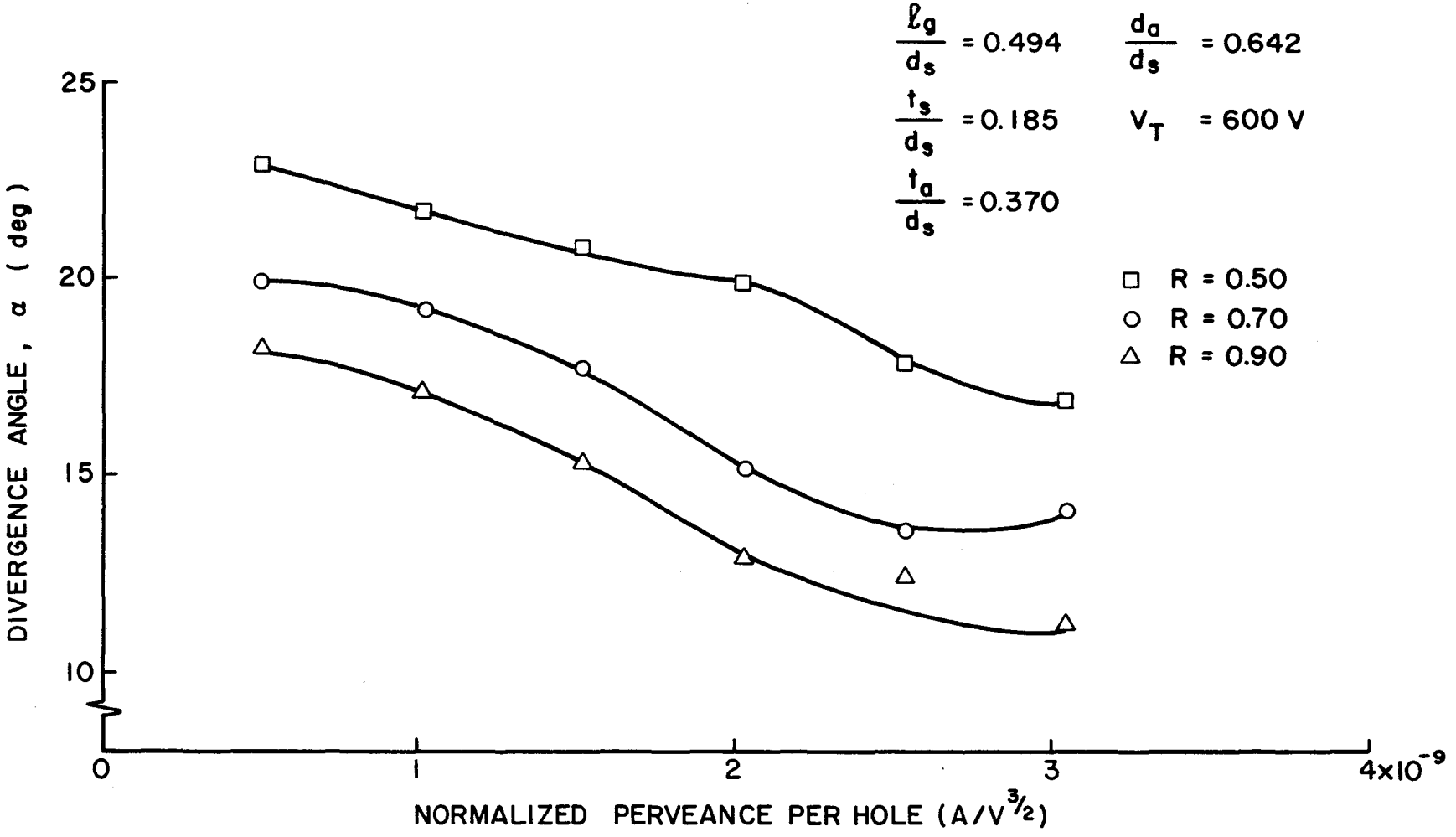

Figure 20. Effect of Net-to-total Accelerating Voltage on Divergence.

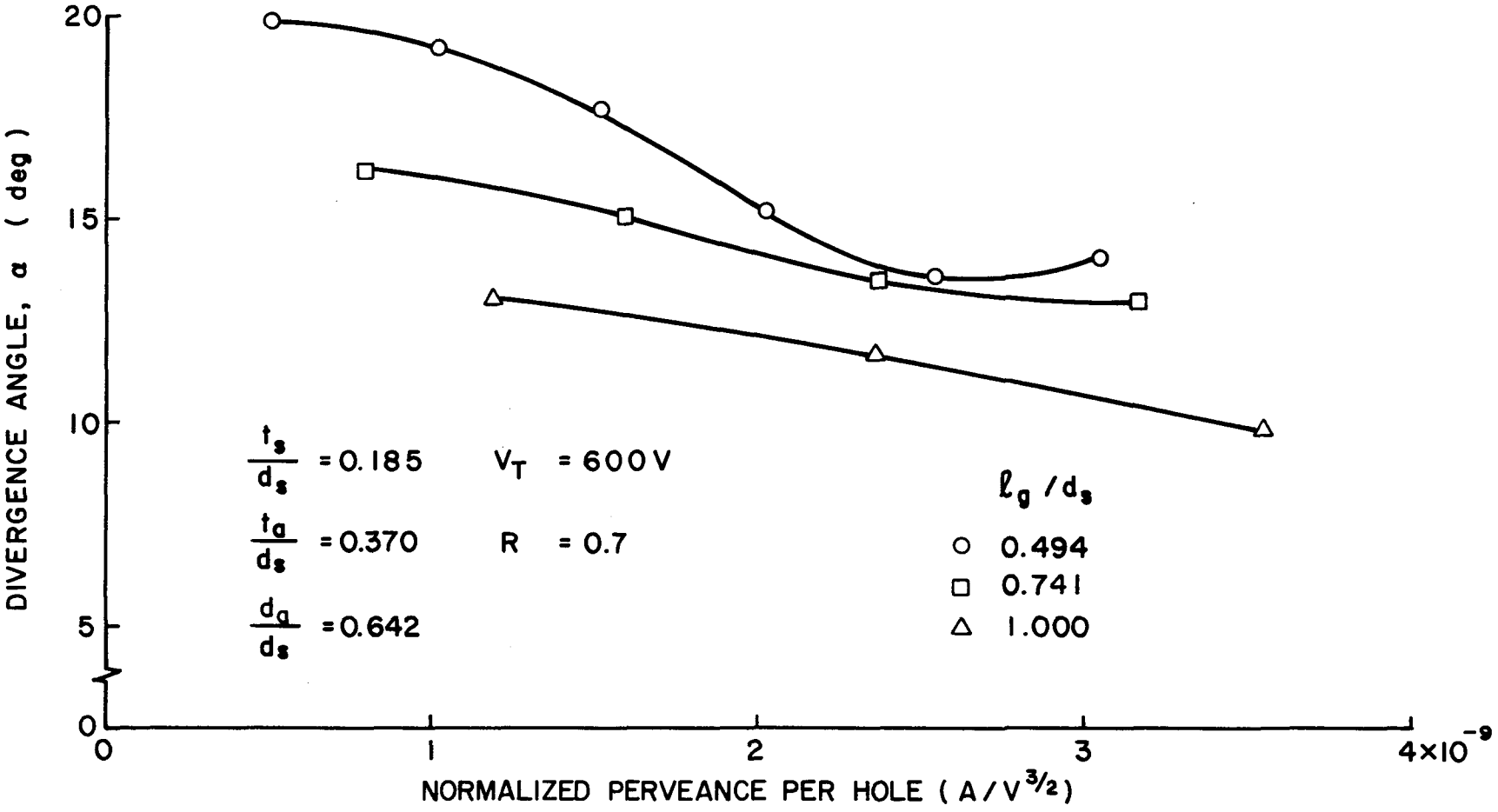

Figure 21. Effect of Grid Separation Ratio on Divergence.

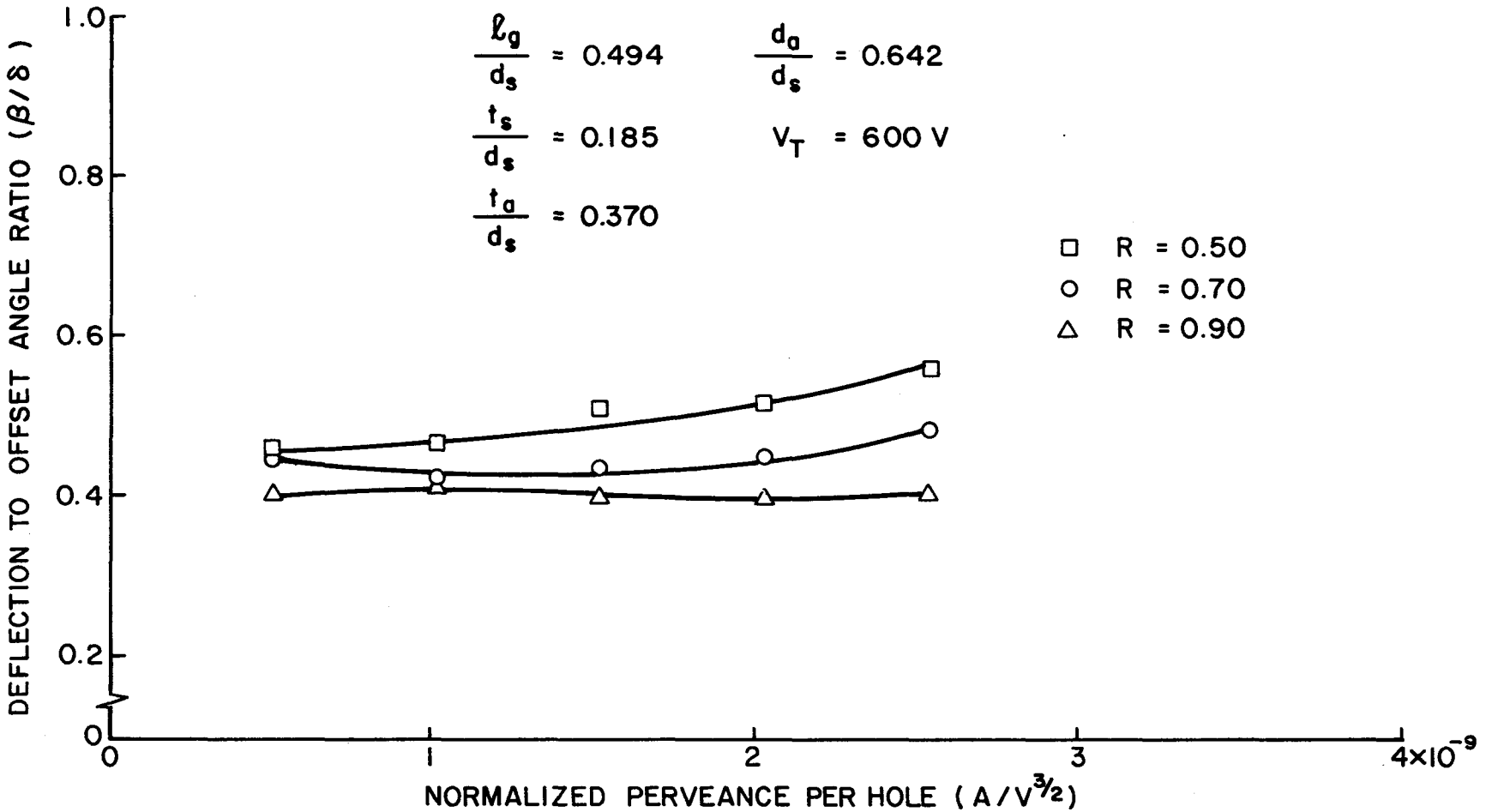

Figure 22. Effect of Net-to-total Accelerating Voltage Ratio on Deflection to Offset Angle Ratio.

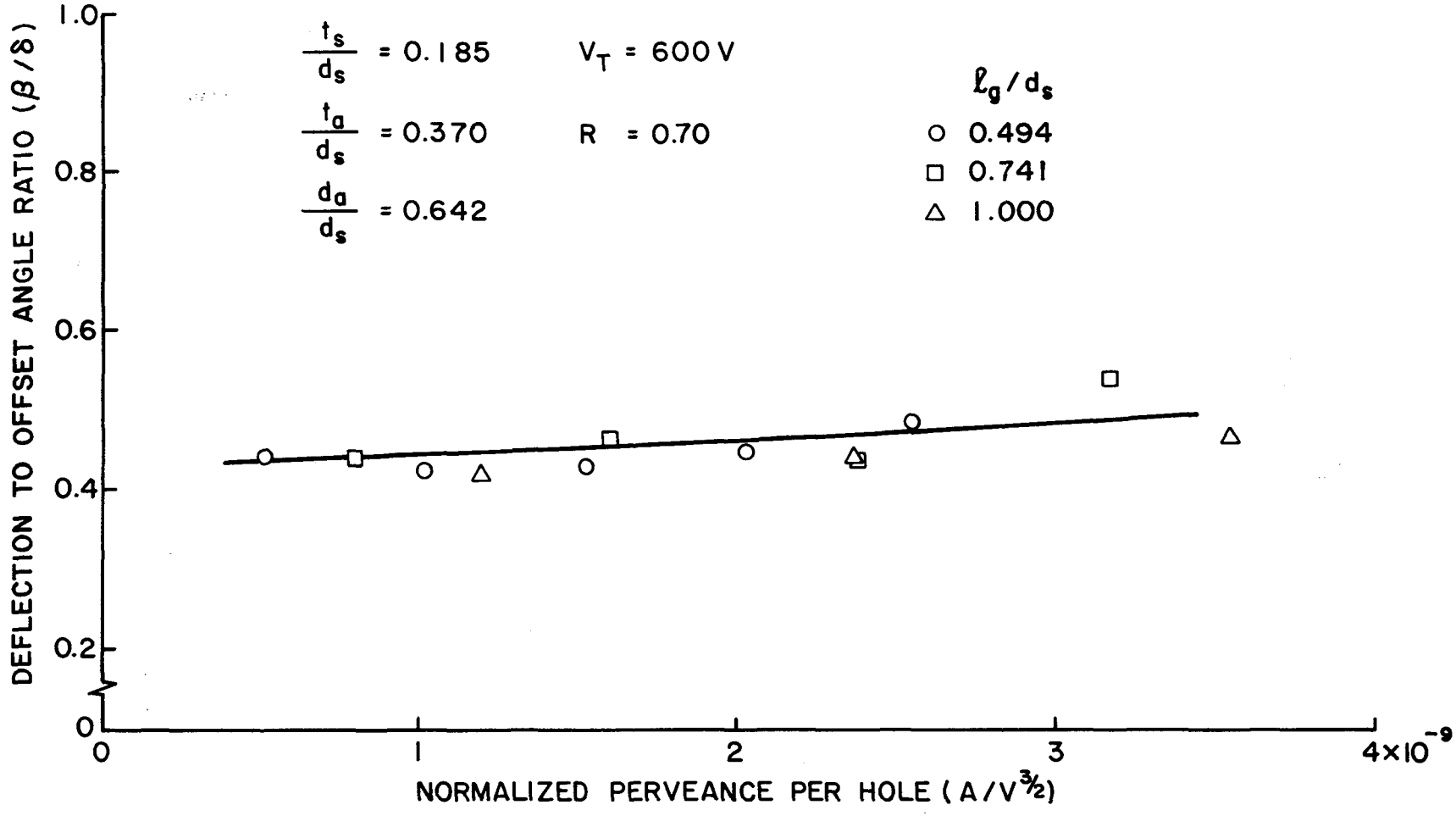

Figure 23. Effect of Grid Separation Ratio on Deflection to Offset Angle Ratio.

for a 10% impingement limit (impingement current 10% of beam current). Although this may be high for some applications, the rise in impingement with grid offset is fairly rapid and therefore β_u will not vary greatly for different impingement limits. Figures 24 and 25 show the effects of net-to-total acceleration voltage ratio, perveance and grid separation ratio on the range of useful deflection angles. This range is seen to decrease substantially as perveance increases. Increases in accelerating voltage ratio and grid separation ratio are also observed to reduce the deflection angle range although their effect is generally less significant.

CONCLUSIONS

Ion beamlet deflections over a range of several degrees can be effected by displacing the screen and acceleration grid holes relative to each other. The deflection is limited to this useful range by the onset of high accelerator grid impingement currents. This range is dependent on the perveance at which the grid is operating, and to a lesser extent on the net-to-total accelerating voltage ratio and the normalized grid separation distance. This observation suggests a potential problem with large diameter multipole thrusters that may not have been recognized and is worthy of mention. In large thrusters, relatively large offset angles may be required at the apertures on the outer edges of the grids. For divergent field thruster designs the perveances at these outer hole sets are relatively small because of the peaked plasma density profile in the discharge chamber and therefore impingement at the outer holes may not be severe. For multipole thrusters however the flatter plasma density profiles would be expected to cause higher perveance and hence greater impingement at these outer holes.

Over the useful range of beam deflections the beamlet divergence angle is independent of deflection. In this range the deflection angle is

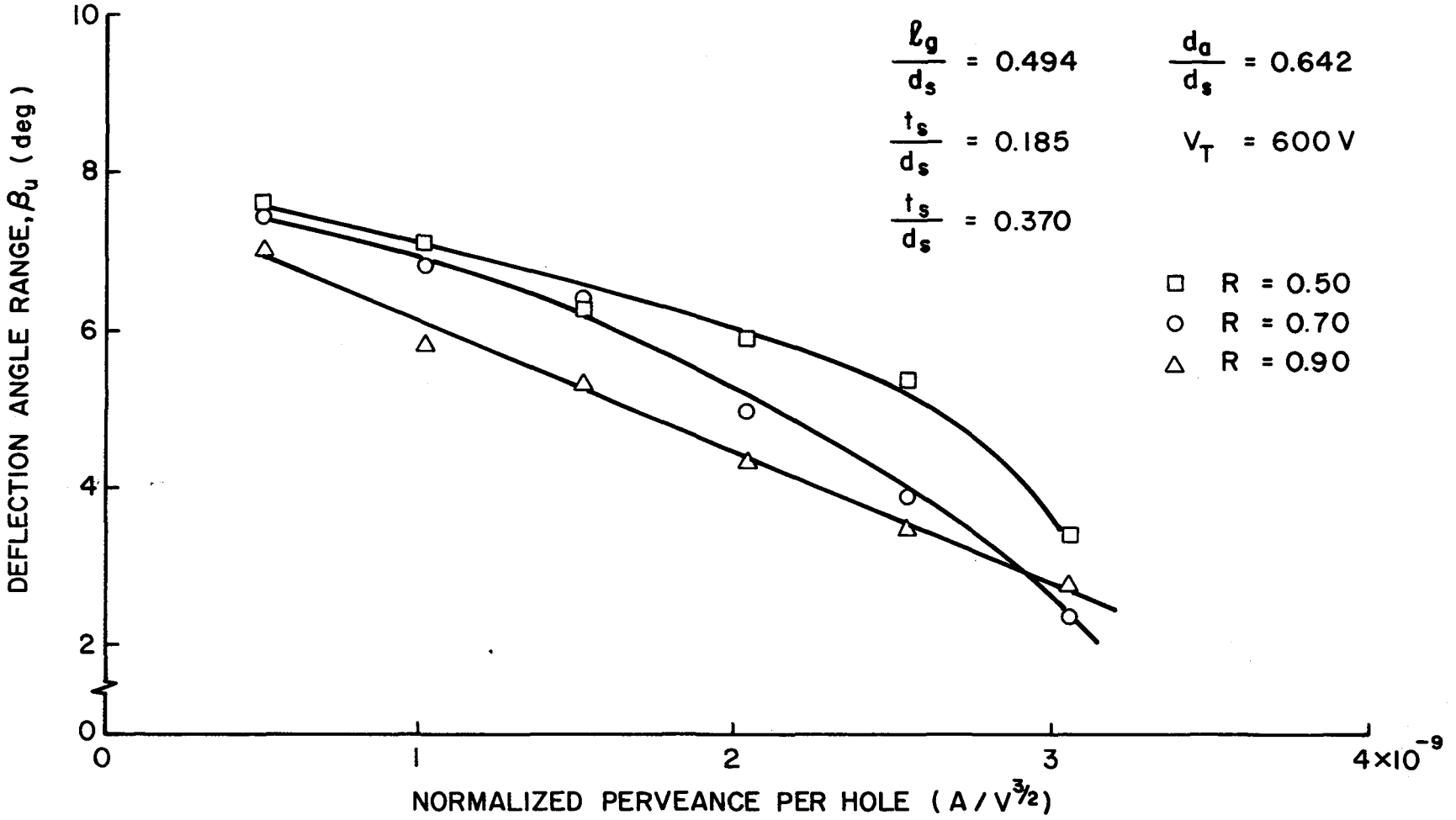

Figure 24. Effect of Net-to-total Accelerating Voltage Ratio on Deflection Angle Range based on 10% Impingement Limit.

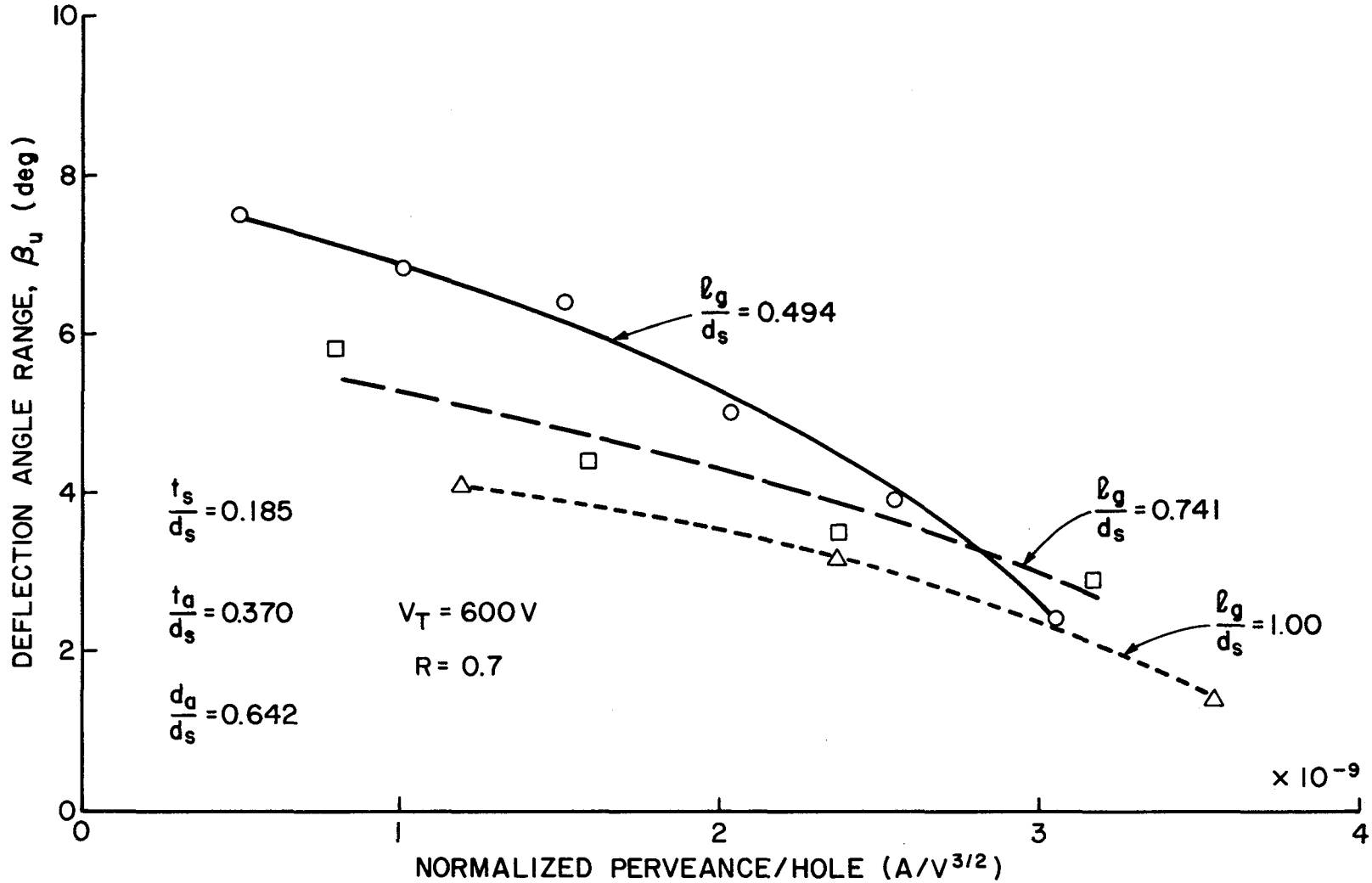

Figure 25. Effect of Grid Separation Ratio on Deflection Angle Range based on 10% Impingement Limit.

also a linear function of the grid offset angle. The constant of proportionality between these angles shows a mild dependence on the net-to-total accelerating ratio but is relatively independent of grid separation ratio and perveance. It is noted that this study is incomplete in that the full range of variation of such parameters of interest as grid thickness and accelerator grid hole diameter has not yet been accomplished.

THE HOLLOW CATHODE EMISSION MECHANISM

Dan Siegfried

Previous work performed under this grant resulted in the development of a phenomological model describing the electron production processes taking place within the orificed, hollow cathode.[17] A key assumption in this model is that the dominant surface emission mechanism is field-enhanced, thermionic emission. This report will discuss an experiment which provides additional support for the validity of this assumption.

BACKGROUND

The electron current density (j_e) from a surface emitting electrons due to field-enhanced, thermionic emission is described by the following equation

$$j_e = A_o T^2 \exp\left(\frac{-e\bar{\phi}_e}{kT}\right) \tag{11}$$

where A_o is a theoretical constant equaling $120 A/cm^2 °K^2$, T is the surface temperature, e is the electronic charge, and k is Boltzmann's constant. The average effective work function $\bar{\phi}_e$ is given by

$$\bar{\phi}_e = \phi_s - \left(\frac{e\,|E|}{4\pi\varepsilon_o}\right)^{\frac{1}{2}}$$

where ε_o is the permittivity of free space, E is the electric field adjacent to the surface and ϕ_s is the surface work function (a material property). In the model, the electric field is estimated using

$$E = \frac{-dV}{dx} = \frac{-4}{3}\frac{V_p}{\lambda_D} = \frac{-4}{3} V_p \left[\frac{ne^2}{\varepsilon_o kT_e}\right]^{\frac{1}{2}} \tag{13}$$

where the sheath thickness is estimated as one Debye length (λ_D), the factor of 4/3 comes from Child's Law considerations, V_p is the plasma potential, T_e is the electron temperature °K, and n is the plasma density.

The previous evidence indicating that the surface emission mechanism is field-enhanced, thermionic emission was based primarily on the ability of the model to predict reasonable values of the surface work function (ϕ_s), given experimentally determined values of the plasma properties, the surface temperature, and the emission current density. The surface work function is a material property of the emitting surface, and so if the model is valid, the calculated work function should agree with the expected value of this parameter for the insert material used in the experiments. The initial experiments[17] employed to check the model used insert segments $\sim$ 2 mm long. The results of these experiments, which were based on a large number of data points describing average conditions on these insert segments, provided average surface work functions ranging from 1.7 to 2.25 eV which increased linearly with temperature. A surface work function of $\sim$ 2.0 eV is quite reasonable for tantalum coated with the chemical R-500* used in the experiments and agrees with tabulated values for these materials. Fomenko[18] in an excellent summary of work function data gives values ranging from 1.5 eV for tantalum coated with barium oxide to an average of $\sim$ 2.7 eV for various barium and strontium tantalates. Further, a surface work function which is a linearly increasing function of the surface temperature is expected when the theoretical constant for A_0(120 A/cm^2°K^2) is used to calculate ϕ_s from the Schottky equation. In this case ϕ_s is known as the "true" work function, as opposed to the "Richardson" work function which is not a function of temperature but relies on an empirically determined value for the constant A_0. The relationship between these two work functions is discussed in Ref. 19.

---

* A double carbonate mixture - (Ba/Sr) CO_3 - manufactured by the J. T. Baker, Co.; Phillipsburg, New Jersey

EXPERIMENTAL DETERMINATION OF THE SURFACE WORK FUNCTION

The experimental results of Ref. 17 indicate that the field-enhanced, thermionic emission process is characterized by a work function that is reasonable because of its magnitude and its linear dependence on temperature. However, these were average results based on a relatively large emitting surface area. Because of this and because the emission current shows an exponential sensitivity to the work function, this evidence alone was not considered sufficient to permit one to state conclusively that field-enhanced, thermionic emission was the dominant emission mechanism acting. It was felt that such a judgement might be made, however, if the actual work function were accurately known for the emitting surface. One method of determining this work function would be to make an independent measurement of the work function of a small sample of the emitting surface without the discharge present. This work function could then be compared with the surface work function of the same sample area calculated using the hollow cathode model based on data from the operating cathode. Because of the extreme sensitivity of the surface work function to contamination and operating history, it was considered imperative that this measurement be made without having to remove the insert from the cathode. An experiment to perform such an in-situ measurement was designed; the basic features of the appartus used in this test are illustrated schematically in Figure 26. The sample area for the test was a tantalum "patch" $\sim$ 2 mm square and 0.125 mm thick coated with R-500. The patch had three, 0.25 mm diameter leads consisting of a platinum/platinum 13% rhodium thermocouple pair and a lead for measuring the emission current. The patch was electrically isolated from the insert and the rest of the cathode. The basic procedure for the experiment was to operate the cathode in the normal

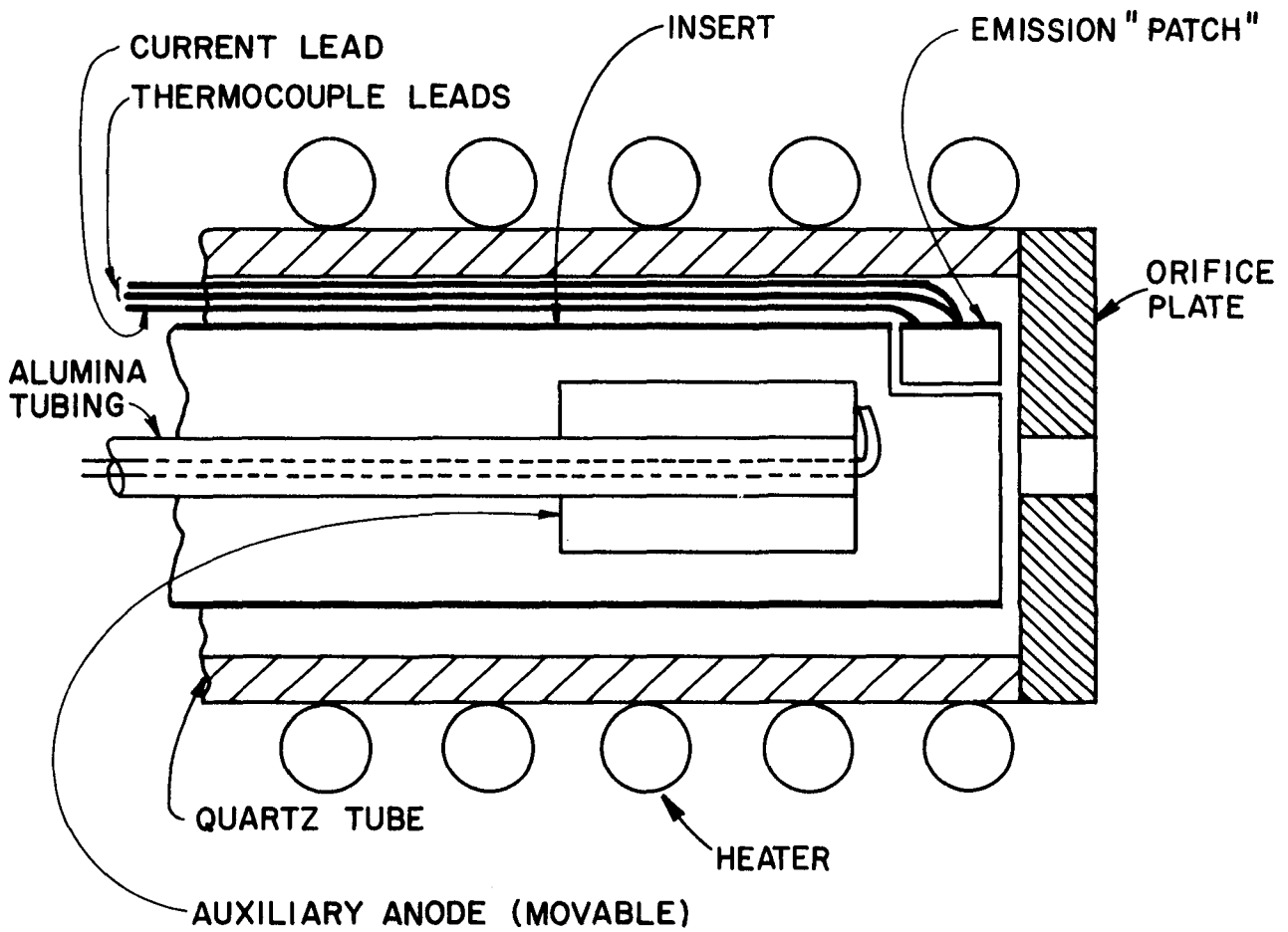

Figure 26. Apparatus for In-Situ Measurement of Patch Work Function.

manner while making measurements of patch temperature, emission current, and plasma properties. The discharge and flow were then turned off and a conventional surface work function test was performed in which the cathode was heated using the external heater and the patch emission current was collected using the auxiliary anode.

This experiment was attempted a number of times without much success because it was very difficult to establish electron emission reliably from the patch while the cathode was operating. This was due to difficulty in maintaining a sufficiently low work function at the patch surface for a long enough period to conduct a complete experiment. The assumption of uniform surface work function and emission current density are idealizations. Apparently the work function of the insert surfaces show rather strong local variations, with the emission tending to take place predominantly from sites having the lowest work function. Although every effort was made to get uniformly thin low work function coatings and to activate them by raising their temperature before operation, coating irregularities may have contributed to these non-uniformities. There were occasions when the patch was apparently a low work function site and would emit. However, when this occurred the tendency was for most of the cathode emission to come from the patch. This caused a rather high patch temperature which resulted in a gradual depletion of barium from the patch causing the emission site to shift eventually to another location. It was impossible to complete an experiment with consistent results under these conditions. This problem was finally circumvented by using a separate power supply to bias the patch negative with respect to cathode potential, and thereby establish electron emission from the patch. The emission process was facilitated when this procedure was followed because the power supply increased the sheath potential drop at

the patch. This raised the patch temperature due to increased ion heating and also increased the electric field adjacent to the patch thereby increasing the field-enhancement of the emission process. The fact that the patch frequently ceased emitting under normal conditions is now seen as beneficial. When this occurred the patch could be used both as a probe to sense plasma conditions at the cathode wall (these are necessary inputs to the model) and then, when it was biased negatively as a test surface from which electron emission could be measured. The experiment was conducted by operating the cathode in the normal manner and recording a current-voltage characteristic while the patch was biased from +5 v to -35 v relative to cathode potential. The procedure and data analysis for this are discussed in Appendix B. Using data collected from the patch in the field-enhanced, thermionic emission mode, the work function of the surface was computed based on the model. These work function results are shown as the open symbols in Figure 27. As the figure suggests, this test was conducted three times and at two separate discharge current levels. The solid symbols in Figure 27 correspond to a conventional surface work function test in which the propellant flow was stopped, the emission current was collected at the auxiliary anode (Fig. 26) and the Richardson-Dushmann equation[19] was used to compute the surface work function.

The results shown in Figure 27 indicate that the test patch has a surface work function of approximately 2.7 eV both with and without a discharge present. Considering the exponential sensitivity of the emission current to the work function, the scatter of the data about this mean value is rather large. However, it is felt that this is due to experimental variation in the work function rather than a failure of the model. The data in fact show that the work function probably did vary both during the course

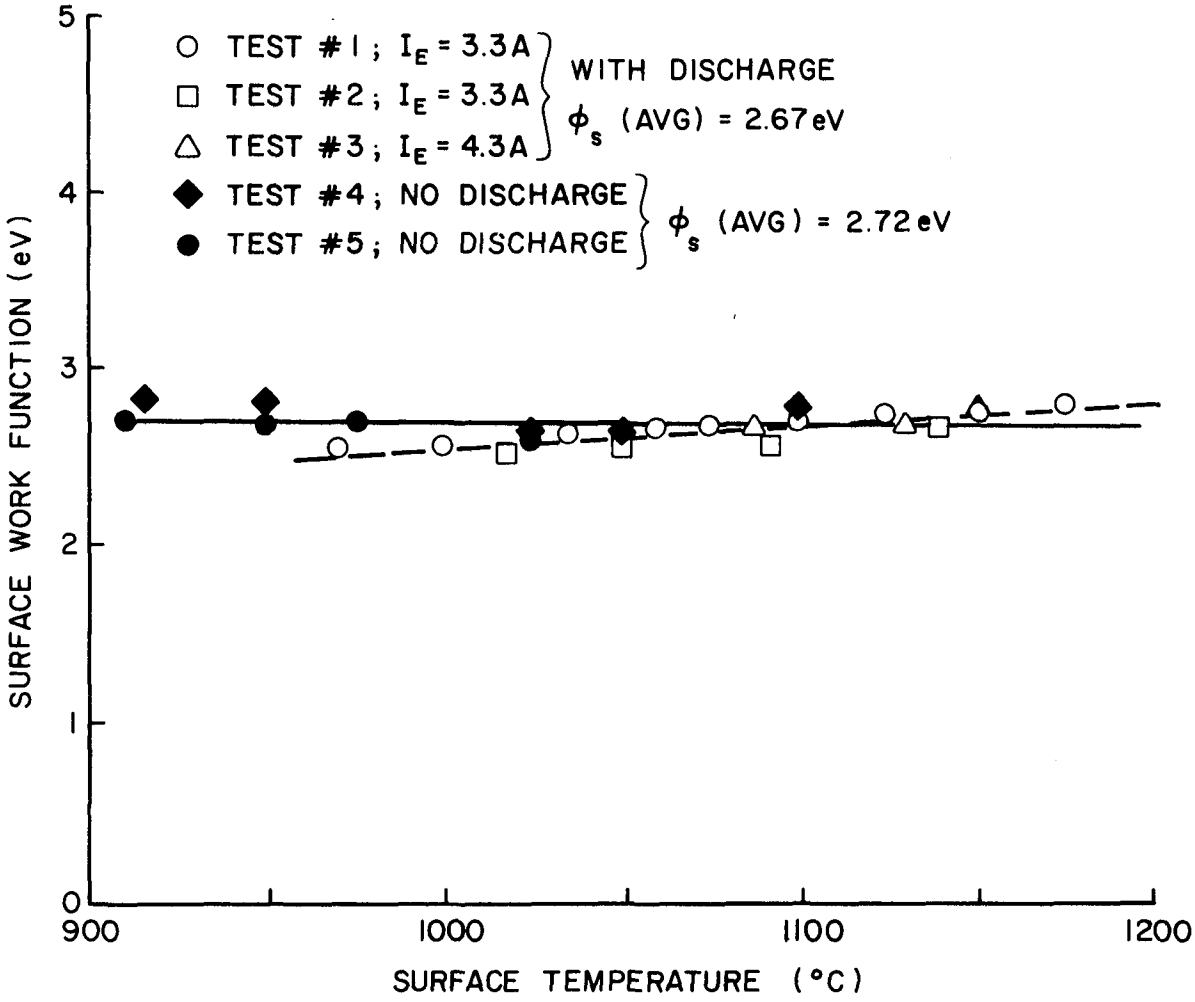

Figure 27. Comparison of Surface Work Function with and without Discharge Present.

of an individual test as well as from one test to the next. It was observed for example that the electron emission current at the higher temperatures decreased during the time it took to make a temperature measurement. (See Figure B1, Appendix B.) This change became increasingly significant as the negative bias, and therefore, the patch temperature were increased. This decrease in emission current with time suggests an increase in work function probably due to increased sputtering and evaporation of barium caused by higher ion bombardment energies at the higher negative bias. In the extreme cases, the barium was apparently depleted to the point where no electron emission would take place from the patch even if the patch were biased to -35 v. This situation is discussed in Appendix B. It was found, when the patch would not emit, that heating the entire cathode to $\sim$ 1250°C using the external heater caused the patch surface to be reactivated. This heating presumably forced a redistribution of barium from other, normally cooler, surfaces within the cathode. After such a heating cycle the experiment could be continued although the surface work function would be somewhat different than that in the previous test. Such a reactivation procedure was performed between Test #1 (open circles) and Test #2 (open squares). A similar redistribution of barium apparently took place during Test #4 when the cathode was heated to 1100°C by the end of the test. This is considered responsible for lowering the surface work function from Test #4 to Test #5. The point of this discussion is that the magnitude of the surface work function results of Figure 27 varies significantly from one test to the next and that this variation, due to actual surface condition changes occurring between tests, is as great as the variation between the discharge case (open symbols) and the no discharge case (solid symbols).

The dashed line in Figure 27 shows the least squares fit for the results indicated by the open symbols (i.e., with the cathode operating). These data show the expected linear increase of the surface work function with temperature. The fact that the no-discharge case (solid symbols) does not show a clear linear temperature dependence is surprising and may be due to the redistribution of barium which occurs when the entire cathode is heated. The decrease in work function of the patch as the cathode is heated (Tests #4 and #5) may be overshadowing the linear increase normally seen when dealing with the "true" work function. In fact, for both the discharge case and the no-discharge case it should be understood that the surface conditions and therefore the work function at any given temperature or discharge condition, must be viewed as a condition of dynamic equilibrium for the low work function compounds present on the surface. The surface density of these compounds, determined by this equilibrium condition, is dependent on the rate at which they are lost from the surface by sputtering and evaporation and the rate at which they are deposited by condensation and by positive low work function ions (in the discharge case), which are attracted to the cathode potential surfaces. This equilibrium state is certainly dependent on cathode operating conditions and history.

The purpose of the experiment embodied by Figure 27 was to compare the surface work function of the test patch calculated using the hollow cathode emission model with an independently determined value measured when no discharge was present. Agreement between the two values of the work function is considered to be evidence supporting the model of field-enhanced, thermionic emission as the dominant emission mechanism for the hollow cathode. It is felt that the results shown in Figure 27 are in reasonable agreement considering the experimental variation in work function discussed above, and they are therefore considered to support the validity of the model.

It is interesting to note that the numerical average of the values of the work function calculated from the model (open symbols, Figure 27) is 2.67 eV compared to an average value of 2.72 eV determined for the case where no discharge is present (solid symbols). This agreement is considered remarkably good, particularly when it is considered that the difference of 0.05 eV between these two average values is considerably less than the scatter of the data due to the experimental variation of the work function discussed above. Though this close agreement may be partially fortuitous, it is believed to be significant in light of the variation in surface conditions during the tests.

It should be mentioned that the work function of 2.7 eV applies to the test patch which is probably somewhat depleted and therefore not representative of large tantalum insert surfaces which are coated with R-500. This value of 2.7 eV is typical of barium tantalate compounds[18] which are probably present on the surface even after the oxide coating is depleted. It is considered likely that under normal operating conditions most of the emission in the cathode takes place from regions of the insert where the work function is on the order of 2.0 eV. This average surface work function is typical of the larger surfaces discussed previously and probably reflects the presence of barium oxide coating.

ENERGY BALANCE AT THE EMISSION SURFACE

In general, the ion and electron components of the measured current to an emission surface are not known and can not be directly measured. However, the ratio of these components of the measured current can be estimated from the energy balance at the emission surface and this is the procedure used in the model described in Reference 17. The surface work function experiment conducted on the patch provides a unique means of investigating the validity

of using such an energy balance to determine the ratio of ion to electron currents at the emission surface. This can be done because one has the capability of determining the ion and electron components of the current to the test patch directly. When the patch was not biased, and therefore not emitting, all of the measured current was due to ion flux to the patch. When the patch was biased negative of cathode potential, the increase in measured current was due to the electron emission from the patch. In this case, the ion and electron components of the current can be obtained directly from the current-voltage characteristic for the patch and are the currents labeled $I_p(i)$ and $I_p(e)$ respectively in Figure B1 of Appendix B. Knowing the currents $I_p(i)$ and $I_p(e)$ and the patch surface area, the net power input to the patch ($\dot{q}$) due to the flux of the charge carriers can be calculated using

$$\dot{q} = [I_p(i) \cdot (V_p + V_i - \phi_s)] - [I_p(e) \cdot \phi_e] \qquad (14)$$

where the first bracketed term is the ion heating power and the second is the power required to boil off electrons. Here V_p is the plasma potential and V_i is the ionization potential. It is noted that the power input to the patch from excited neutrals is neglected in this equation because their contribution is believed to be small. The open symbols in Figure 28 show the $\dot{q}$ calculated, using Eq. (14) along with currents, voltages, and work functions determined from the patch experiments, and plotted as a function of patch temperature. The solid line shown in Fig. 28 is the least squares fit of the open symbols.

If the assumptions regarding the energy balance are correct, then $\dot{q}$ from Eq. 14 should be equal to the total thermal power lost from the surface by radiation, conduction and convection. For the quartz test cathode with a thin foil insert, it was proposed that the predominant

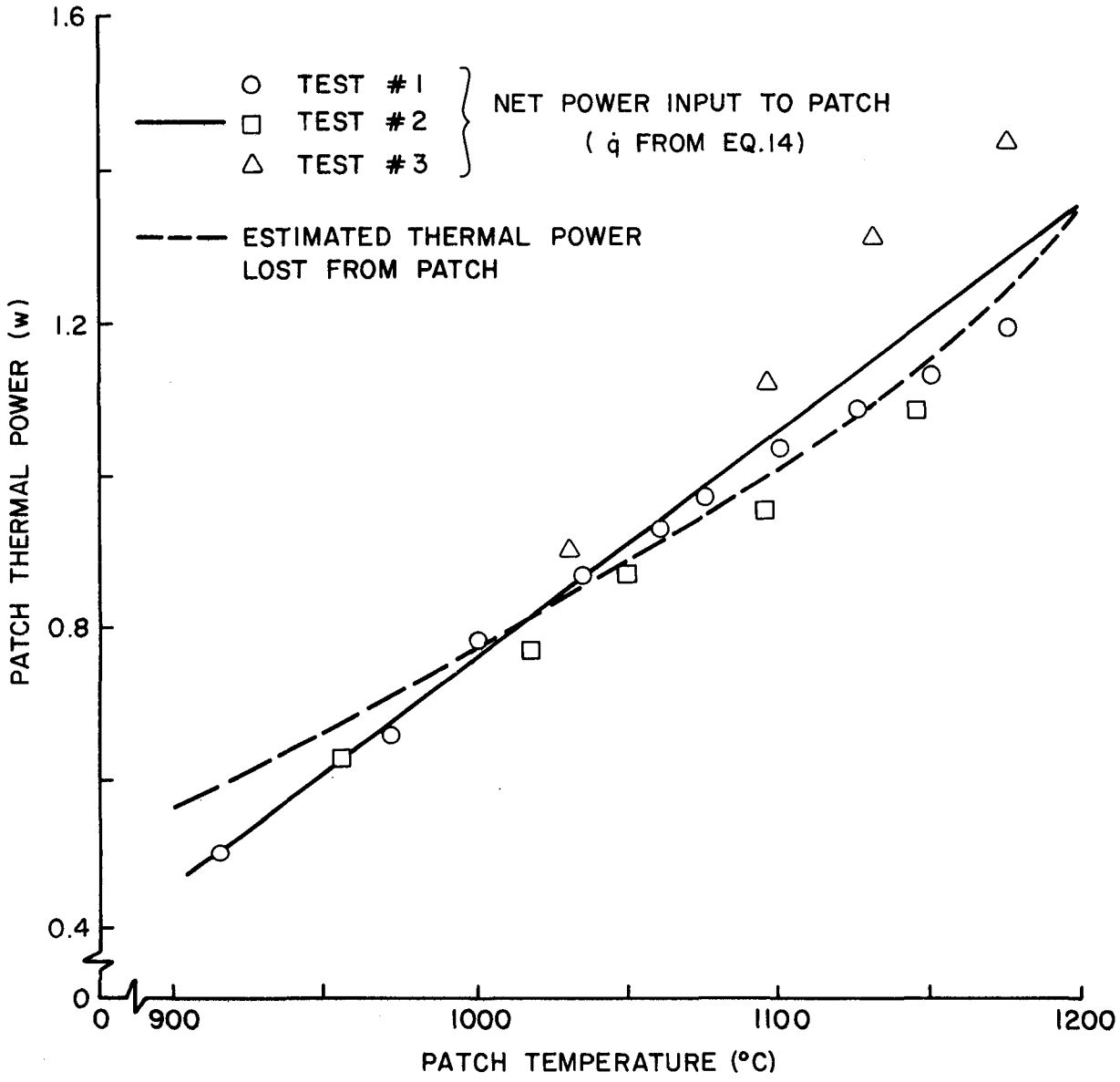

Figure 28. Comparison of Patch Insert Power with Computed Power Thermal Loss.

thermal loss would be by radiation from the outer surface of the insert and could be estimated by an expression such as $\dot{q} \approx A\varepsilon\sigma T^4$ where A is the surface area of the patch, ε is the surface emissivity ($\sim$ 0.5 for tantalum), σ is the Stefan-Boltzmann constant, and T is the surface temperature. In the case of the test patch, this expression underestimated the thermal power loss by a factor of 2 to 2.5. This was probably due to the effect of additional thermal losses by conduction and radiation from the three, 0.25 mm diameter leads attached to the back of the patch. The effect of these leads was accounted for by modeling the patch as a flat radiating surface at temperature T with three cylindrical fins extending 4 mm from the patch. The fins were modeled using a simple four node finite difference analysis accounting for both conduction along the leads and radiation from their surfaces to presumed cold external surfaces (note that during the test the heater shown in Figure 26 is moved out of the way and the patch does radiate to cold external surfaces). The results of this analysis are plotted as the dashed curve in Figure 28. Admittedly the analysis is rather crude and the results are somewhat dependent both on the fin length that is chosen and on the temperature that is chosen for the surface to which the patch radiates. However, the results are not very sensitive to fin length and the assumption regarding the temperature of the surfaces receiving the radiation is believed to be a good one. The agreement between the curves in Figure 28 is good. Even considering the above disclaimers, it is felt that the thermal power estimated for the patch is quite reasonable and supports the use of the energy balance as a valid means of determining the ratio of the ion to electron currents at the emission surface.

It should be stressed that the value used for the thermal loss ($\dot{q}$) is specific to the thermal configuration of the insert and cathode. Just as

the patch was not suitably modeled using the expression $\dot{q} \simeq A\varepsilon\sigma T^4$ chosen for the insert in the quartz tube cathode, a metal body cathode with a multilayer foil or solid type insert would require specific analysis related to its thermal characteristics.

CONCLUSIONS

This experiment showed that based on the proposed model the surface work function calculated for a test patch in an operating cathode was in good agreement which the surface work function determined for the same surface by a conventional surface work function test. This supports the basic assumption of the model that field-enhanced thermionic emission is the dominant surface emission mechanism for this type of cathode.

The energy balance on the emission surface as used in the model described in Reference 17 is shown to provide a valid method for determining the ratio of ion current to electron emission current. Application of this method requires a reasonable characterization of the heat transfer from the emission surface for the particular insert/cathode design being investigated.

PLASMA PROBING IN ORIFICED, HOLLOW CATHODES

Dan Siegfried

The orificed, hollow cathode model referred to in the preceding section of this report is shown to describe with reasonable accuracy the electron production processes taking place inside the cathode. However, in its present form the model does not contain sufficient detail to make a priori predictions of plasma properties or their spatial variation. Because of this deficiency it cannot be used to predict the location at which the surface emission will take place or such overall operating characteristics of the cathode as discharge voltage or discharge mode. It is desirable that the model be extended to include these capabilities, and it is for this reason that an additional experimental study was undertaken to make detailed plasma properties measurements inside of the cathode. The experimental portion of this study was completed this year and included the simultaneous measurement of plasma property profiles, insert temperature profiles, emission current density profiles and internal cathode pressure over a range of emission currents, mass flow rates, and orifice diameters. The large amount of data collected from this experiment is still being analyzed with the goal of extending the present model to include the considerations mentioned above. It is planned that the results of this study will be published in the form of a contractor report in the coming year and so will not be presented here. The probing technique and method of analysis used for determining plasma properties in this study are presented as Appendix C of this report.

CONTROLLING ION CURRENTS TO DISCHARGE CHAMBER SURFACES

Given the choice an electrostatic ion accelerator designer would probably opt for a design in which every ion produced in the discharge chamber would be directed through the screen grid where it could contribute to the extracted beam. If such a condition could be realized it would result in maximum thruster propellant and energy efficiencies and minimum sputter erosion rates of discharge chamber surfaces. The generally accepted theory describing discharge chamber operation has however suggested that this ideal design is not approachable. This theory is based on the premise that ions once they are produced in the primary electron region of the discharge chamber they leave it isotropically.[20,21] This suggests that the fraction of the ions produced that find their way through the screen grid is equal to the ratio of screen grid open area to the total surface area bounding the primary electron region. Recent experiments have however suggested that the commonly held theory is invalid and that the design giving ideal performance can be approached. These experiments and their interpretation is the focus of this chapter.

DIVERGENT FIELD THRUSTER STUDIES

The basic elements of a divergent field discharge chamber are shown in Figure 29a. The primary and high temperature Maxwellian electrons that do most of the ionizing are generally confined to the primary electron region shown. It is also generally assumed that ions produced in this region move with equal probability in any direction, and this assumption has led to models that have been used to predict discharge chamber performance successfully.[21] Such a model suggests that the ion current densities to all surfaces bounding this region should be about equal, i.e., to the

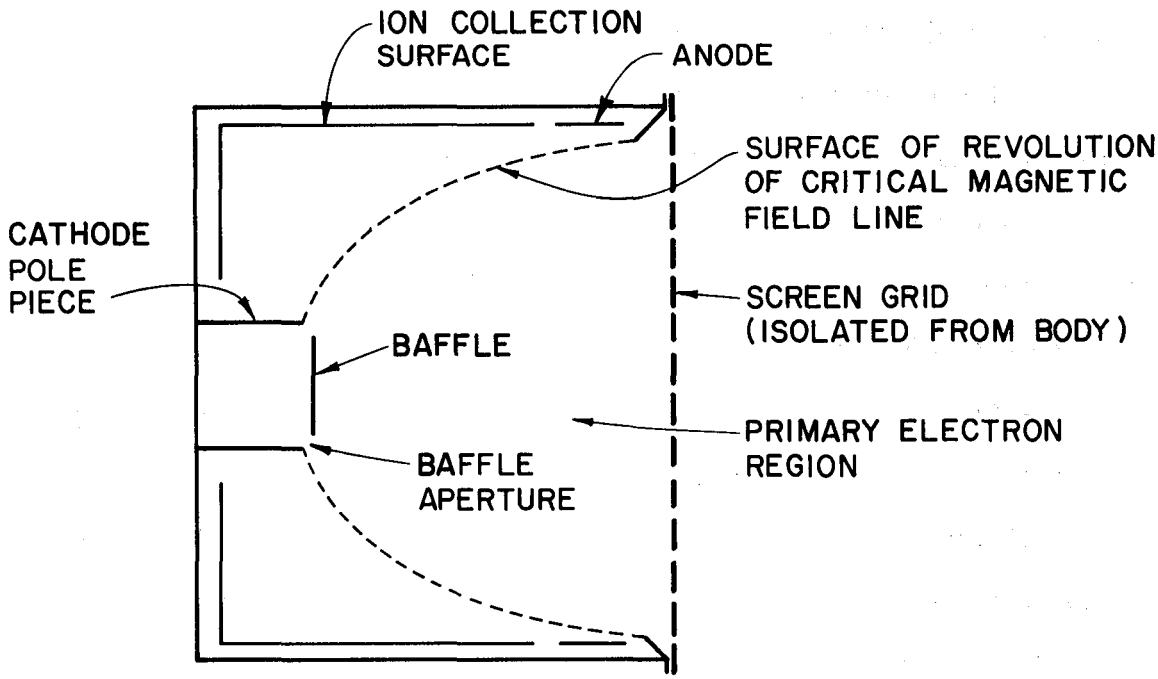

a. DIVERGENT FIELD DISCHARGE CHAMBER SCHEMATIC

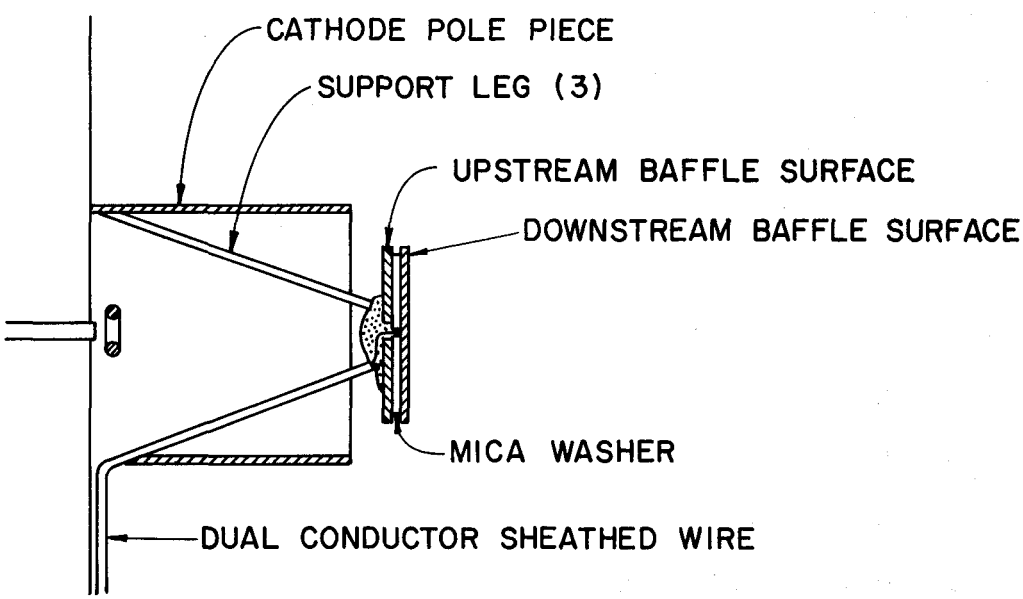

b. DOUBLE SURFACE BAFFLE DESIGN FOR SERT II THRUSTER

Figure 29. Divergent Field Thruster Test Apparatus.

surface of revolution of the critical field line, the baffle, the baffle aperture, the screen grid webbing and the screen grid open area. In order to check whether this postulate was true the conventional baffle of a SERT II, divergent field thruster was replaced with the double surface baffle shown schematically in Figure 29b. The two surfaces of this baffle made from closely spaced 0.25 mm thick stainless steel sheets can be biased independently through the wires shown while the thruster is operating. When this is done, they behave like large Langmuir probes and if they are biased substantially negative of discharge chamber plasma potential the ion current incident on them at their normal operating potential can be measured. The screen grid shown in Figure 29a was also isolated from the thruster body and wired so it could be biased in the same way. Finally, in a separate experiment, the ion collection surface shown was added and it too was designed so it could be biased to measure the ion current crossing the critical field surface. Using this apparatus then it was possible to measure the ion currents to both baffle surfaces, through the critical field surface and to the screen grid webbing. The beam current extracted through the screen grid holes is of course also measured. When these currents are divided by their associated surface area a mean current density to that surface is determined. In this regard it should be noted that the mean ion current densities to the baffle surfaces is probably not the same as the current density to any particular point on those baffle surfaces. In this same vein it is known that the mean and local values of ion current density are markedly different for the screen grid and the beam current. The beam current density profile is relatively peaked because of the correspondingly peaked ion density profile in the SERT II discharge chamber. The ion current density to the screen grid varies with radius not only

because of this radial ion density variation but also because of the annular ring beyond the edges of the outermost holes which collects discharge chamber ions. Because of this ring the screen grid sees not only a non-uniform plasma but it has a surface with non-uniform ion collecting characteristics. In spite of these conditions one can gain some very useful information by considering the mean ion current densities involved.

The SERT II thruster was operated over a wide range of flow rates and discharge power conditions and ion currents of interest were measured. Mean ion current densities determined from these runs are shown in Figure 30. One observes that the mean ion current densities to baffle, screen grid and beam correlate well over this wide range of flow rates and discharge powers as evidenced by the relatively close proximity of the data points to the lines passing through them. Secondly, the mean ion current density to the baffle is seen to be about twice that to the beam and about three times that to the screen grid. Figure 31, which shows the mean ion current density toward the screen grid plotted against the mean ion current density to the downstream baffle surface, is based on data taken from the solid lines in Figure 30. The mean total current density toward the screen grid as used here is the sum of the beam and screen currents divided by the total area of the screen grid (open and closed). The high degree of linear correlation between this total current density and the baffle current density is noteworthy, but the important point demonstrated by Figures 30 and 31 is that under all conditions investigated the ion current density toward the baffle is about 2½ times that toward the screen grid. This seems to contradict the model of isotropic ion loss from the primary electron region.

There is additional piece of information that should be considered before the isotropic model of ion current distribution is rejected. It

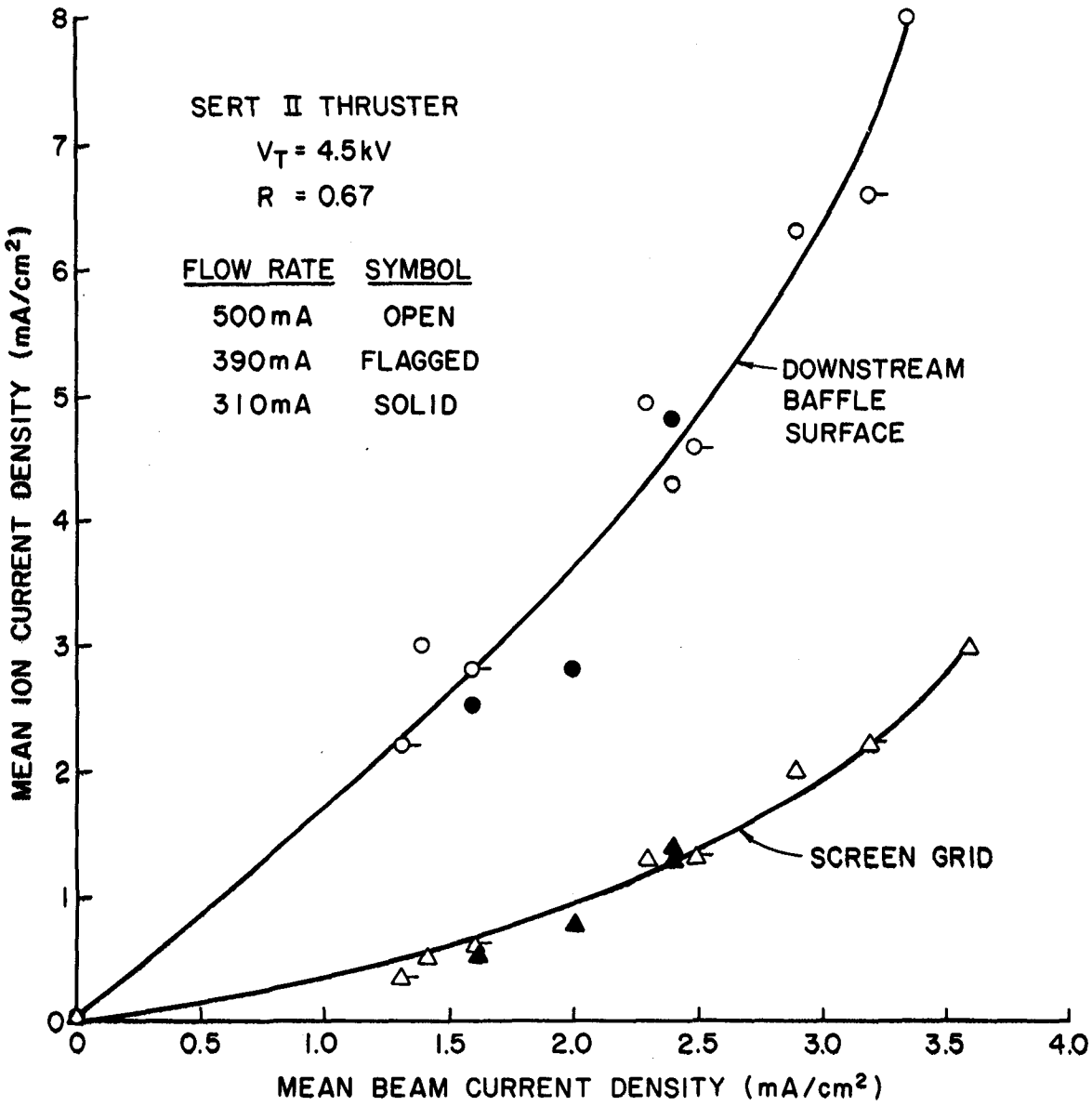

Figure 30. Ion Current Density Distribution.

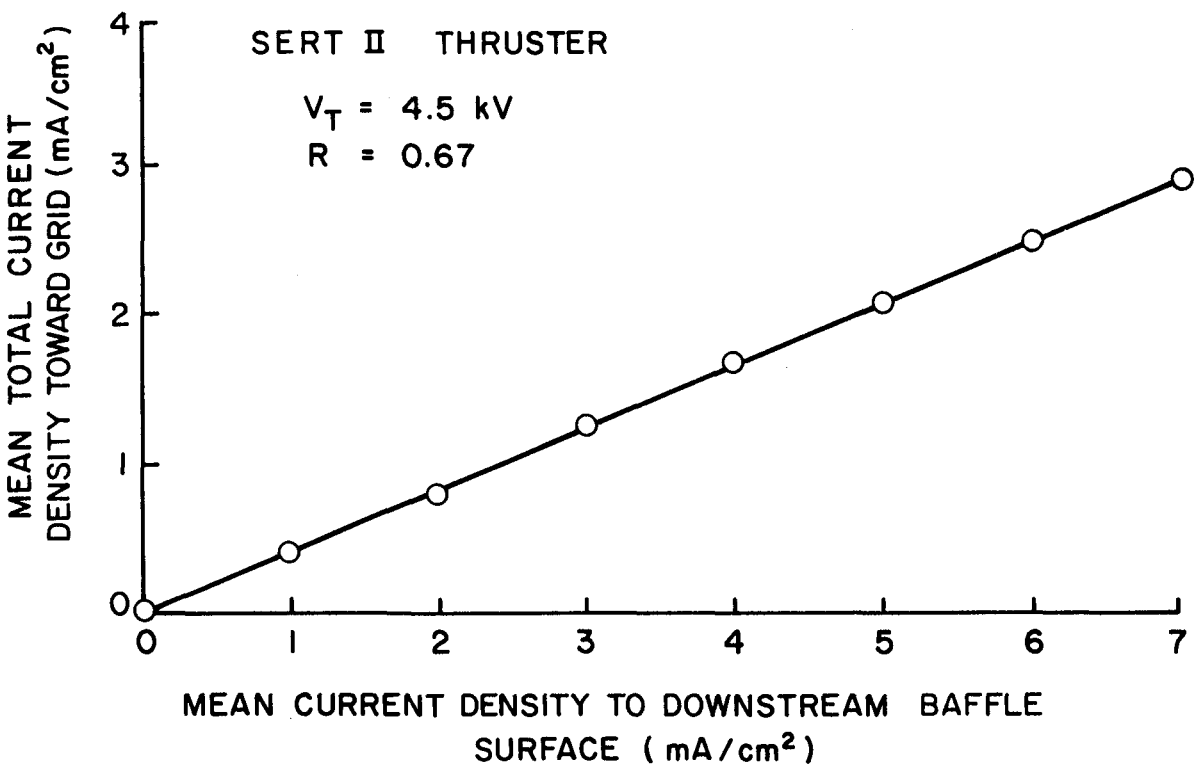

Figure 31. Ion Current Density Correlation.

concerns ion motion toward the critical field line boundary shown in Figure 29a. There is no electrode to collect ions at this boundary, and because the gyro radius for ions is large, one might expect that they would pass right through this surface to anode and cathode potential surfaces located beyond it. Current measurements were made in the SERT II thruster both with Langmuir probes and with the ion collection surface positioned outside of the critical field line (Fig. 29a) and biased to collect ions. These measurements showed that the ion current density across the surface of revolution of the critical field line is about 15% of the beam current density over a range of flow rate and discharge power conditions.

In summary these tests have shown that the ion current density to the upstream baffle surface is $\sim 2\frac{1}{2}$ times that toward the screen grid while the ion current density crossing the surface of revolution of the critical field line is only $\sim$ 15% of that toward the screen grid. These results suggest that while ions probably leave the discharge chamber ion production region isotropically those reaching the surface of revolution of the critical field line are focused by local electric fields along this surface. As a result of this focusing ions are directed toward the baffle region and hence a higher current density is observed there. It is postulated that the required local electric fields at the critical field surface develop as a result of the magnetic confinement of the electrons near this surface. The potential differences at this surface would have to be relatively small (a volt or less) because they are not obvious from Langmuir probe measurements made in discharge chambers. Ion energies at the surface should be in the atom temperature to Bohm energy range ($\sim$0.05 to $\sim$5eV) so potential differences of the order of a volt should be sufficient to deflect many of them.

While ion current densities through the baffle aperture and to the cathode and anode pole pieces were not measured in this study it is considered likely that high ion current densities do exist at these locations. Additional evidence of high currents to the cathode pole piece and through the baffle aperture is found in life test results for the 5 and 30 cm diameter thrusters which revealed anamolously high erosion rates on both surfaces of the baffle and the cathode pole piece.[22,23] It is considered probably that these high erosion rates were a consequence of bombardment by doubly and singly charged ions which had been diverted along the critical field surface and came from the main discharge plasma. Incidentally it is considered likely that excessive erosion evident on the inside of the cathode pole piece in these life tests was caused by ions that came from the main discharge through the baffle aperture. Such ions would be able to acquire sufficient kinetic energy to give the relatively high sputtering yields required while ions from the cathode discharge region would not. In this regard it should be mentioned that test results obtained on the double surface baffle (Fig. 29b) showed the ion current density to the upstream surface of the baffle is about equal to the ion current density to the screen grid. It was not possible however with the apparatus used here to determine through energy discrimination whether these ions were coming from the main or cathode discharge regions.

An additional piece of information concerning ion focusing can be obtained from the data of Figure 30. It concerns the focusing of ions that takes place at the screen grid. Aston reported that equipotential profiles measured upstream of the screen grid appeared to focus ions away from the screen grid webbing and through the apertures.[24] The present work supports his observation. Using data points taken from the solid line for screen

grid current on Figure 30 one can determine the fraction of ions approaching the screen grid that actually pass through the grid. This fraction represents the effective open area of the screen grid for ion extraction. The upper curve of Figure 32 shows that this fraction varies in the 60% to 80% range as ion flux toward the screen grid is varied by adjusting discharge power and propellant flow rate conditions. The fact that the transparency of the screen grids to ions is greater than the physical open area fractions for the grid suggests substantial local ion focusing toward the apertures. The two open area fractions identified on Figure 32 differ because the open area fraction pertaining to the entire grid accounts for the annular ring beyond the outermost holes that can collect ions and the other one is the open area fraction over the central region of the grid.

The dotted curve in Figure 32 shows how this fraction changed when the high voltage was turned off. The data associated with this curve were obtained by measuring the ion currents to the downstream baffle surface, screen grid and into the beam with the high voltage on. The high voltage was then switched off and the ion currents to the downstream baffle surface and screen grid were measured again. This procedure was repeated over a range of flow rates and discharge power levels and a correlation between these currents was established (similar to Fig. 30). It was then argued that the ion currents toward the screen grid and the downstream baffle surface should be independent of the total accelerating voltage level. On the basis of this argument it was possible to compute the ion current through the grids with the high voltage off as the difference between the ion current toward the screen grid and the ion current collected at the screen grid at a specified baffle current level. The ratio of this ion current through the grid to the ion current toward the grids is equal to the effective screen grid open area fraction.

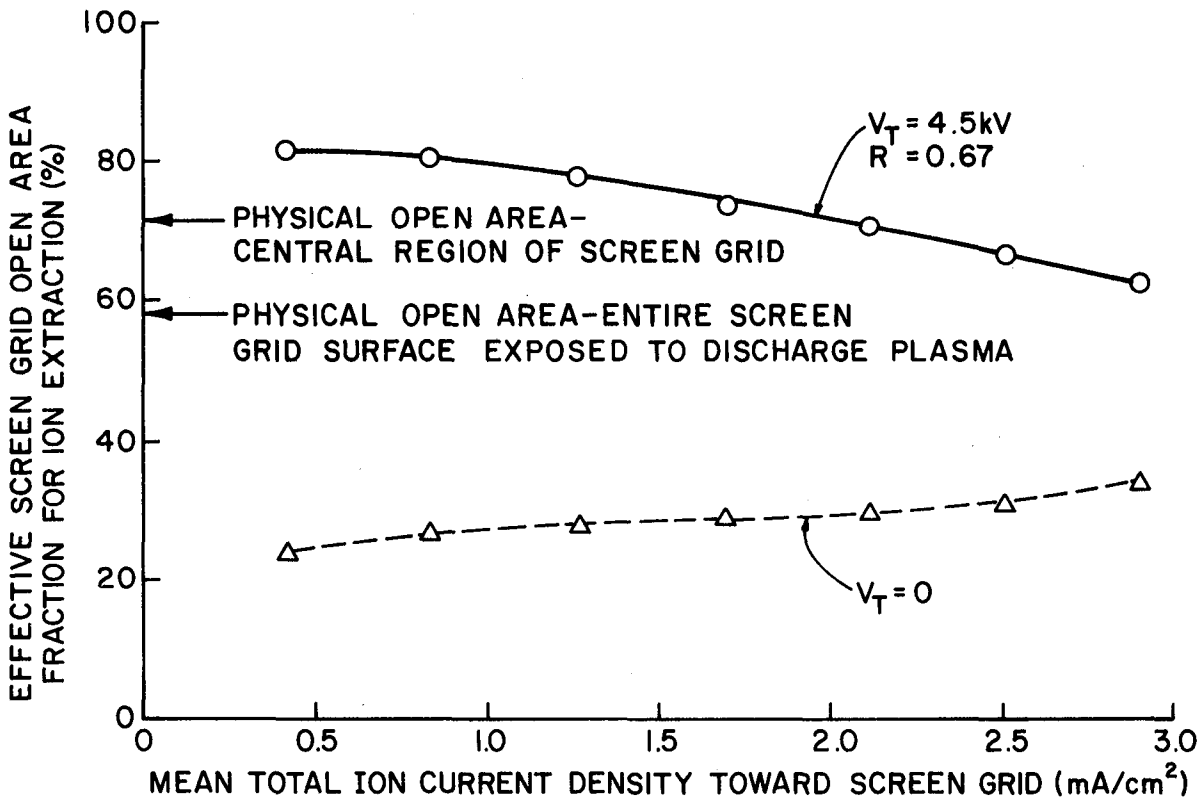

Figure 32. Ion Focusing at the Screen Grid.

Figure 32 suggests that the ion focusing at the screen grid is altered when the high voltage is turned off such that the apparent transparency of the grids to ions is reduced to about 25% to 35%. This implies that turning off the high voltage causes a greater fraction of the ions directed toward the screen grid to be focused onto the webbing rather than through the holes.

FLEXIBLE MAGNETIC FIELD THRUSTER STUDIES

Once one accepts the hypothesis that ion currents can be controlled in a discharge chamber by controlling electrons with magnetic fields he is led logically to the conclusion that it might be possible to direct essentially all ions produced in a discharge chamber toward the ion extraction grids. In order to investigate this possibility it is desirable to have considerable freedom in manipulating the discharge chamber magnetic field. This freedom is available with the flexible magnetic field thruster described in the next section of this report. In the discharge chamber of this thruster the anode is simply a tube that carries a current of several tens of amperes. This current induces the protective magnetic field around the tubular anode. The tube can be bent in essentially any shape to generate the desired magnetic field shape. This thruster was also designed so the entire thruster body and screen grid could be biased like a Langmuir probe and the ion current to these surfaces could be measured. Because the anode and refractory wire cathode surface areas were less than 10% and 1% respectively of the thruster body area it could be assumed that essentially all ions produced in the thruster were collected on the body or screen grid or else extracted in the ion beam. This assumption was also aided by the expectation that the anode would be positive of discharge plasma potential, a condition that should reduce the ion collection rate at the anode. This

expectation was in turn justified on the basis that the anode area was sufficiently large so the random electron current to it generally exceeded the current demanded by the discharge power supply.

A number of magnetic field shapes were generated by bending the anode into different configurations in the course of these tests. Figure 33 contains sketches of three of these configurations along with magnetic field line drawings showing the magnetic field shapes associated with each of them. Each sketch includes arrows showing the direction of the magnetic field current flowing through the anode. The data plotted shows how the magnitude of this current affects the fraction of ions produced in the discharge chamber that end up being extracted in the ion beam. This fraction, which is the ratio of beam ion current to beam plus body plus screen grid ion currents, is a good indicator of the efficiency of the discharge chamber design in directing ions through the grids. The solid curve (circular data points) in Fig. 33 shows the field current does not affect the fraction of the ions produced in the chamber that end up going to the beam for the countercurrent coil anode configuration. Recall it is postulated that increased magnetic field currents can improve electron containment and that this in turn induces electric fields that stop ion migration past the magnetic field to the thruster body. In the case of the countercurrent coil configuration however, the ions are ineffectively redirected and they simply find their way to the body at a different location than the one they would reach were the magnetic fields not present. Hence the extracted ion fraction is independent of field magnet current. It is noteworthy the ratio of screen grid open area to primary electron region surface area for this thruster is about 18%, and this is about equal to the extracted ion fraction shown in Figure 33 for the countercurrent coil design.

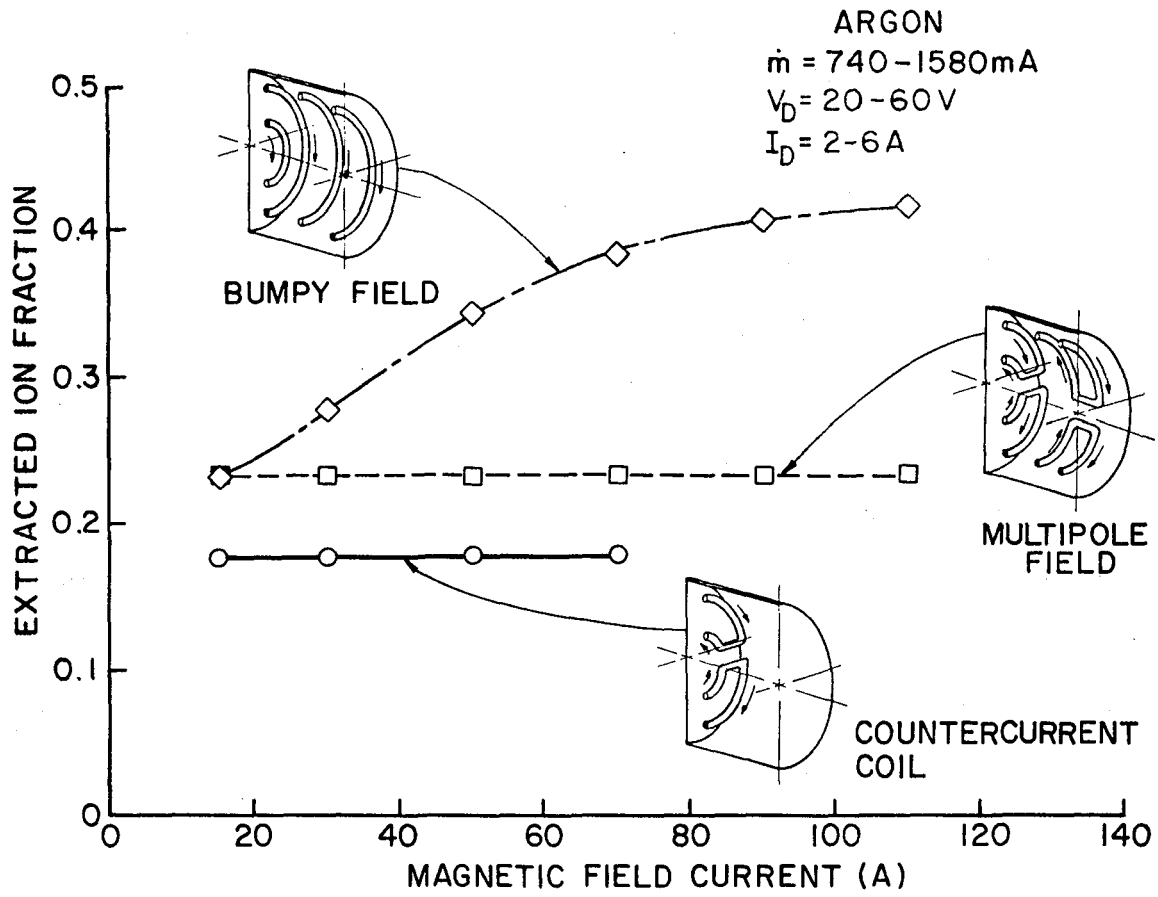

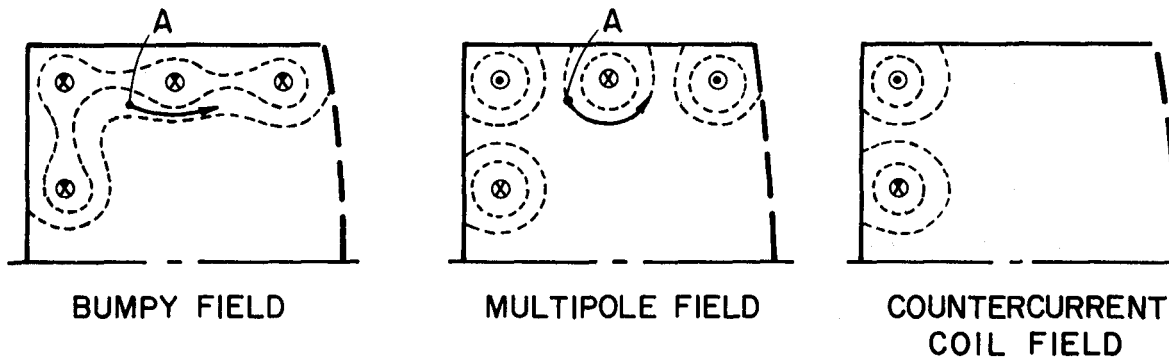

Figure 33. Effect of Magnetic Field Configuration on Ion Extraction Capability.

When additional anode surface area is added as with multipole field configuration (dotted line with square data points) the extracted ion fraction is again independent of magnetic field current. This ratio is, however, seen to be higher ($\sim$ 23%) for this configuration than it was for the previous one even though the screen grid open area to primary electron region surface area is still $\sim$ 18%. This suggests that increasing the anode surface coverage of the chamber tends to increase the fraction of ions directed toward the screen grid slightly even though the magnetic field is not effective in aiding this process.

The bumpy field configuration (centerline with diamond symbols) shows a very important effect in Figure 33. Contrary to the two preceding cases, increases in the field current cause redirection of ions toward the grid for this configuration. In fact at high field currents the fraction of the ions produced that are extracted reaches over 40% even though the screen grid open area to primary electron region surface area ratio remains at $\sim$18%. This is particularly significant because it indicates that through proper magnetic field design it may be possible to direct essentially all ions produced in the discharge chamber toward the screen grid.

Some insight into the mechanisms acting that make the bumpy field configuration more effective at controlling ion migration than the multipole configuration can be gained by comparing the magnetic field line-of-force drawings associated with each anode shape. For the bumpy field case consider a primary electron being reflected from the anode by the magnetic field. If this electron has a collision at point A in Figure 33 for example it would tend to be captured and directed along the path shown. Because of the field shape it tends to remain on the discharge side of the anode. Because the electron cannot get across this magnetic field boundary the

electron density is low in the region between the anodes and the chamber walls and the ion loss to the walls is therefore small. For the case of the multipole anode configuration however a similar collision causes the electron to be directed toward the discharge chamber wall in the manner shown in Fig. 33. Because electrons are not confined one would also expect the ions to get to the walls where they could be lost through recombination .

APPLICATION TO EXISTING THRUSTER DESIGNS

It is interesting to reflect upon ion flow patterns in existing discharge chamber designs as predicted by the theory that has just been presented. Figure 34 shows some of these discharge chamber magnetic field configurations. The divergent field configuration of Figure 34a has already been discussed. In it ions would be expected to be diverted along critical field surfaces so that above average ion currents would be expected going to the baffle, cathode pole piece and probably the anode pole piece. High ion currents would also be expected through the baffle aperture and these would be expected to strike the interior structure of the cathode discharge region.

In the multipole configuration the critical magnetic field surface has a shape like the one shown in Figure 34b.[25,26] With this configuration electrons and therefore the ions that couple to the electrons should be diverted along the field surface into the ends of the pole pieces. Higher sputter erosion might therefore be expected on the tips of the pole pieces. If the magnetic flux density for the multipole were increased substantially then the bulk of the electrons approaching the pole piece could find themselves in a sufficiently strong magnetic mirror effect so they would be reflected from the pole pieces (Fig. 34c). Keeping the electrons sufficiently far

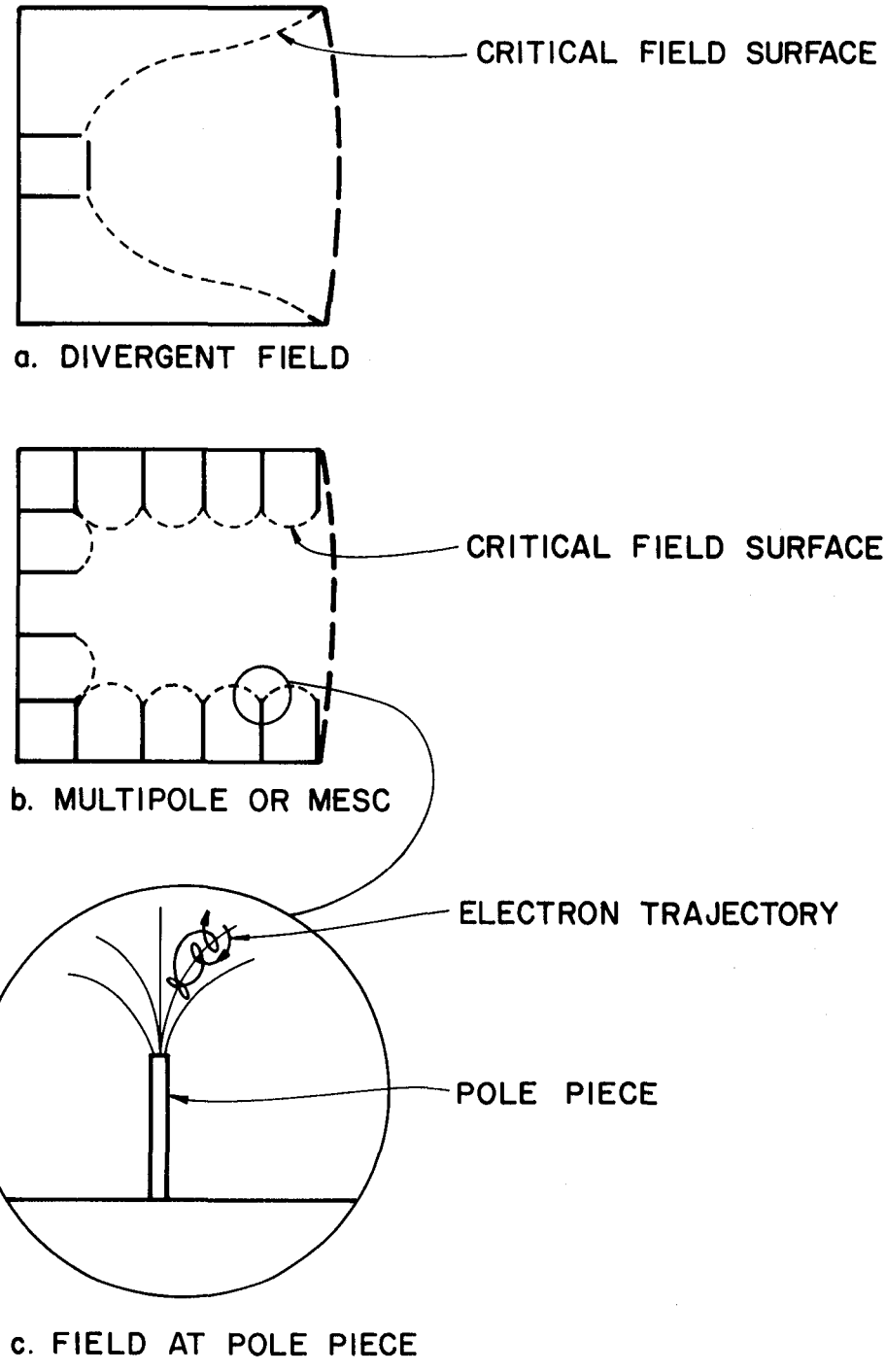

Figure 34. Conventional Magnetic Field Configurations.

from the pole pieces should again set up an electric field that would present ion migration to the pole piece tips. Such an effect is consistent with the improved performance observed in the Magneto-Electrostatic Containment (MESC) thruster where high magnetic flux densities exist at the pole piece tips.[27] It is believed that the good performance achieved by Sovey in his line-cusp thruster was also attributable to this same magnetic mirror effect at the pole pieces.[28]

CONCLUSION

Ion currents flowing in discharge chambers can be controlled through proper selection of magnetic field shapes and magnitudes. With one field shape tested as many as 40% of the ions produced in the discharge chamber were extracted in the beam and higher fractions are considered achievable. It is postulated that the mechanism whereby this is accomplished is related to the confinement of electrons away from such cathode potential surfaces as chamber walls and pole pieces. By confining electrons and preventing their migration to cathode potential surfaces it is argued that local electrical fields are set up that stop ion migration to and recombination at these surfaces. This model can be used to explain sputter erosion patterns and performance variations observed in currently available thrusters.

THE FLEXIBLE MAGNETIC FIELD THRUSTER

The concept of this ion thruster discharge chamber design was conceived initially as a research tool that could be used to investigate discharge chamber phenomena. The basic characteristic of the device that makes it desirable for research is its capacity to undergo rapid modifications to its magnetic field shape and strength. As the research into the concept has progressed however the results obtained have suggested that it may exhibit superior performance as a thruster for space missions as well.

The basic idea behind the device involves generating a magnetic field that completely envelopes a long tubular anode. This magnetic field is circumferential to the anode and is generated by passing relatively large direct currents through the anode. The anode tubing can be routed through the discharge chamber in any way desired to produce the overall magnetic field shape of interest and regardless of how the anode was routed it is generally shielded from primary electrons over its full length. The entire thruster shell is maintained near cathode potential during operation so electron migration to this surface is limited by the electro-static fields between the shell and the plasma. It was anticipated that with this design primary electrons emitted by the cathode would bounce around inside the discharge chamber being reflected by the magnetic fields at the anode and the electric fields at the near cathode potential body. Eventually they would undergo an ionizing collision, thereby losing sufficient energy to facilitate their migration across the magnetic field to the anode surface.

ANODE DESIGN CONSIDERATIONS

The practicality of the flexible field thruster depends to a large extent on the anode currents required to develop the required circumferential

magnetic field around it. This current must be sufficient to produce fields that will prevent the monoenergetic primary electrons in the discharge plasma from reaching the anode surface. The magnetic flux density (B) at a radius (r) from the centerline of a wire carrying a current (I_f) is given

$$B = \frac{\mu_o I_f}{2\pi r} \tag{15}$$

where μ_o is the permeability of free space and it has been assumed that "r" is greater than the wire radius (r_o). In order to prevent collection of electrons having an energy E_e (in eV) Isaacson found the following condition on the integral of the magnetic flux density had to be satisfied in a similar geometrical situation[26]

$$\int_{r_0}^{r_1} B dr \geq 6.74 \times 10^{-6} \sqrt{E_e} \quad . \tag{16}$$

In this expression r_1 is either the radius at which the magnetic flux density drops to a negligible value or the radius at which electrons are injected into the magnetic field, whichever is less. Combining Eqs. 15 and 16 and performing the indicated integration one can solve for the current required through the wire. After substituting for the permeability one obtains

$$I_f = \frac{33.7 \sqrt{E_e}}{\ell n\left(\frac{r_1}{r_0}\right)} \quad . \tag{17}$$

For 40 eV primary electrons, a 1.6 mm radius wire and a radius of electron injection in the radius range of 1 to 2 cm the required magnetic field current given by Eq. 17 is about 100 A. This is large, but not unacceptably so. For a 1.6 mm radius anode of the order of a meter in length further analysis suggests that copper can carry the required current with a small voltage drop over the one meter tube length ($\sim$ 0.1 v) as long as the wire

is maintained at a sufficiently low temperature ($\sim$ 80°C). Computations suggest this temperature can be maintained by using commercially available 3.2 mm dia. copper tube and circulating water through it at a flow rate of a few tens of ml/min.

APPARATUS AND PROCEDURE

In order to investigate the flexible magnetic field thruster experimentally a cylindrical chamber was designed into which the various anode configurations of interest could be inserted. The basic stainless steel, sheet metal chamber, shown schematically without an anode in Figure 35h, is 16 cm in diameter and 8 cm long. The other sketches in Figure 35 show perspective cutaway views of anode configurations examined in this preliminary series of tests. For all tests that involved more than one anode loop, the spacing between adjacent loops was $\sim$ 2.5 cm. The refractory wire cathode used in the tests was positioned 2.5 cm upstream of the grids in the manner suggested in Fig. 35h for all anode configurations shown except the single downstream torus (Fig. 35a). In this case the cathode was 5.5 cm upstream of the grids. The refractory wire cathode employed 0.25 mm dia. tungsten wire about 30 cm in length. This cathode was heated using alternating currents in the range 12 to 15 A from a center-tapped power supply. Argon propellant was used because of the ease with which flow rates could be set and maintained. Tests were conducted at flow rates of 740, 1270 and 1580 mA equivalent. Thruster performance was measured at discharge voltages through the range of 20 v to 60 v above cathode center tap potential. Generally the thruster body was allowed to float during the tests and discharge current was adjusted through the range 2 A to 10 A by controlling the alternating current through the refractory cathode.

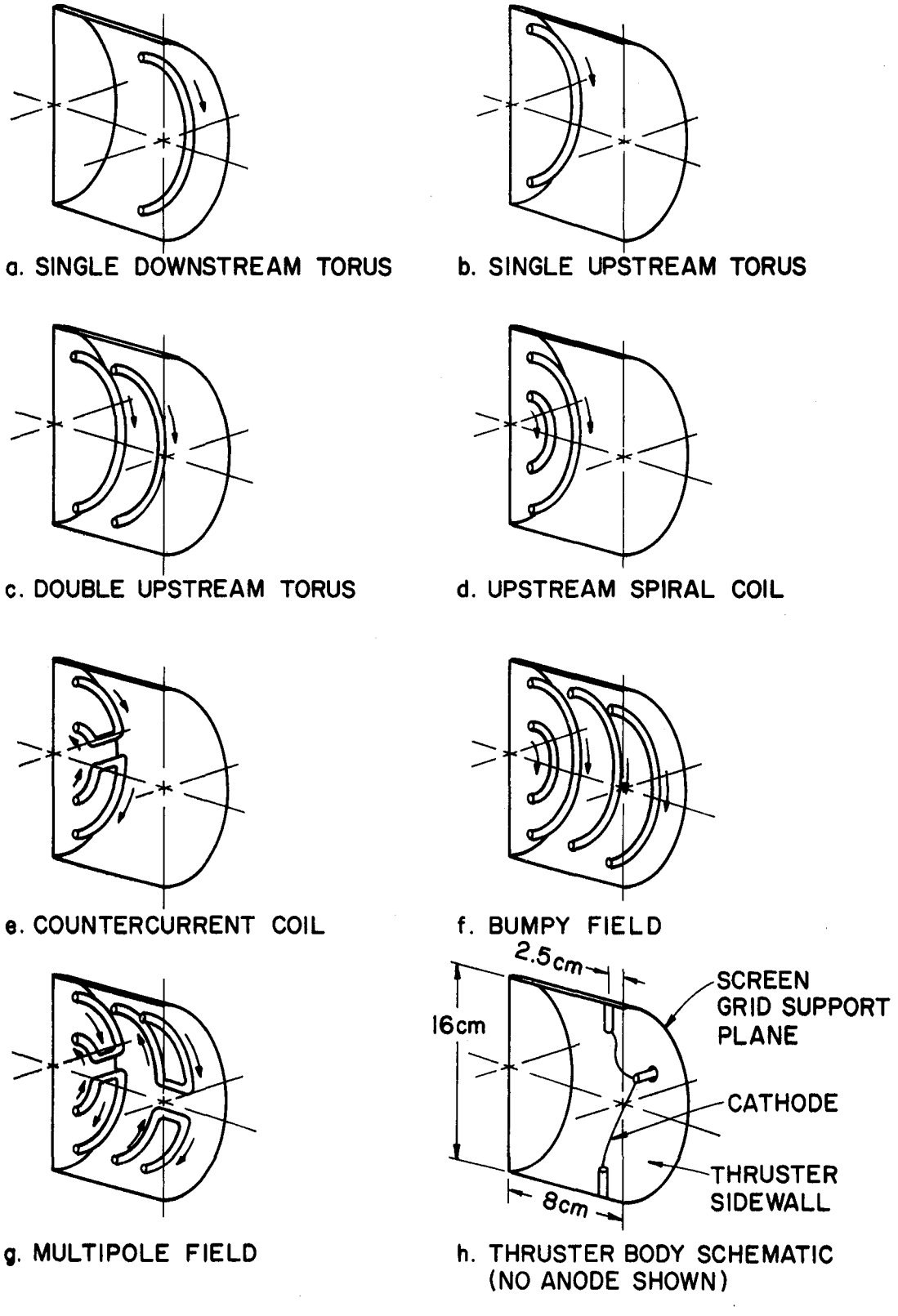

Figure 35. Flexible Magnetic Field Thruster Configurations.

The grids used had a 67% open area screen and a 30% open area accelerator. They were operated at a total accelerating voltage of 1500 v and a net-to-total accelerating voltage ratio of 0.67 with a cold grid spacing of 0.75 mm. Beam neutralization was accomplished using a refractory wire cathode. All tests were conducted in a 1.2 m dia. x 4.6 m long vacuum test facility. The usual discharge chamber related measurements of beam current, anode voltage and anode current were made at each operating condition.

Another rather unique measurement was made possible by the fact that the discharge chamber is designed so the cathode is isolated from the thruster body and screen grid. The positive high voltage is connected directly to the cathode centertap, and the body and screen grid are connected to this point through a power supply that can be used to bias the body and screen grid relative to positive high voltage (mean cathode) potential. With the thruster operating, the body and screen grid could be biased to -50 v; at this bias, electron collection on these surfaces was eliminated and the ion current to the surfaces could be measured. Applying this bias did not change the discharge chamber operation significantly. When the bias was applied, the current from the body and screen grid rose from zero to the value corresponding to the ion current being collected (I_i). At the same time the beam current would drop slightly. It was restored to its initial value however when the cathode current was increased to the point where the anode current also increased an amount I_i above its initial value. Physically the preceding sequence involves adjusting the anode current so the electrons required to neutralize the ion current to the walls are supplied through the bias supply rather than directly from the discharge chamber plasma. The -50 v bias voltage mentioned may seem excessive but it is required here because the refractory cathode supplies some very high energy electrons when

the alternating voltage cycle is at a minimum.

By measuring the ion current to the thruster body and screen grid in the manner suggested above one is provided with a powerful tool for evaluating thruster performance. It is really an extension of the Langmuir probe technique proposed by Sovey[28] and is essentially the same approach used by Siegfried in studying hollow cathodes.[17] In this case however the entire body and screen grid act as the probe. The value of the measurement lies in the fact that the body and screen grid ion current represents the current of ions produced in the chamber but not extracted through the grids. The sum of this current and the beam current is the total ion production rate. Knowing this total ion production rate one can compute the fraction of ions producted that are extracted (beam current-to-total production rate ratio) and the energy cost of a plasma ion (discharge power-to-total production rate ratio). The first of these parameters indicates the efficiency of the discharge chamber in directing ions through the grids; the second the efficiency of discharge chamber electrons in producing ions.

RESULTS

In the first tests conducted the single downstream toroidal anode shown in Fig. 35a was used. The major diameter of the torus was $\sim$ 11 cm, it was located 25 cm upstream of the grids and the cathode was 5.5 cm upstream of the grids. With this configuration the beam ion energy cost was about 600-900 eV/ion, the utilization was less than $\sim$ 30% and the magnetic field current could not be raised above 50 A or the discharge would extinguish even though the anode voltage was maintained at 50 v. When the anode was moved upstream (Fig. 35b) the discharge losses dropped by about 50 or 100 eV/ion presumably because the change induced potential gradients in the plasma

that encouraged greater ion migration toward the grids. The maximum utilization and maximum field current were not changed measurably. With the double upstream torus configuration (Fig. 35c) the available anode surface increased and it was possible to sustain the discharge at magnetic field currents of up to 80 A at anode voltages of 40 v. This resulted in a further lowering of the beam ion energy cost to 400-500 eV/ion and an increase in the utilization to about 35%. When the upstream spiral coil was installed (Fig. 35d) the performance was about the same as that observed with the double upstream torus.

At this point it was recognized that the magnetic field between the two coils in either configurations 35c or 35d tended to cancel because the current in both coils had a clockwise sense. It was postulated that reversing the direction of the current in one of the coils would increase the field between the coils by making the fields associated with each coil additive. This reversal was accomplished by installing the countercurrent coil configuration shown in Figure 35e. The beam ion energy cost and the utilization were considerably poorer with this configuration than it had been with the spiral coil (Fig. 35d) even though the anode lengths for the two configurations were both the same. The reason for this is related to the shapes of the magnetic fields and their capacity to direct ions back towards the discharge plasma rather than to the thruster body. The details of this process are discussed in the section of this report entitled "Controlling Ion Currents to Discharge Chamber Surfaces."

Since the performance of the upstream spiral coil (Fig. 35d) and the double torus (Fig. 35c) had both yielded fair performance it was considered likely that combining the concepts would give even better performance. The idea of the bumpy field configuration (Fig. 35f) which resulted from this

union provided a magnetic field barrier at essentially all of the wall surfaces thereby enhancing ion reflection at these surfaces. Testing showed that this configuration did indeed give good performance. The performance realized is shown in Figure 36 where performance curves for the upstream spiral coil anode and the bumpy field anode are compared. The performance of the bumpy field anode configuration is observed to be respectable particularly in consideration of the short discharge chamber length (8 cm) which probably imposes a limit on the utilization level that can be realized at a reasonable discharge power level. Figure 36 also shows that the bumpy field configuration can be operated at a 30 v discharge voltage as well as 40 and 50 v values. In fact in this configuration the source operated satisfactorily at a 20 v discharge voltage but its discharge tended to extinguish at higher discharge currents when the argon flow rate was less than $\sim$ 1580 mA.

Figure 37 shows the effect of magnetic field current (I_f) on discharge chamber performance. It is considered important to note that the most substantial changes occur as this current is increased from zero to 70 A and that performance changes with further increases to 130 A are less significant. Figure 38 shows how the performance of the bumpy field configuration varied with flow rate. As the data on the figure suggest the field current had to be reduced somewhat at lower flow rates to prevent the discharge from extinguishing. It is noted however that increasing the field current from 90 to 130 A resulted, as also suggested by Fig. 37 in relatively, minor performance improvements at all flow rates.

The nagging feeling that the increased magnetic field strength in the region between the anodes would improve performance, in spite of results obtained with the reversing current coil configuration, led to the

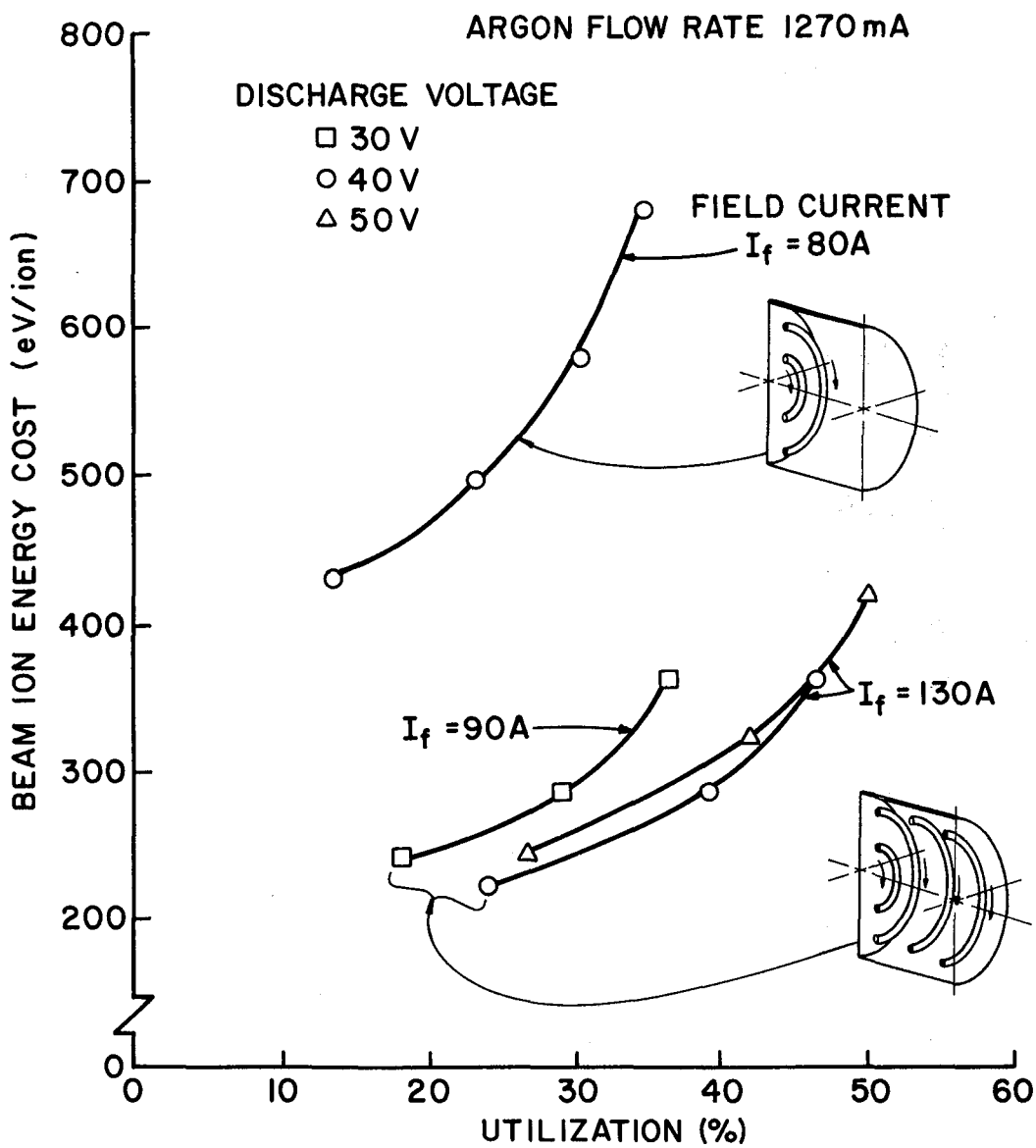

Figure 36. Effect of Magnetic Field Shape on Performance Curves.

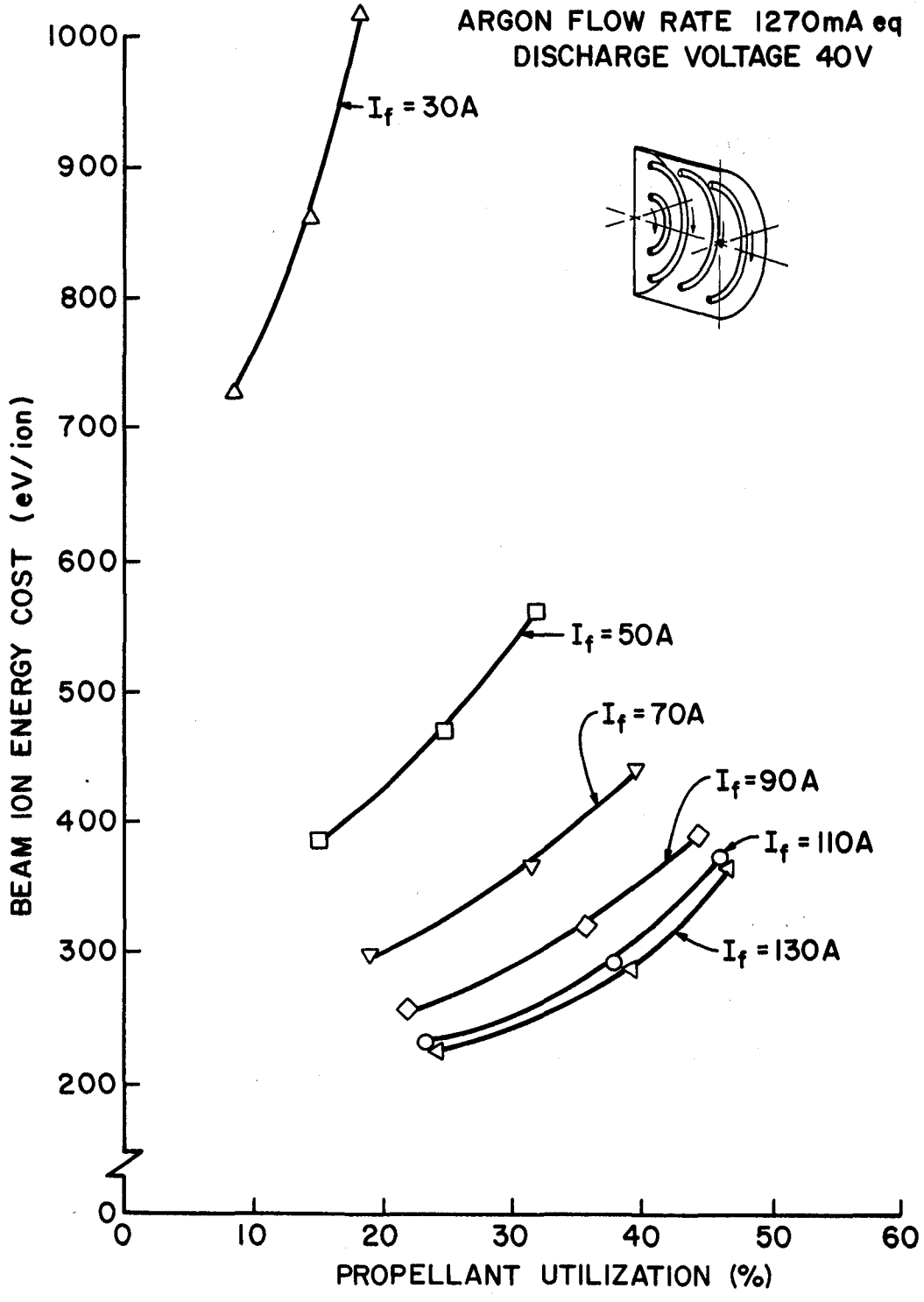

Figure 37. Effect of Field Current on Performance.

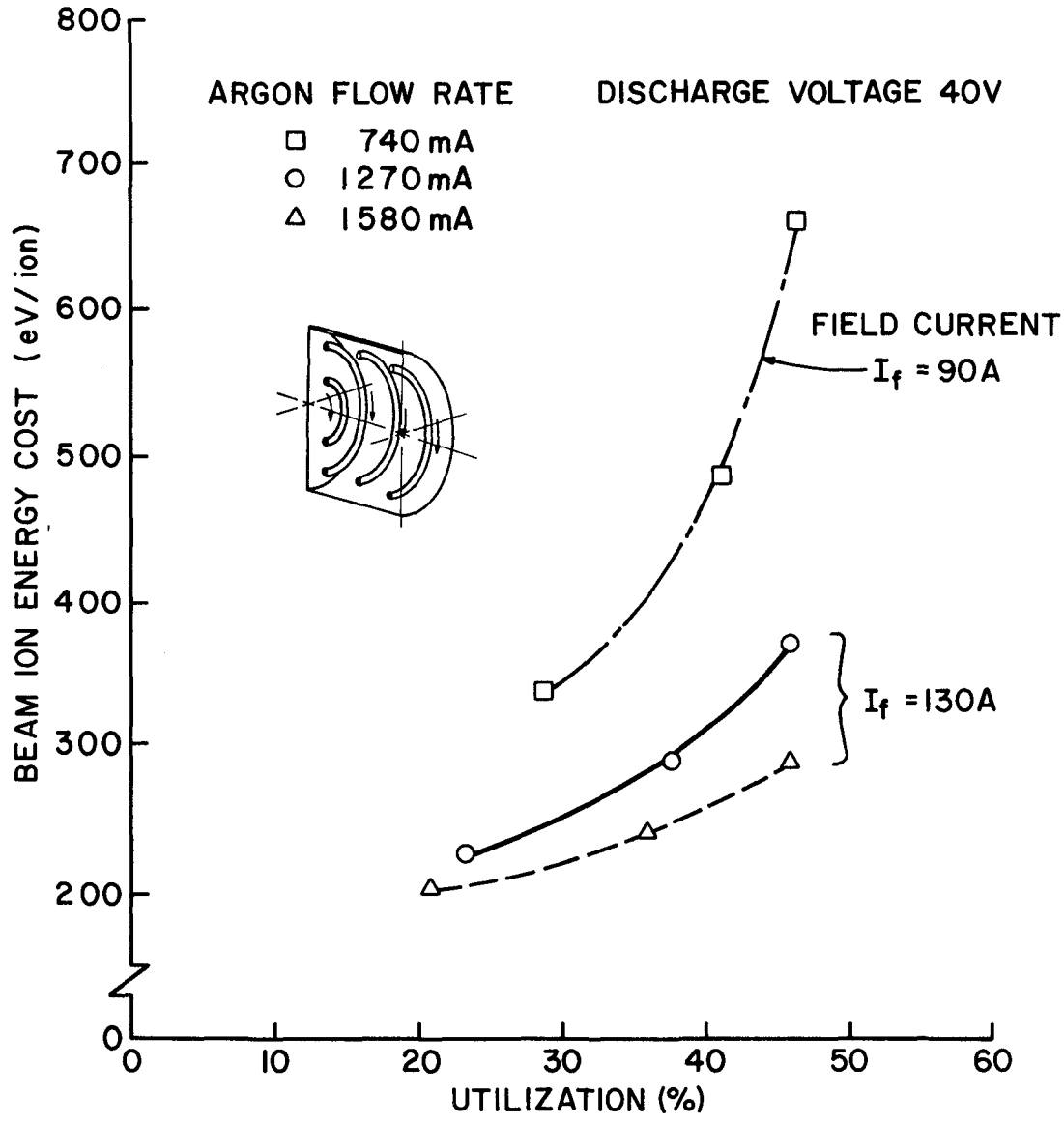

Figure 38. Effect of Flow Rate on Performance (Bumpy Field Configuration).

construction of the anode configuration shown in Fig. 35g. This configuration produced a magnetic field that looked like the ones observed in multipole thrusters. Tests showed that this configuration did not perform nearly as well as the bumpy field one. This again supported the theory of ion migration control discussed in the preceding chapter of this report.

Finally it is noted that all of the configurations shown in Fig. 35 operated very stably with no evidence of discharge oscillations being observed.

POTENTIAL FOR IMPROVEMENT

The copper coils used for anodes in the Flexible Field Thruster can be bent into essentially any configuration desired to achieve ion migration control. This can be done almost without concern for possible electron leaks to the anode through the magnetic field because the anode and its magnetic field are linked together. This makes the Flexible Field Thruster a particularly valuable tool for studying optimum discharge chamber configurations. A number of additional configurations slated for investigation are expected to yield both increased physical understanding of thruster phenomena and improved thruster performance. Ultimately it is hoped that a field configuration will be found for which essentially all ions produced in the discharge chamber will be directed toward the screen grid. If this could be done its consequences would be substantial. In particular it could mean: 1) the beam ion energy cost would approach the plasma ion energy cost times the reciprocal of the limiting ion extraction fraction (the fraction should approach one plus the ratio of screen grid closed-to-open areas), 2) the discharge chamber could be made as long as desired

without any discharge power penalty so the utilization efficiency could approach 100%, 3) grid supports could be introduced through the discharge chamber or small diameter discharge chambers could be used without a discharge power penalty so closely spaced grids capable of very high current density operation could be used, and 4) sputtering damage to all but the screen grid surface could be essentially eliminated.

The evidence that the high performance suggested in the preceding paragraph is achievable is obtained from curves like the ones given in Figs. 39 and 40. The upper plots of Fig. 39 are typical curves showing the fraction of ions produced in the discharge chamber that are extracted through grids as a function of magnetic field current. They show that while the extracted ion fraction for two anode configurations could not be controlled by adjusting the magnetic field, it was possible to exercise this control with the bumpy field design. It is believed that other designs superior to the bumpy field configuration can be found. With regard to these plots it is considered important to note that the identical curves were obtained over wide ranges of flow rates, anode voltages and anode currents. In other words the ability to control the extracted ion fraction is determined by the overall magnetic field shape and magnitude almost exclusively.

The lower plots of Fig. 39 show how the energy cost of plasma ions was affected by magnetic field current at a typical flow rate and anode current for the same discharge chamber configurations of the upper plots. This energy cost of a plasma ion is an indication of the efficiency of the utilization of primary electron energy in ionizing the argon propellant. These curves show this quantity is dependent on discharge chamber configuration also, but when the field current can be increased to $\gtrsim$ 100 A without

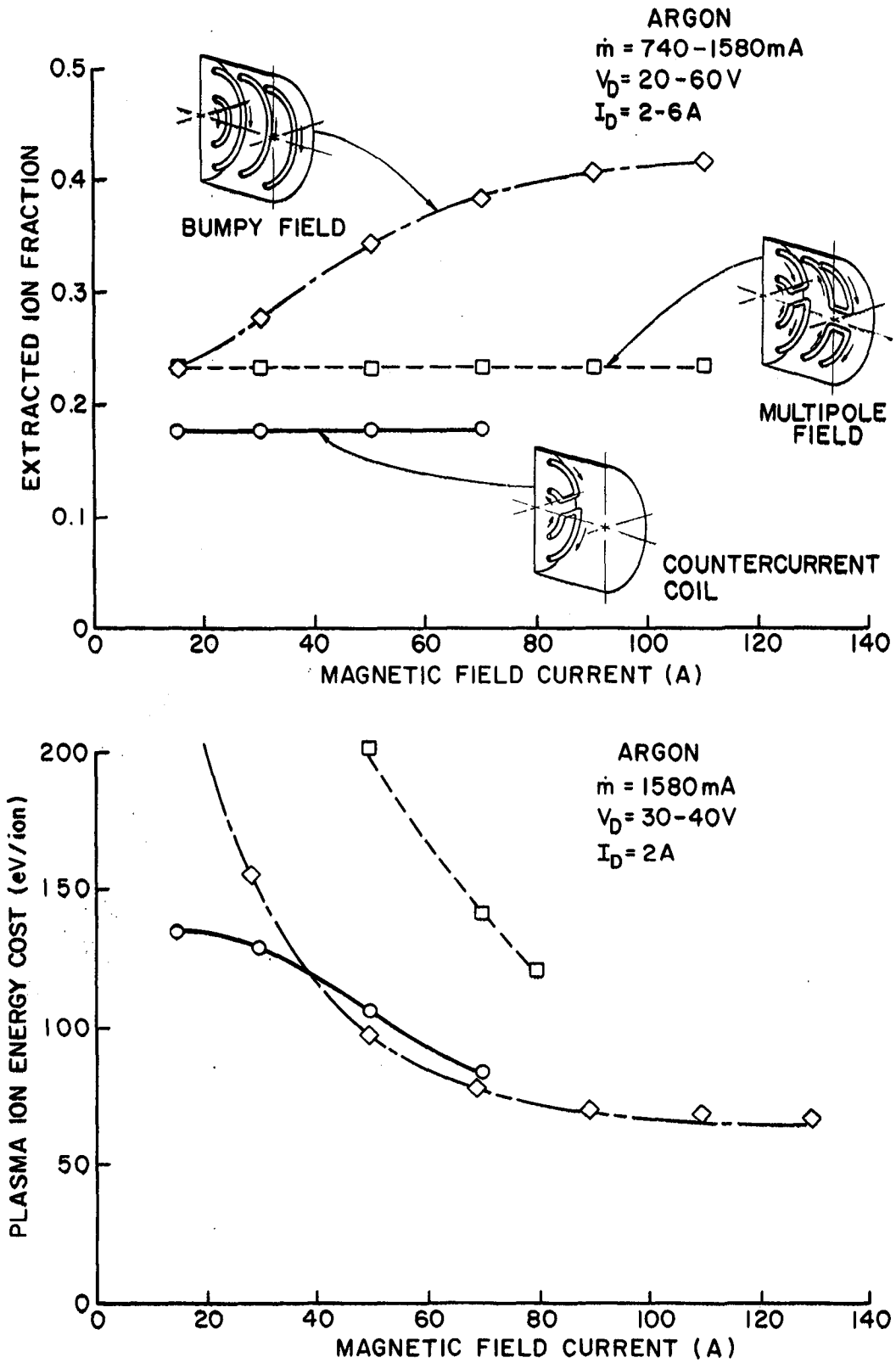

Figure 39. Effect of Magnetic Field Configuration on Discharge Chamber Performance Indicators.

extinguishing the discharge this cost approaches the same value (60 to 70 eV/plasma ion) for the flow rate, anode current and anode voltage appropriate to this figure. Hence it appears that the limiting value of the plasma ion cost is relatively independent of overall magnetic field shape. Finally it is noted that lower magnetic field currents would probably be required if a hollow cathode were used rather than a refractory cathode because the hollow cathode produces a more nearly monoenergetic primary electron group.

Figure 40 shows typical curves indicating the effects of flow rate, discharge voltage and discharge current on the energy cost of a plasma ion. While these data were obtained with the bumpy field design results obtained with other configurations were very similar. As expected increasing the magnetic field current increased the degree of anode shielding from primary electrons and causes the plasma ion energy cost to drop in the lower plot of Fig. 39 and in both Fig. 40 plots. The data of Fig. 40 suggest the energy cost of a plasma ion increases with discharge current and decreases with flow rate. Surprisingly however it is relatively independent of anode voltage.

CONCLUSIONS

The flexible magnetic field thruster concept is workable. Magnetic field currents of the order of 100 A are required through 3 mm diameter tubing to generate the fields required to shield the tubing from the high energy primary electrons in a typical discharge plasma. The bumpy field configuration gives the best performance of the configurations tested to date. By measuring the ion currents to the thruster body and screen grid one can compute the fraction of ions produced in the discharge that are

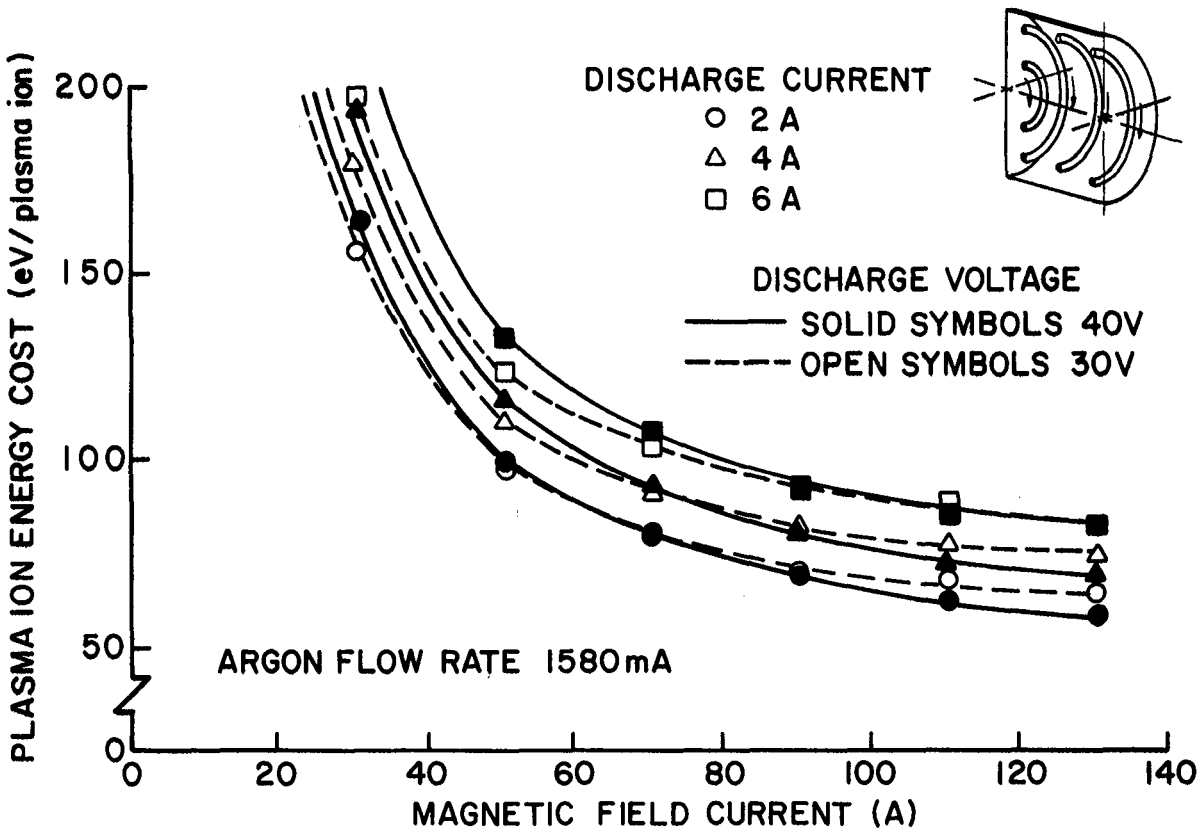

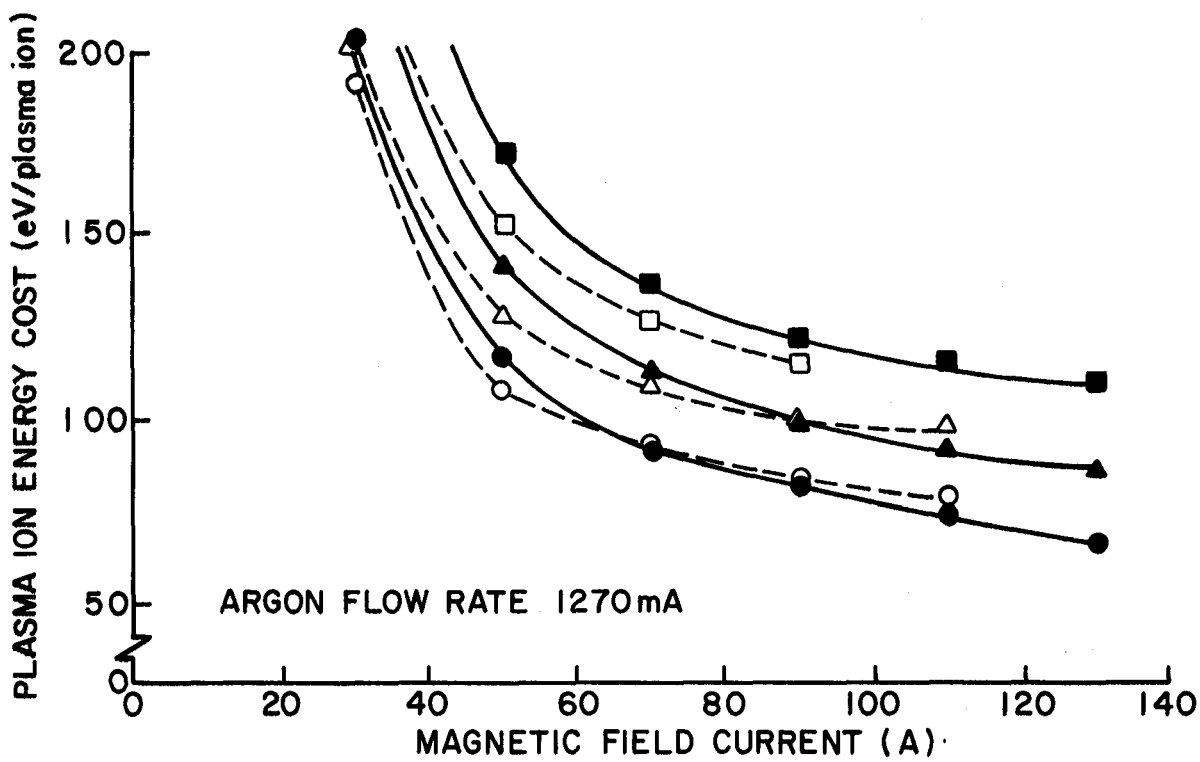

Figure 40. Plasma Ion Energy Costs in the Bumpy Field Configuration.

extracted in the beam and the energy cost of plasma ions. Both of these quantities indicate it should be possible to realize further improvements in the performance of the flexible magnetic field thruster.

TWO TEMPERATURE SAHA EQUATION

C. E. Mitchell

In the hollow cathode as well as in other plasmas of practical interest it appears that to a good degree of approximation the electrons are in equilibrium at one temperature, say T_e, while the neutrals and ions are in equilibrium at a significantly lower temperature T_N. Equilibrium here is taken to mean that the electrons and the ions plus neutrals exhibit Maxwell-Boltzmann distributions at the temperatures T_e and T_N, respectively. Assuming that such a two temperature equilibrium is the case it seems reasonable to ask if an expression for α, the ionization fraction in terms of the temperatures T_e and T_N exists.

In fact such a two temperature or expanded Saha equation does exist and has been used with some success by Bessling[29] and later by Siegfried.[30] The equation used by them is

$$\frac{\alpha^{1+\beta}}{(1-\alpha)^{\beta}(\beta+\alpha)} = \frac{1}{P}\frac{(2\pi m_e)^{3/2}}{h^3}\,(kT_e)^{5/2}\,\left(\frac{g_I}{g_N}\right)^{\beta} 2\exp[-E_I/kT_e] \qquad (18)$$

where $\beta = T_N/T_e$

g_I/g_N - ratio of electronic ground state degeneracy for singly ionized and neutral atoms

E_I - ionization energy

P - total pressure

h - Planck's constant

m_e - electron mass

k - Boltzmann's constant

α - ionization fraction, $\frac{N_e}{N_I + N_N}$

N_e - Number of electrons

N_I - Number of ions

N_N - Number of neutrals

The derivation of the Eq. 18 has proved difficult to find in the literature. Though Siegfried conducted a literature search and obtained Bessling's original reference, directly from him, no development of the expression or explanation of the underlying assumptions could be found. Consequently it was decided to attempt to develop the expression directly from the well known results of statistical thermodynamics. It is the intent here to give a brief presentation of the derivation of Eq. 18 along with the assumptions necessary for its derivation.

THEORETICAL DEVELOPMENT

Assuming that two separate equilibrium populations exist, one composed of electrons at T_e and the other of ions and neutrals at T_N then the following equilibrium relationships describing numbers of particles in the i^{th} energy state hold

$$\frac{N_{e,i}}{N_e} = \frac{g_{e,i}\ \exp[-E_{e,i}/kT_e]}{Z_e} \tag{19}$$

$$\frac{N_{I,i}}{N_I} = \frac{g_{I,i}\ \exp[-E_{I,i}/kT_N]}{Z_I} \tag{20}$$

$$\frac{N_{N,i}}{N_N} = \frac{g_{N,i}\ \exp[-E_{N,i}/kT_N]}{Z_N} \tag{21}$$

where E_i represents the energy of the i^{th} state of a given specie and the Z's are partition functions given by

$$Z_e = \sum_{\substack{\text{all}\\ \text{states}\\ i}} g_e \exp[-E_{e,i}/kT_e] \tag{22}$$

$$Z_I = \sum_{\substack{\text{all}\\ \text{states}\\ i}} g_{I,i} \exp[-E_{I,i}/kT_N] \tag{23}$$

$$Z_N = \sum_{\substack{\text{all}\\ \text{states}\\ i}} g_{N,i} \exp[-E_{N,i}/kT_N] \exp[E_I/kT_N] \tag{24}$$

Carrying out the summations in Eqs. 22, 23 and 24 yields

$$Z_e = 2 \frac{V}{h^3} (2\pi m_e kT_e)^{3/2} \tag{25}$$

$$Z_N = g_N \frac{V}{h^3} (2\pi m_N kT_N)^{3/2} \exp[E_I/kT_N] \tag{26}$$

$$Z_I = \frac{g_I V}{h^3} (2\pi m_N kT_N)^{3/2} \tag{27}$$

These quantities can be used in turn to determine the entropies and internal energies respectively of the electrons, neutrals and ions from the following expressions.

$$S_e = \frac{U_e}{T_e} + N_e \left[\ell n(\frac{Z_e}{N_e}) + 1 \right] k \tag{28}$$

$$S_I = \frac{U_I}{T_N} + N_I \left[\ell n(\frac{Z_I}{N_I}) + 1 \right] k \tag{29}$$

$$S_N = \frac{U_N}{T_N} + N_N \left[\ell n(\frac{Z_N}{N_N}) + 1 \right] k \tag{30}$$

$$U_e = N_e kT_e^2 \frac{\partial(\ell n\ Z_e)}{\partial\ T} = \frac{3}{2} kT_e\ N_e \tag{31}$$

$$U_N = N_N\ kT_n^2 \frac{\partial(\ell n\ Z_N)}{\partial\ T} = \frac{3}{2} kT_N\ N_N - N_N\ E_I \tag{32}$$

$$U_I = N_I\ kT_N^2\ \frac{\partial(\ell n\ Z_I)}{\partial\ T} = \frac{3}{2}\ kT_N\ N_N \tag{33}$$

If the combined system were nonreacting the expressions above could be used for arbitrary T_e, T_N, N_e, N_I, N_N. If reaction is allowed in the sense that N_e, N_I, N_N can change then one might expect that, for given T_e and T_N, a unique set of N_e, N_N, N_I would be most highly favored and in fact would define equilibrium for the combined system. Of course, since

$$\begin{aligned} N_e &= N_I = \alpha\ N_A \\ N_A &= N_N + N_I = \text{constant} \\ \text{and } N_N &= (1-\alpha)\ N_A \end{aligned} \tag{34}$$

then really for fixed T_e, T_N we could also solve for α, the ionization fraction.

For reacting mixtures at a single temperature it is well known that the condition for equilibrium of a constant volume system is $dF = 0$, where $F = U - TS$ is the Helmholtz free energy of the complete system. Proceeding formally to require that $dF = 0$ also in the two temperature case leads to

$$d\left[(U_e - T_e\ S_e) + (U_I - T_N\ S_I) + (U_N - T_N\ S_N)\right] = 0 \tag{35}$$

or using Eqs. 28, 29, and 30 this becomes

$$d\left[N_e\ kT_e\left(\ell n(\frac{Z_e}{N_e}) + 1\right) + N_I\ kT_N\left(\ell n(\frac{Z_I}{N_I}) + 1\right) + N_N kT_N\left(\ell n\frac{Z_N}{N_N} + 1\right)\right] = 0 \tag{36}$$

The differential operation expressed above is to be taken with N_e, N_N and N_I as independent variables.

Thus

$$T_e\left(\ell n(\frac{Z_e}{N_e})\right)dN_e + T_N\left(\ell n(\frac{Z_I}{N_I})\right)dN_I + T_N\left(\ell n(\frac{Z_N}{N_N})\right)dN_N = 0 \tag{37}$$

$$\begin{aligned} \text{but } dN_e &= dN_I \\ \text{and } dN_e &= -dN_N \end{aligned} \tag{38}$$

so Eq. 37 becomes

$$\left(T_e \ln \left(\frac{Z_e}{N_e}\right) + T_N \ln\left(\frac{Z_I}{N_I}\right) - T_N \ln\left(\frac{Z_N}{N_N}\right) \right) dN_e = 0 . \tag{39}$$

Since dN_e is arbitrary the expression in brackets must vanish if $dF = 0$. Dividing by T_e yields

$$\frac{Z_e}{N_e} \left(\frac{Z_I}{N_I}\right)^{\beta} \left(\frac{N_N}{Z_N}\right)^{\beta} = 1$$

or

$$\left(\frac{N_N}{N_I}\right)^{\beta} \frac{1}{N_e} = \left(\frac{Z_N}{Z_I}\right)^{\beta} \frac{1}{Z_e} \tag{40}$$

using Eqs. 25, 26, and 27 and the definition of the ionization fraction α, Eq. 40 becomes

$$\frac{\alpha^{1+\beta}}{(1-\alpha)^{\beta}} = \frac{V}{N_A} 2(2\pi m_e kT_e)^{3/2} \left(\frac{g_I}{g_N}\right)^{\beta} \exp[-E_I/kT_e] \tag{41}$$

The ideal gas law can now be invoked to bring the pressure (P) and volume (V) of the system into the equations.

$$PV = (N_I + N_N)\, kT_N + N_e\, kT_e$$

$$\text{or} \quad \frac{V}{N_A} = \frac{k\, T_e(\beta+\alpha)}{P} \tag{42}$$

Using this expression Eq. 41 becomes

$$\frac{\alpha^{1+\beta}}{(1-\alpha)^{\beta}(\beta+\alpha)} = \frac{(2\pi m_e)^{3/2}}{P\, h^3} (kT_e)^{5/2} \left(\frac{g_I}{g_N}\right)^{\beta} \exp[-E_I/kT_e] \tag{43}$$

which is Equation 18, Bessling's expression.

In assessing the assumptions leading to Equation 43 it is clear that as long as the fundamental assumption of thermal equilibrium of two different populations at two different temperatures holds, then all expressions through Equation 43 must be true and in fact are just definitive of the two temperature equilibrium. The critical remaining assumption is the one determining equilibrium, $dF = 0$. For the case of single temperature

reactive equilibrium F measures the availability of the system relative to a single dead state at T, the uniform system and surroundings (or bath) temperature. When the system is to react at two fixed temperatures the condition dF = 0 as used above is to be interpreted as requiring that the sum of the availability of the electron system relative to a dead state (or bath) at T_e plus the availability of the ions and neutrals relative to a different dead state (or bath) at T_N, must be a minimum. The bath at T_e can exchange energy only with the electrons; the bath at T_N can exchange energy only with the ions and neutrals. No energy exchange between the two baths or reservoirs is assumed. With these constraints in place the solution given above for α represents an equilibrium solution in the sense that moving to any other value of α would require an increase in the total free energy of the system as defined. For an isolated system no mechanism for increasing this potential exists and the system remains at the minimum potential (equilibrium).

It should be pointed out, however, that in the case of single temperature reactive equilibrium, the relationship between α and T determined by the condition dF = 0, would prevail even if the system once in equilibrium were to be insulated from all baths and reservoirs. In the case of the two temperature system this would not be true. Indeed, if the system at the equilibrium point given by Equation 23, were to be insulated from the two baths (or reservoirs) at T_e and T_N the system would tend toward a single temperature with the equilibrium value of α determined by the usual form of the Saha equation applied at the final temperature.

8 cm DIAMETER THRUSTER OPERATION

The 8 cm diameter mercury ion thruster (SIT 8)[4] was designed initially for operation at a beam current of 0.072 A. Subsequently, this thruster was operated at substantially higher discharge and beam current levels at both the NASA Lewis and Hughes Research Centers. In support of these efforts an 8 cm diameter thruster was also operated at high power at Colorado State University. The purpose of this work was to determine how discharge plasma properties were affected by operation at high discharge power levels. These properties were measured using a conventional non-emitting Langmuir probe[31] 0.074 cm in diameter by 0.127 cm long. Probe traces were analyzed using the procedure developed by Beattie.[32]

RESULTS

The performance of the SIT 8 thruster at discharge current levels ranging from 1 to 4.5 amps is illustrated by the data given in the first seven columns of Table I. These performance data, which appear to be similar to results obtained at NASA Lewis, were collected with a screen voltage of +1200 V and an accelerator grid potential of -600 V. Plasma property data measured 0.6, 3.8 and 7.0 cm downstream of the baffle on the thruster centerline are shown in the next three columns of Table I. For reference purposes it is noted that the screen grid is 8.4 cm downstream of the baffle. The Langmuir probe traces from which the plasma results of Table I were obtained seemed to be fit better by a pure Maxwellian distribution function than by a Maxwellian plus monoenergetic one so the data do not include primary electron energies and densities. It is considered noteworthy that the electron temperature seems to remain essentially constant as axial location is varied while electron density drops off rapidly as one approaches the screen grid.

Table I

High Power SIT 8 Operating Data

Test No.	Dischg. Current (A)	Dischg. Voltage (V)	Beam Current (mA)	Flow Rate (mA)	Utiliz. (%)	Dischg. Power (eV/ion)	Elec. Temp (eV)	Elec. Density (cm^{-3})	Plasma Potential (V)	Probe Location * (cm)
1	1.0	39.0	83	92	90	431	6.0	$1.6x10^{11}$	29.7	7.0
							6.4	$2.6x10^{11}$	33.5	3.8
							7.1	$2.2x10^{11}$	35.1	0.6
2	1.0	34.3	83	115	72	379	6.5	$1.2x10^{11}$	34.0	7.0
							6.5	$1.6x10^{11}$	35.2	3.8
							7.0	$1.3x10^{11}$	35.2	0.6
3	2.0	30.0	151	166	91	367	5.9	$2.7x10^{11}$	24.6	7.0
							5.7	$5.5x10^{11}$	27.8	3.8
							6.1	$5.5x10^{11}$	30.0	0.6
4	2.0	29.0	162	204	79	329	5.6	$3.4x10^{11}$	24.9	7.0
							5.9	$5.8x10^{11}$	28.8	3.8
							6.2	$6.0x10^{11}$	30.9	0.6
5	2.0	28.4	173	216	80	300	5.5	$4.1x10^{11}$	26.0	7.0
							5.3	$8.0x10^{11}$	29.2	3.8
							5.5	$8.4x10^{11}$	30.2	0.6
6	2.0	27.4	183	255	72	272	4.0	$4.9x10^{11}$	24.1	7.0
							3.7	$12.1x10^{11}$	27.2	3.8
							3.7	$12.3x10^{11}$	27.4	0.6
7	3.0	29.6	168	190	88	499	5.7	$3.1x10^{11}$	22.9	7.0
							6.3	$6.8x10^{11}$	28.3	3.8
							6.4	$7.7x10^{11}$	29.4	0.6
8	3.0	28.4	196	226	87	406	5.4	$4.6x10^{11}$	23.6	7.0
							5.7	$9.9x10^{11}$	28.1	3.8
							5.6	$10.3x10^{11}$	28.4	0.6
9	3.0	26.5	228	294	78	322	4.0	$7.1x10^{11}$	23.7	7.0
							4.0	$11.7x10^{11}$	25.5	3.8
							4.0	$15.2x10^{11}$	26.4	0.6
10	4.5	28.3	222	251	88	545	5.1	$4.3x10^{11}$	20.7	7.0
							5.4	$11.4x10^{11}$	24.9	3.8
							5.9	$12.1x10^{11}$	27.6	0.6

* Measured downstream from the baffle on the thruster centerline.

Table I (Continued)

Test No.	Dischg. Current (A)	Dischg. Voltage (V)	Beam Current (mA)	Flow Rate (mA)	Utiliz. (%)	Dischg. Power (eV/ion)	Elec. Temp. (eV)	Elec. Density (cm^{-3})	Plasma Potential (V)	Probe Location (cm)
11	4.5	26.3	254	311	82	440	4.6	7.2×10^{11}	22.4	7.0
							4.3	13.8×10^{11}	23.8	3.8
							4.6	12.4×10^{11}	24.9	0.6
12	4.5	25.4	273	356	77	393	4.1	7.4×10^{11}	22.8	7.0
							4.1	12.7×10^{11}	24.6	3.8
							3.7	17.7×10^{11}	23.7	0.6
13	4.5	25.0	277	389	71	381	3.4	9.5×10^{11}	21.6	7.0
							3.4	20.2×10^{11}	24.0	3.8
							3.1	20.7×10^{11}	23.2	0.6

Some of the results of Table I are also plotted in Figures 41 through 43. Figure 41 shows for example how the discharge voltage and beam current vary with propellant flow rate and discharge current. The range of flow rates shown in this Figure (and in Table I) at each discharge current level represents that range over which the very stable discharge conditions required for the collection of meaningful Langmuir probe data were achieved. At the lower discharge current level of 1 amp this range was small as the results of Figure 41 (circular symbols) indicate. At higher flow rate levels the range of flow rates was observed to increase. Figure 41 shows that the discharge voltage was essentially independent of discharge current and that the beam current was only slightly dependent on discharge current. The results of Fig. 42 suggest that stable thruster operation was realized at each flow rate/discharge current condition when the thruster was operating over essentially the same ranges of propellant utilization and discharge power.

Figure 43 shows the effects of propellant flow rate and discharge current on Maxwellian electron temperature and density at a location near the screen grid (1.4 cm upstream). Except at the lowest discharge current level the electron temperature is seen to decrease while the electron density increases with flow rate.

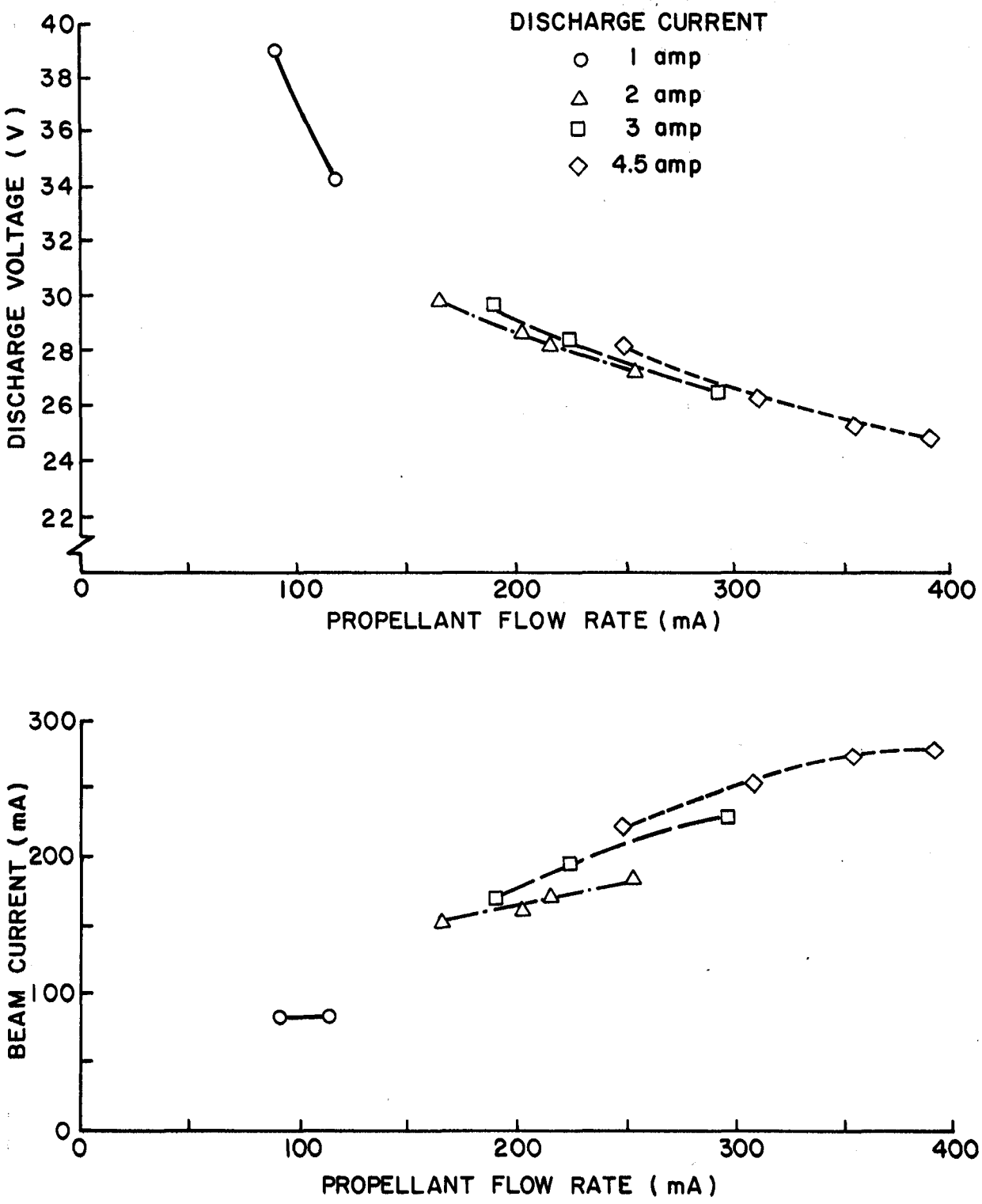

Figure 41. SIT 8 Performance at High Powers

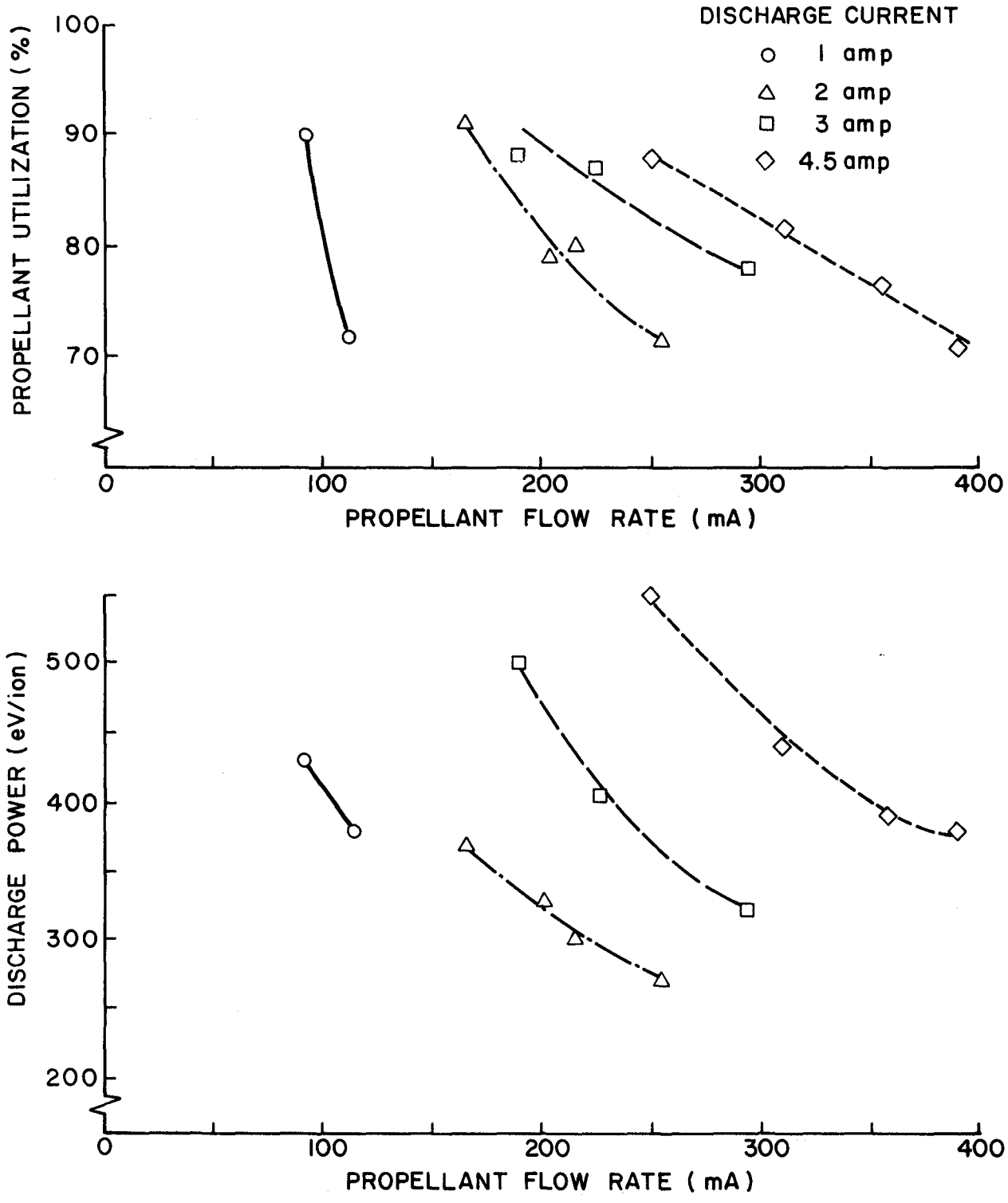

Figure 42. SIT 8 Performance at High Powers

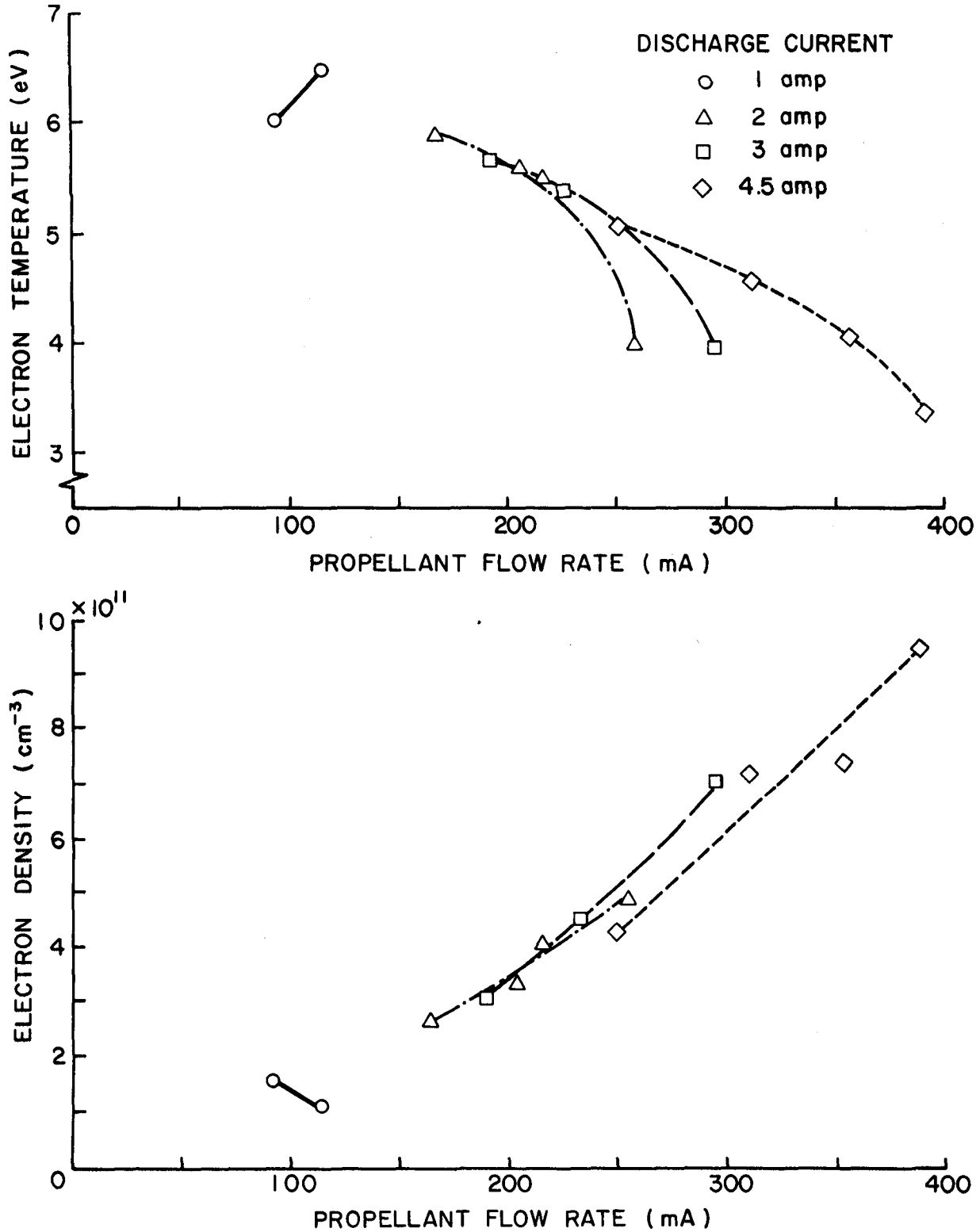

Figure 43. SIT 8 Plasma Properties 7 cm Downstream of Baffle on Thruster Centerline.

DISCUSSION OF RESULTS

As propellant flow rate and discharge power are increased in an ion thruster discharge chamber the electron density would be expected to increase. This increase in plasma density would in turn be reflected in an increase in ion beam current. Both of these results are observed in the data of Figs. 41 and 43. For the SIT 8 thruster there is no means of controlling the discharge impedance because all flow passes through the the cathode and there is no magnetic baffle. This means the increase in plasma density and neutral density must be accompanied by higher plasma conductivities in the baffle aperture region because of an increased collision frequency there. This in turn causes the drop in discharge voltage with propellant flow rate that is shown in Fig. 41. The increase in electron collision frequency that accompanies power and propellant flow increases would also be expected to extend into the main discharge chamber. Such an increase in collision frequency especially when accompanied by a discharge voltage decrease causes the electrons coming through the baffle aperture to thermalize quickly. This is considered to be the reason why a strong primary electron group was not identified in the main discharge plasma. Finally this high collision frequency should also facilitate more rapid energy removal from the Maxwellian electron population. Such a phenomenon would result in the decrease in electron temperature with flow rate that is shown in Fig. 43.

REFERENCES

1. Kerslake, W. R. and S. Domitz, "Neutralization Tests on the SERT II Spacecraft," AIAA Paper No. 79-2064, Oct/Nov. 1979.
2. Kerslake, W. R. and L. R. Ignaczak, "SERT II 1980 Extended Flight Thruster Experiments," AIAA Paper No. 81-0665, April, 1981.
3. Kaufman, H. R., "Plasma Physics Analysis of SERT II Operation," NASA CR-159814, January 1980.
4. Hyman, J., et al. "One-Millipound Mercury Ion Thruster." AIAA Paper 75-386, March 1975.
5. Aston, G., "Ion Extraction from a Plasma," NASA CR-159849, June 1980.
6. Kerslake, W. R., NASA Lewis Research Center, Private Communication, January 1982.
7. Aston, G., Kaufman, H. R., and Wilbur, P. J., "The Ion Beam Divergence Characteristics of Two-grid Accelerator Systems," AIAA Journal, Vol. 16, No. 5, May 1971, pp. 516-524.
8. Kaufman, H. R., "Technology of Electron Bombardment Ion Thrusters," Advances in Electronics and Physics, Vol. 36, Academic Press Inc., San Francisco, 1974.
9. Aston, G., private communication to P. J. Wilbur, Aug. 1979.
10. Aston, G., "The Ion-Optics of a Two-grid Electron-Bombardment Thruster," NASA CR-135034, May 1976.
11. Latham, W. C. and W. B. Adam, "Theoretical Analysis of a Grid Translation Beam Deflection System for a 30 cm Diameter Kaufman Thruster," NASA TM X-67911, 1971.
12. Latham, W. C., "Approximate Analysis of the Effects of Electrode Misalignments on Thrust Vector Control in Kaufman Thrusters," AIAA Paper No. 68-89, 1968.

13. Kaufman, H. R., J. M. E. Harper, and J. J. Cuomo, "Focused Ion Beam Designs for Sputter Deposition," Journal of Vac. Science & Tech., May/June 1979.

14. Whealton, J. H., "Linear Optics Theory of Ion Beamlet Steering," Rev. of Sci. Instrum., Vol. 48, No. 11, p. 1428, 1977.

15. Conrad, J. R., "Beamlet Steering by Aperture Displacement in Ion Sources with Large Acceleration-Deceleration Ratio," Rev. of Sci. Instrum. Vol. 51, No. 4, April 1980, pp. 418-423.

16. Stewart, L. D., J. Kim, and S. Matsuda, "Beam Focusing by Aperture Displacement in Multiampere Ion Sources," Rev. of Sci. Instrum., Vol. 46, No. 9, Sept. 1975.

17. Siegfried, D. E., "A Phenomenological Model Describing Orificed, Hollow Cathode Operation." Appears in "Ion and Advanced Electric Thruster Research - 1980," NASA CR-165253, Dec. 1980.

18. Fomenko, V. S., Handbook of Thermionic Properties, Plenum Press Data Division, New York, 1966.

19. Hensley, E. B., "Therminonic Emission Constants and their Interpretation," Journal of Applied Physics, Vol. 32, No. 2, Feb. 1961, pp. 301-308.

20. Kaufman, H. R., and R. S. Robinson, "Ion Source Design for Industrial Applications," AIAA Paper 81-0668, April 1981.

21. Longhurst, G. R., and P. J. Wilbur, "Plasma Property and Performance Prediction for Mercury Ion Thrusters," appears in Electric Propulsion and its Application to Space Missions, R. Finke ed., American Institute of Aeronautics and Astronautics, 1981, pp. 224-250.

22. Nakanishi, S. and R. C. Finke, "9799-Hour Durability Test of Five Centimeter Diameter Ion Thruster," Journal of Spacecraft and Rockets, v. 11, No. 8, Aug. 1974, pp. 560-566.

23. Collett, C. et al, "Thruster Endurance Test," NASA CR-135011, May 1976.

24. Aston, G., and P. J. Wilbur, "Ion Extraction from a Plasma," Journal of Applied Physics, Vol. 52, No. 4, April 1981.

25. Longhurst, G. R. and P. J. Wilbur, "Multipole Mercury Ion Thruster," AIAA Paper No. 78-682, April 1978.

26. Isaacson, G. C., "Multipole Gas Thruster Design," NASA CR-135101, June 1977.

27. Ramsey, W. D., "12 Centimeter Magnets-Electrostatic Containment Mercury Ion Thruster Development," AIAA Paper No. 71-692, June 1971.

28. Sovey, James S., "Performance of a Magnetic Multipole Line-Cusp Argon Ion Thruster," AIAA Paper No. 81-0745, April 1981.

29. Bessling, Harro, "Theorie der Hochtemperatur-Hohlkathode, ein Modell fur den Kathodenmechanismics" DFVLR Report DLR-FB 26-50, Stuttgart, Germany, 1976.

30. Siegfried, D. E., "Mercury Hollow Cathode Studies," appears in "Mercury Ion Thruster Research-1977," NASA CR-135317, Dec. 1977.

31. Wilbur, P. J., "An Experimental Investigation of a Hollow Cathode Discharge," NASA CR-120847, Dec. 1971, pp. 6, 7.

32. Beattie, J. R., "Numerical Procedure for Analyzing Langmuir Probe Data," AIAA Journal, V. 13, No. 7, July 1975, pp. 950-952.

33. Rawlin, V. K., "Studies of Dished Accelerator Grids for 30-cm Ion Thruster," AIAA Paper No. 73-1086, Nov. 1973.

34. Siegfried, D. E., "Probe Measurements Inside the Orificed, Hollow Cathode," appears in "Ion and Advanced Electric Thruster Research," NASA CR-165253, Dec. 1980, pp. 40-52.

APPENDIX A

EFFECTIVE ACCELERATION LENGTH FOR ION OPTICS

The bulk of the data that has been collected to describe the optical performance of ion thrusters has used the effective acceleration length ℓ_e shown in the inset sketch on Fig. A1.[7,8,10] This length is defined by the expression

$$\ell_e = (\ell_g^2 + d_s^2/4)^{\frac{1}{2}} \tag{A1}$$

where the quantities ℓ_g and d_s represent respectively the grid separation distance and screen hole diameter shown on the sketch in Fig. A1. The basic assumption involved when the effective acceleration length is defined this way is that the plasma sheath is located somewhere near the downstream edge of the accelerator grid. Recent work by Aston[5,24] has suggested however that for a grid set operating normally and having reasonable screen grid thicknesses the plasma sheath is located at the upstream surface of the screen grid as suggested by the sketch in Fig. A1. This suggests that the more appropriate effective acceleration length (ℓ_e') would include the screen grid thickness (t_s) as given by the equation

$$\ell_e' = [(\ell_g + t_s)^2 + d_s^2/4]^{\frac{1}{2}} \quad . \tag{A2}$$

The inclusion of this thickness has been suggested previously by Rawlin.[33]

It is appropriate to compare optical performance data analyzed using these two different definitions of effective acceleration length to compute normalized perveance per hole. The data of Fig. A1 do this for the case where accelerator screen hole diameter is being varied. These data are obtained from experimental results measured by Aston in his study of two grid optics.[10] In Fig. A1a the conventional definition of effective acceleration length (ℓ_e) given by Eq. A1 is used to normalize the current.

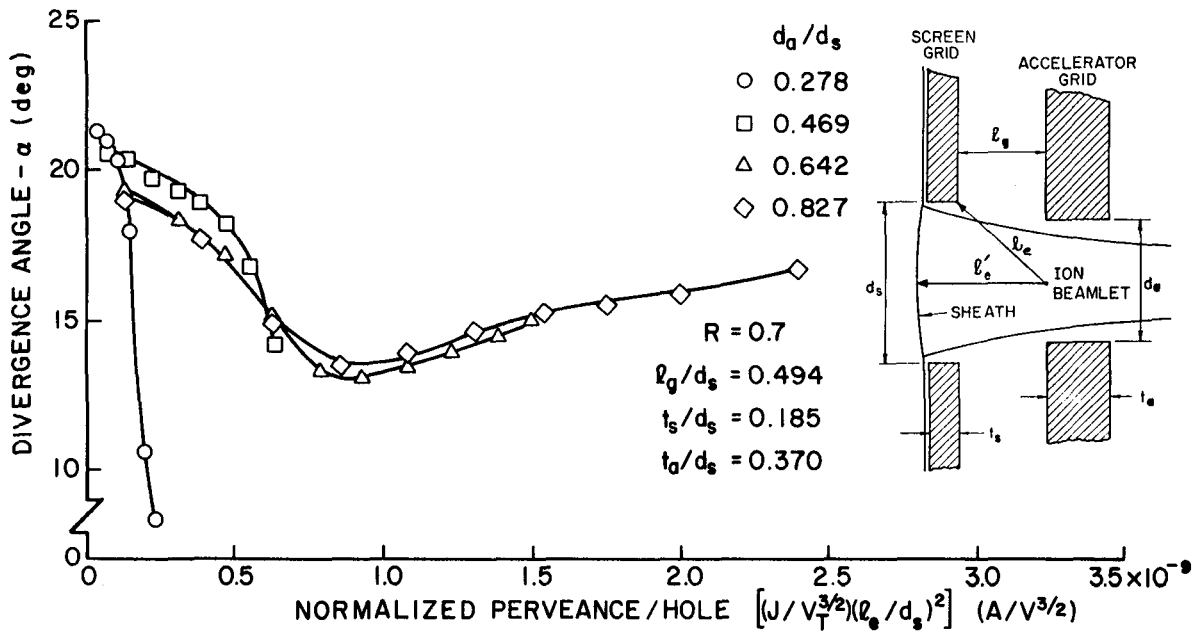

a. CONVENTIONAL ACCELERATION LENGTH

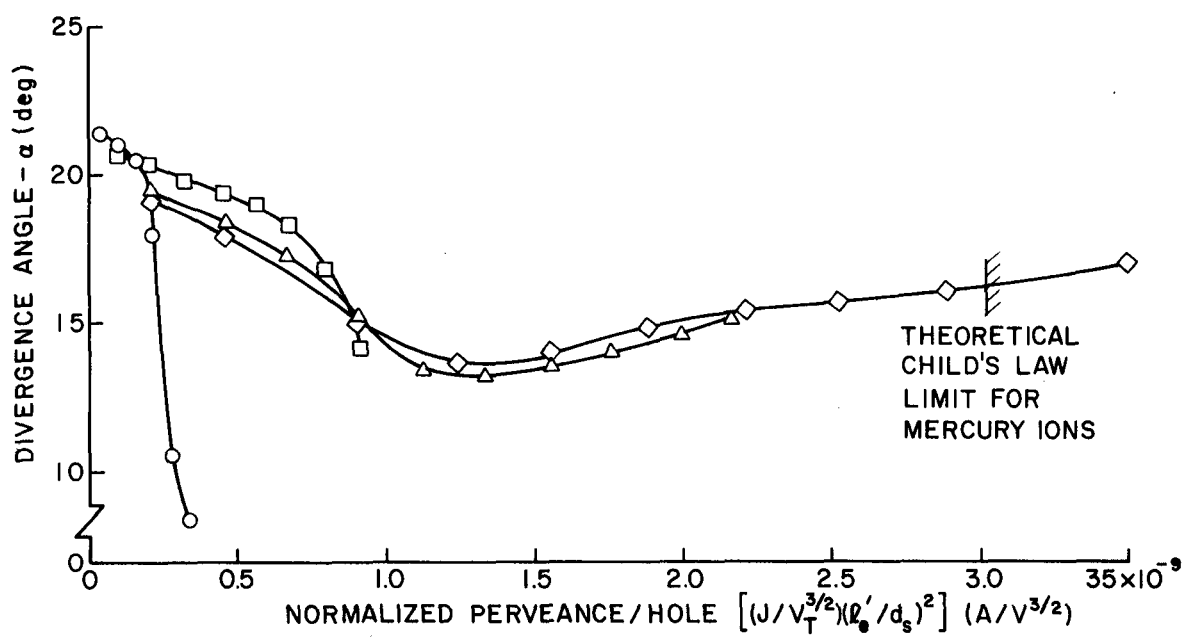

b. ACCELERATION LENGTH INCLUDING SCREEN GRID THICKNESS

Figure A1. Comparison of Divergence Curves for Different Effective Acceleration Lengths.

In Fig. A-1b the same results are presented but the ion currents have been normalized using the new acceleration distance (ℓ_e') defined by Eq. A2. Figure A-1b shows that with the new definition the normalized currents exceed the theoretical Child's Law limit by about 15% at the highest accelerator grid diameter. While this seems a little unpalatable initially it is reasonable to expect currents that exceed this limit because of the effects of ion focusing away from the screen grid webbing and into the ion beamlets and because of the affect of non-zero ion velocities at the plasma sheath.

Figure A-2 makes the same sort of comparison that Fig. A-1 does, but these data show the effect of screen grid thickness on the optical performance of the grids. A close comparison of the curves in the lower plot of Fig. A-2 shows that for all but the thickest screen grid the minimum beam divergence occurs at the same perveance condition when the effective acceleration distance ℓ_e' is used. This agreement is not as good when the conventional distance ℓ_e is used. Throughout this report the new definition of effective acceleration length ℓ_e' is used to correlate the data.

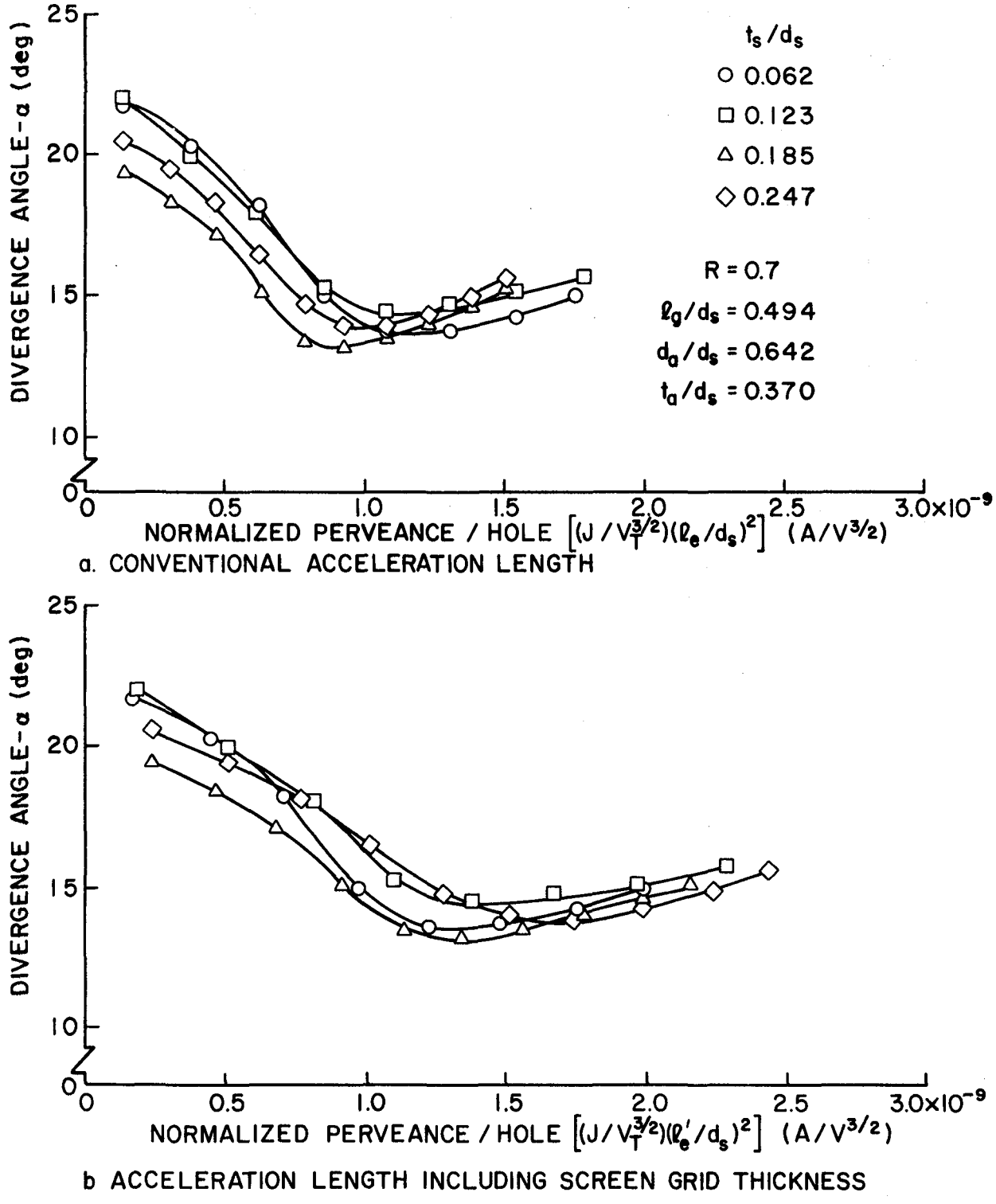

Figure A2. Comparison of Divergence Curves for Different Effective Acceleration Lengths.

APPENDIX B

DETERMINATION OF THE WORK FUNCTION OF AN EMITTING PATCH IN A HOLLOW CATHODE INSERT

Dan Siegfried

A small patch of tantalum foil isolated from and adjacent to a rolled foil, tantalum insert was connected to a power supply that could be used to bias the test patch (Fig. 26) with respect to the remainder of the insert and the orifice plate (both at cathode potential). Figure B-1 shows the characteristics of this patch for a typical test (#1 of Fig. 27) in the form of a plot of electron current to the patch vs. patch potential. At potentials above cathode potential this figure shows that the patch behaves as a Langmuir probe operating in the ion saturation region of the probe current-voltage characteristic. The electron temperature of the plasma adjacent to the patch can be obtained in the normal manner from the exponential rise in collected electron current (I_{ce}) in this region of the probe trace. The ion saturation current ($I_p(i)$) and floating potential (V_f) can then be used to estimate the plasma density and plasma potential.[17] The emission portion of the trace (that portion at potentials below cathode potential) gives the electron emission current ($I_p(e)$) from the patch as a function of negative patch potential at various patch temperatures. The negative portion of the curve is obtained by reducing the patch voltage, measuring the patch temperature and then reducing the voltage again and repeating the procedure. Down to potentials of about -15 v the curve looks relatively smooth. At about -20 v ($\sim$ 1100°C), however, irregularities in the curve appear and they become more pronounced as one goes to greater negative biases. These irregularities were introduced because of the procedure used in obtaining the data. This procedure involved slowly

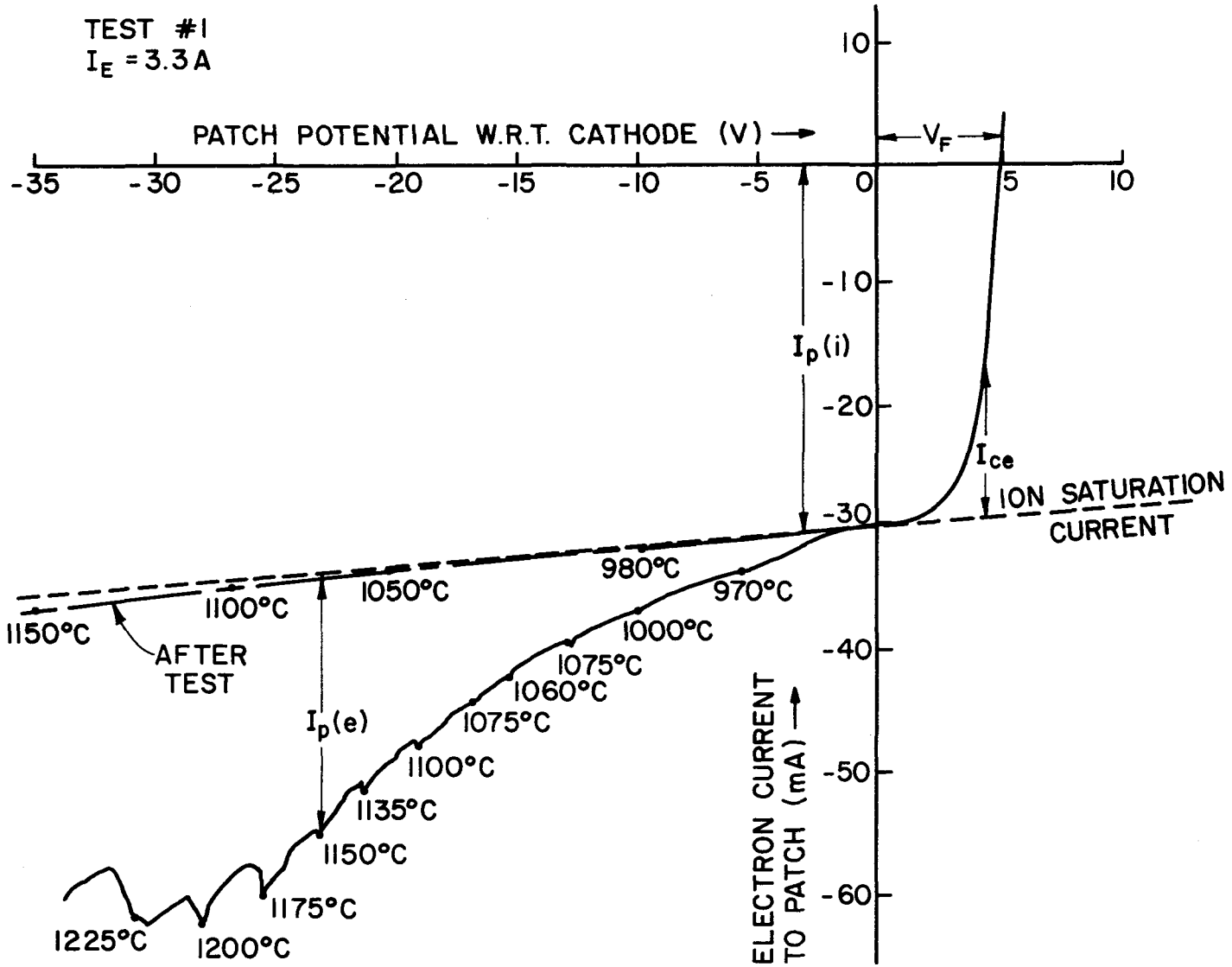

Figure B1. Patch Current-Voltage Characteristic.

reducing the patch potential to a given voltage and then measuring the patch temperature. During the time interval when this temperature measurement was being made the insert was bombarded by ions which probably tended to drive off some of the barium on its surface. This caused the work function to increase thereby causing the emission current ($I_p(e)$) to decrease and the hump to appear on the current-voltage curve. A further reduction in the patch potential caused its temperature to increase and with it the associated electron emission. The cycle was then repeated and at the lower bias values the size of the humps became progressively larger. If one went back to zero bias and repeated the test, the positive bias portion of the curve was unchanged but the negative bias portion would be shifted upward (lower electron emission currents). After several tests a substantial amount of the barium would be driven off and the patch would exhibit the curve labelled "After Test" on Fig. B-1. The dotted "ion saturation" curve shown in Fig. B-1 is extrapolated from the cathode (zero) potential region of the characteristic. It represents the limiting current-voltage characteristic curve for the case of zero electron emission. It was found that when the patch became depleted of barium, as in the curve labelled "After Test" that it could be reactivated by heating the entire cathode to $\sim$ 1250°C using the external heater. This presumably was due to a redistribution of barium from other, normally cooler, surfaces within the cathode. After reactivation, emission from the patch could be re-established, although usually at a somewhat different level. Work functions were obtained from the data by using the plasma properties (obtained from the positive bias portion of the curve) together with the electron emission current ($I_p(e)$), the patch surface temperature, the patch surface area and the patch bias potential in the Schottky equation for field-enhanced, thermionic emission (Eqs. 11 and 12).

APPENDIX C

LANGMUIR PROBING OF HIGH DENSITY PLASMAS

Dan Siegfried

THEORY

Very dense plasmas, such as those found inside the hollow cathode, make the use of conventional Langmuir probe techniques unsuitable because of the problems of probe overheating and melting at potentials near plasma potential. A probing technique which alleviates this problem uses a relatively large spherical probe and a method of analysis based on the ion saturation portion of the probe curve (i.e., well below plasma potential).[34] Although traces obtained within the hollow cathode are somewhat non-Maxwellian in shape it was suggested initially that the electron population inside the cathode could be reasonably described as being Maxwellian characterized by a single electron temperature.[34] More recent experimental work has suggested however that if the cathode model is to be extended to predict plasma properties, the probe analysis of the experimental data should be able to account for the non-Maxwellian nature of the probe trace. Such an analysis should be able as a minimum to model the plasma as a Maxwellian plus monoenergetic population. The existing computer programs were not capable of performing this analysis nor could they be easily modified to do so. For this reason a significant effort was expended on developing a new computer program to analyze the hollow cathode probe data using the ion saturation portion of the probe trace. This program uses the same non-linear least squares curve fitting technique that was used in an earlier program[32] and can fit the data to a function which contains the parameters needed to model the Maxwellian plus monoenergetic electron population. However, because the cathode plasma data are restricted to the ion saturation region of the probe trace, the logic

used in the iteration procedure for the current program is considerably different than that used in the previous one. Figure C1 shows a sketch of the conventional Langmuir probe trace which includes the electron saturation region and indicates the approximate location of plasma potential (ϕ) and floating potential (V_f). The detail in Figure C1 is an enlarged view of the ion saturation portion of the probe trace. The ion saturation current is shown as I_i. The electron current to the probe is shown as I and is measured with respect to the extrapolated ion saturation current (dashed line). If the electron population is Maxwellian plus monoenergetic then the curve shown in the detail of Figure C1 is the sum of two functions: an exponential function plus a linear one. The probe currents corresponding to this situation are indicated graphically in Figure C2. In this general case the data can be fitted to the following function

$$I = B_1 + B_2 V + B_3 \exp (B_4 V) \qquad (C1)$$

where the first two terms on the right hand side describe the monoenergetic electron current and the third term is the Maxwellian current for a distribution having a temperature $T_e = B_4^{-1}$. For the monoenergetic electrons, however, the slope of the probe current is discontinuous at the point marked V_{min} in Figure C2. This voltage, at which the primary electron current becomes zero, is equal to $-B_1/B_2$. Because of the discontinuity in the slope at this point, Eq. C1 holds only for voltages greater than V_{min}. Data pairs could be dropped for potentials less than V_{min} but it is obvious that if V_{min} is at all close to V_f then most of the data is ignored. The computer program handles this problem by performing the curve fit to Eq. C1 for the first six data pairs to the left of floating potential (if this does not converge to a solution for the B's in Eq. C1, then additional data pairs

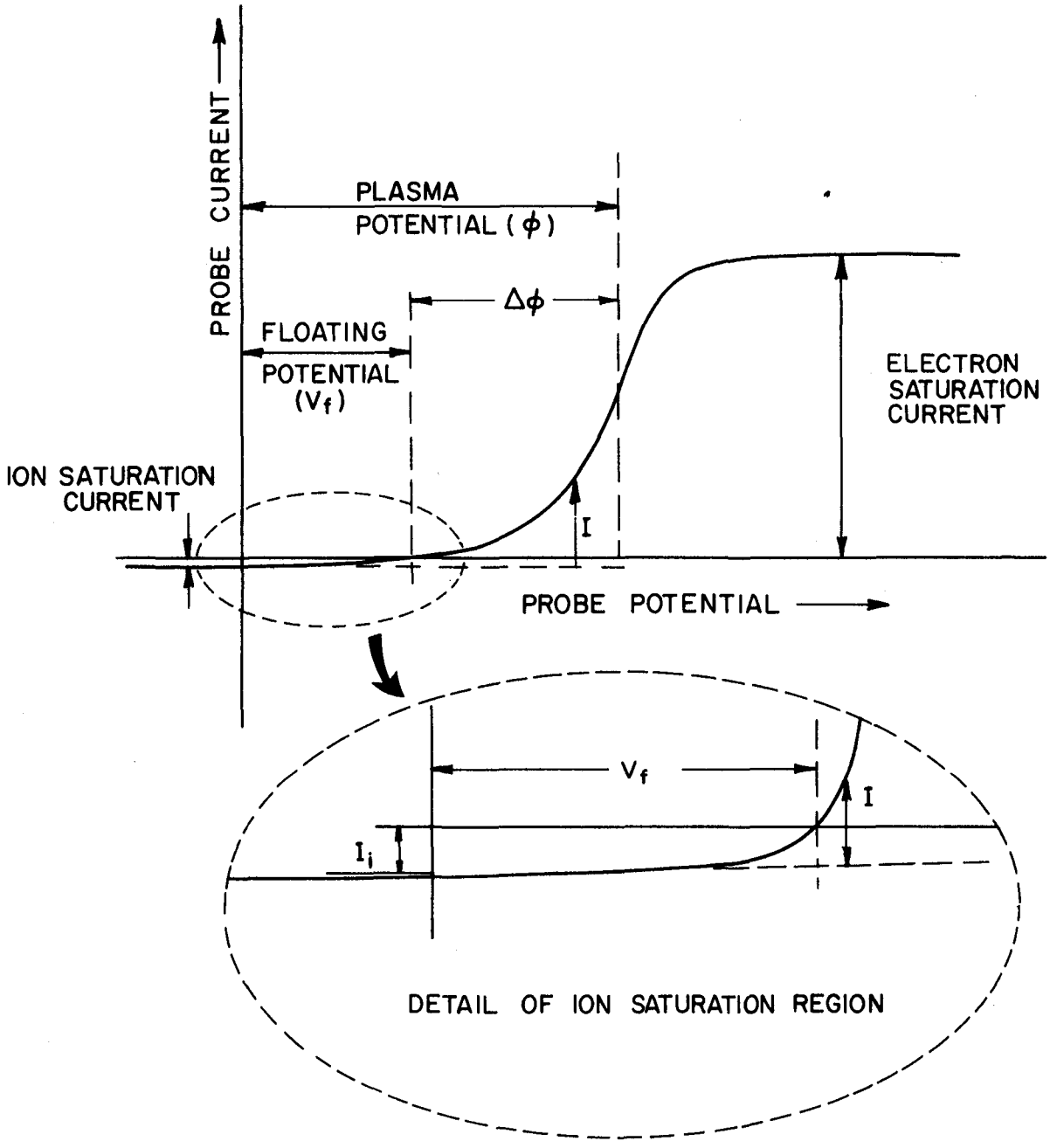

Figure C1. Typical Probe Trace.

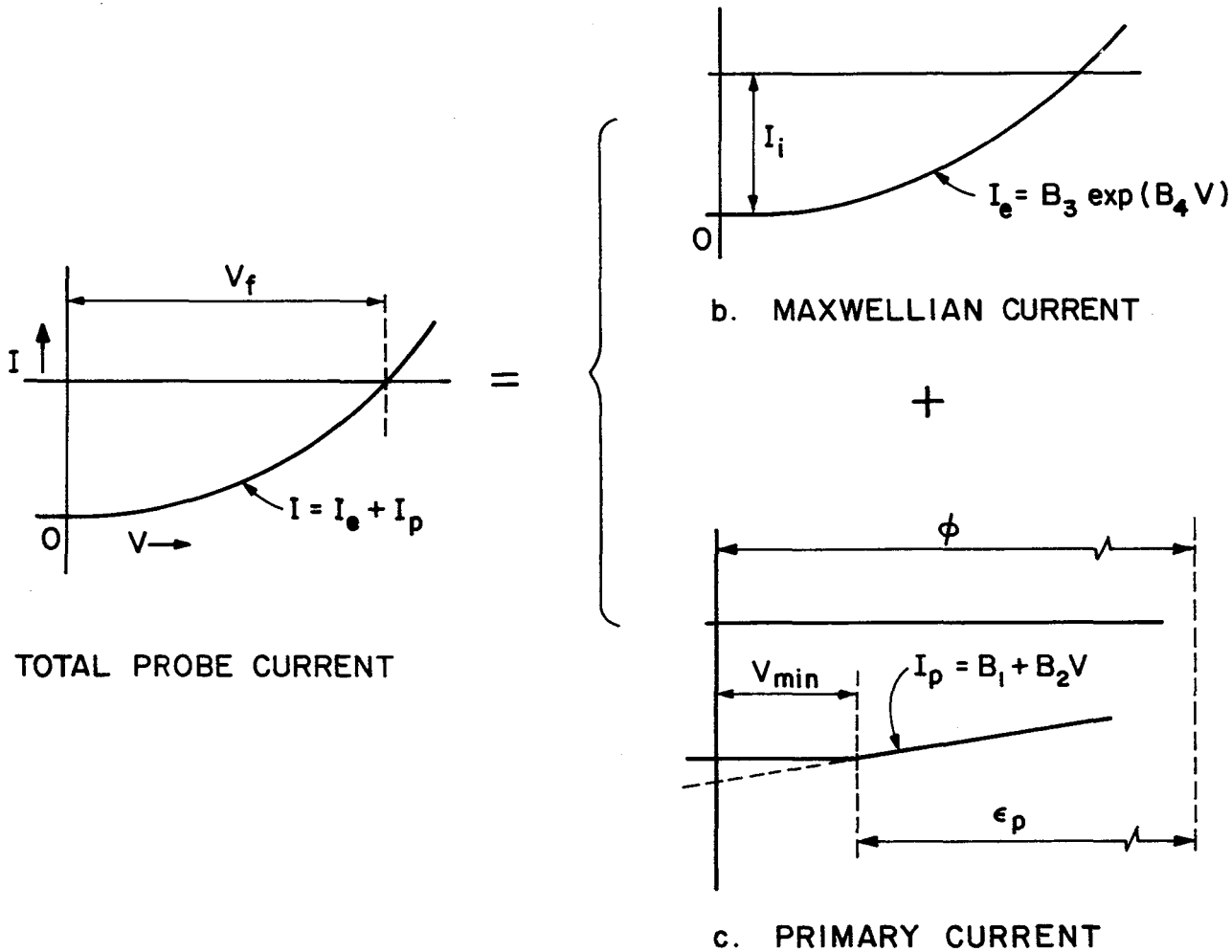

Figure C2. Probe Currents for Maxwellian plus Monoenergetic Electron Distribution.

are added five at a time until convergence is achieved). This provides an initial value for V_{min}. The data points at potentials below V_{min} are then modified by adding algebraically to each data point, the current

$$I_p = B_1 + B_2 V \quad \text{for } V < V_{min}. \tag{C2}$$

The portion added is shown as the dashed line in Figure C2c and effectively removes the discontinuity in the slope at V_{min}. With this modification of the original data, all of the data can then be curve fitted to Eq. C1. This provides a new value for $V_{min} = -B_1/B_2$. The original data is then modified using the new V_{min} and the procedure is continued until the change in the B's from one iteration to the next is less than a specified tolerance. If no initial V_{min} can be found or if the iteration procedure using the modified data does not converge, then the data is fit to the pure Maxwellian distribution function, that is

$$I_e = B_3 \exp(B_4 V) \quad . \tag{C3}$$

Once the values of the B's are determined, the plasma properties can be calculated from the following set of equations.

$$n_e = \frac{4B_3}{e\, \nu_{th} A} \exp\left[\frac{V_f\, \Delta\phi}{T_e}\right] \tag{C4}$$

$$\phi = V_f + \Delta\phi \tag{C5}$$

$$\varepsilon_p = (V_f + B_1/B_2) + \wedge\phi \tag{C6}$$

$$n_p = I_p(SAT)\left[\frac{e}{4}\right]\left[\frac{2\varepsilon_p}{m_e}\right]^{\frac{1}{2}}\left[1 - \frac{e\Delta\phi}{\varepsilon_p}\right]^{-1} \quad \text{where } I_p(SAT) = B_1 + B_2\phi \tag{C7}$$

$$\Delta\phi = -T_e\, \ell n\left\{\alpha\left[\frac{2\pi m_e}{m_i}\ \beta\right]^{\frac{1}{2}} - \frac{n_e}{n_p}\left(\frac{\pi\varepsilon_p}{4\,T_e}\right)^{\frac{1}{2}}\left(1 - \frac{e\Delta\phi}{\varepsilon_p}\right)\right\} \tag{C8}$$

$$\text{where} \quad \beta = \frac{1 + n_p/n_e}{1 + \left(n_p/n_e\right)\left(\frac{T_e}{2\varepsilon_p}\right)} \tag{C8}$$

The variables used in these equations are described in Table C1. The presence of the primary electrons makes the expression for $\Delta\phi$ (Eq. C8) transcendental in $\Delta\phi$. The computer program solves this equation using a simple iterative technique. Because n_e, ε_p, and n_p appear in Eq. C8, they must be updated at each iteration.

Table C1

List of Symbols for Analysis of Ion Saturation Langmuir Probe Trace

- A - Surface area of probe
- B's - Curve fit parameters
- e - Electron charge
- I - Probe electron current
- I_p - Primary electron current
- I_e - Maxwellian electron current
- I_i - Ion saturation current
- m_e - Electron mass
- m_i - Ion mass
- n_p - Primary electron density
- n_e - Maxwellian electron density
- T_e - Maxwellian electron temperature (B_4^{-1}) in eV
- V - Probe potential
- V_f - Floating potential
- ν_{th} - Random thermal electron velocity $\left\{\frac{8kT_e}{\pi m_e}\right\}^{\frac{1}{2}}$
- ν_B - Bohm velocity $\left\{\frac{kT_e}{m_i}\beta\right\}^{\frac{1}{2}}$ for ion arrival to electrode surface
- α - Bohm flux factor (1 for large probes and $\sim$ 0.6 for small ones) $I_i = ne\alpha\,\nu_B\,A$.
- β - Parameter indicating effect of primary electrons on Bohm velocity (Eq. C8)
- ε_p - Primary electron energy in eV

The computer program is set up to allow the monoenergetic electron current (I_p) to take on either positive or negative values. Figure C2 shows the positive case where a population of primary electrons has an energy ε_p. In this case, the energy distribution function for the Maxwellian plus primaries would appear as sketched in Figure C3a. Physically it is easy to imagine that the Maxwellian distribution might also be depleted of electrons at a specific energy due to the loss of electrons having this energy by a mechanism involving an inelastic reaction which has a very large cross-section at this energy. This can be handled effectively in the program by considering the population of monoenergetic electrons as having a negative electron current as shown in Figure C3b. Such a negative current, when added to the Maxwellian component, would be indicative of an energy distribution function such as the one shown in Figure C3c. Analysis of the cathode probe data using this program has shown that in many instances the data best fits the case where the monoenergetic group is negative indicating a Maxwellian population somewhat depleted of electrons at the energy associated with this group.

The preceding is just one possible physical explanation for a Langmuir probe trace suggestive of a non-Maxwellian population with an apparent depletion of electrons at a single energy. Other explanations could involve instrumentation impedance and cathode conditions such as a high neutral density. It should be noted here that the monoenergetic fraction of the electron population found in the cathode probe traces is quite small (on the order of a few tenth's of a percent). The only reason for being concerned about it here is that in dealing with the ion saturation portion of the probe trace this small percentage has a rather strong influence on the calculated Maxwellian temperature. It is therefore desirable to account

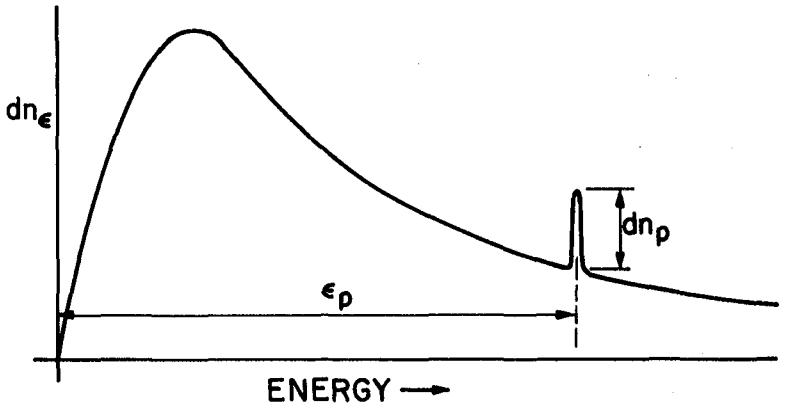

a. ENERGY DISTRIBUTION FUNCTION FOR MAXWELLIAN PLUS PRIMARY ELECTRONS.

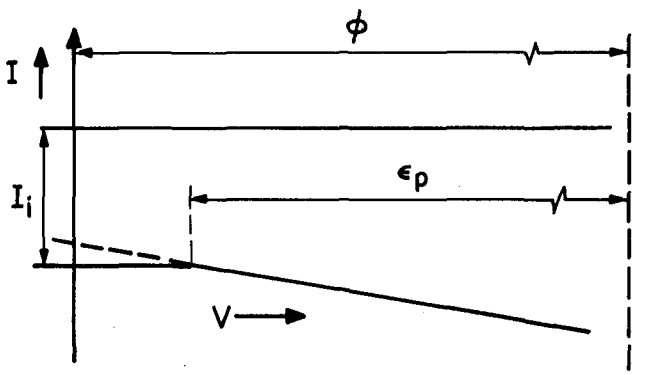

b. LANGMUIR PROBE CHARACTERISTIC FOR NEGATIVE PRIMARY ELECTRON CURRENT.

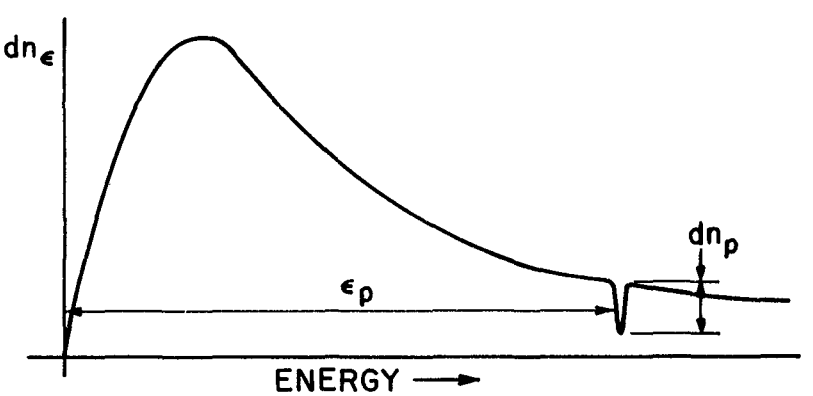

c. ENERGY DISTRIBUTION FUNCTION FOR MAXWELLIAN PLUS NEGATIVE MONOENERGETIC ELECTRONS.

Figure C3. Electron Characteristic Curves.

for this small fraction regardless of its physical cause.

A computer program using the curve fitting technique just described was also written to handle the conventional Langmuir probe traces. Because it does not drop any data points below V_{min}, this program could prove useful when dealing with standard Langmuir probe traces where the monoenergetic group has energies which are rather low with respect to the plasma potential. Listings of both versions of this program are available to anyone interested.

CLOSURE

Computer programs have been developed which will analyze either the full Langmuir probe characteristic or the ion saturation portion of the characteristic. These programs can fit the input data with either a pure Maxwellian distribution or a Maxwellian plus monoenergetic distribution. The programs have the advantage of being able to handle probe characteristics where the monoenergetic population is such that a significant amount of data would be lost if points less than V_{min} were dropped.

DISTRIBUTION LIST

	Copies
National Aeronautics and Space Administration Washington, DC 20546	
Attn: RS/Mr. Dell Williams, III	1
RTS-6/ Mr. Wayne Hudson	1
RTS-6/ Mr. Jerome Mullin	1
MT/ Mr. Ivan Bekey	1
National Aeronautics and Space Administration Lewis Research Center 21000 Brookpark Road Cleveland, OH 44135	
Attn: Research Support Procurement Section	
Mr. G. Golinski, MS 500-306	1
Technology Utilization Office, MS 3-19	1
Report Control Office, MS 5-5	1
Library, MS 60-3	2
Mr. N. Musial, MS 500-113	1
Dr. M. Goldstein, Chief Scientist, MS 5-3	1
Mr. T. Cochran, M.S. 501-7	1
Dr. F. Terdan, MS 501-7	1
Mr. R. Finke, MS 77-4	1
Mr. B. Banks, MS 11-4	1
Mr. D. Byers, MS 501-7	1
Mr. W. Kerslake, MS 501-7	30
National Aeronautics and Space Administration Lyndon B. Johnson Space Center Houston, TX 77058	
Attn: Mr. Hu Davis	1
National Aeronautics and Space Administration Marshall Space Flight Center Huntsville, AL 35812	
Attn: Mr. Jerry P. Hethcoate	1
Mr. John Harlow	1
Mr. Robert Bechtel	1
Research and Technology Division Wright-Patterson AFB, OH 45433	
Attn: (ADTN) Mr. Everett Bailey	1
NASA Scientific and Technical Information Facility P. O. Box 8757 Baltimore, MD 21240	
Attn: Accessioning Dept.	1

	Copies
Case Western Reserve University 10900 Euclid Avenue Cleveland, OH 44106 Attn: Dr. Eli Reshotko	1
DST 1 Ministry of Defence Metropole Building Northumberland Avenue London, WC2 N5BL ENGLAND Attn: Dr. D. G. Fearn	1
United Kingdom Atomic Energy Authority Culham Laboratory Abingdon, Berkshire ENGLAND Attn: Dr. P. J. Harbour Dr. M. F. A. Harison	1 1
National Aeronautics and Space Administration Goddard Space Flight Center Greenbelt, MD 20771 Attn: Mr. W. Isley, Code 734 Mr. A. A. Vetman Dr. David H. Suddeth	1 1 1
COMSAT Laboratories P. O. Box 115 Clarksburg, MD 20734 Attn: Mr. B. Free Mr. O. Revesz	1 1
Comsat Corporation 950 L'Enfant Plaza, SW Washington, DC 20024 Attn: Mr. Sidney O. Metzger	1
Rocket Propulsion Laboratory Edwards AFB, CA 93523 Attn: LKDA/Mr. Tom Waddell LKDH/Dr. Robert Vondra	1 1
DFVLR - Institut fur Plasmadynamik Technische Universitat Stuttgart 7 Stuttgart-Vaihingen Allmandstr 124 West Germany Attn: Dr. G. Krulle	1

	Copies
DFVLR - Institut fur Plasmadynamik 33 Braunschweig Bienroder Weg 53 West Germany Attn: Mr. H. Bessling	1
Giessen University 1st Institute of Physics Giessen, West Germany Attn: Professor H. W. Loeb	1
Jet Propulsion Laboratory 4800 Oak Grove Drive Pasadena, California 91102 Attn: Dr. Kenneth Atkins Technical Library Mr. Eugene Pawlik Mr. James Graf Mr. Dennis Fitzgerald Dr. Graeme Aston	1 1 1 1 1 1
Electro-Optical Systems, Inc. 300 North Halstead Pasadena, California 91107 Attn: Dr. R. Worlock Mr. E. James Mr. W. Ramsey	1 1 1
TRW Inc. TRW Systems One Space Park Redondo Beach, California 90278 Attn: Dr. M. Huberman Mr. Sid Zafran	1 1
National Aeronautics and Space Administration Ames Research Center Moffett Field, California 94035 Attn: Technical Library	1
National Aeronautics and Space Administration Langley Research Center Langley Field Station Hampton, Virginia 23365 Attn: Technical Library Mr. B. Z. Henry	1 1

	Copies
Hughes Research Laboratories 3011 Malibu Canyon Road Malibu, California 90265	
Attn: Mr. J. H. Molitor	1
Dr. R. L. Poeschel	1
Dr. Jay Hyman	1
Dr. J. R. Beattie	1
Dr. W. S. Williamson	1
Dr. H. J. King	1
Princeton University Princeton, NJ 08540	
Attn: Mr. W. F. Von Jaskowsky	1
Dean R. G. Jahn	1
Dr. K. E. Clark	1
Joint Institute for Laboratory Astrophysics University of Colorado Boulder, Colorado 80302	
Attn: Dr. Gordon H. Dunn	1
Boeing Aerospace Co. P. O. Box 3999 Seattle, Washington 98124	
Attn: Mr. Donald Grim, M.S. 8K31	1
Mr. Russell Dod	1
Lockheed Missiles and Space Co. Sunnyvale, California 94088	
Attn: Dr. William L. Owens Propulsion Systems, Dept. 62-13	1
Fairchild Republic Co. Farmingdale, New York 11735	
Attn: Dr. Domenic J. Palumbo	1
Electrotechnical Laboratory 1-1-4, Umezono, Sakura-Mura, Niihari-Gun Ibaraki, Japan	
Attn: Dr. Katsuya Nakayama	1
Bell Laboratories 600 Mountain Avenue Murray Hill, NJ 07974	
Attn: Dr. Edward G. Spencer	1
Dr. Paul H. Schmidt	1

Copies

Sandia Laboratories
Mail Code 4537
Albuquerque, NM 87115
Attn: Mr. Ralph R. Peters 1

Ion Tech, Inc.
P. O. Box 1388
1807 E. Mulberry
Fort Collins, Colorado 80522
Attn: Dr. Gerald C. Isaacson 1

EG & G Idaho
P. O. Box 1625
Idaho Falls, Idaho 83401
Attn: Dr. G. R. Longhurst, TSA-104 1

The Aerospace Corporation
P. O. Box 95085
Los Angeles, CA 90045
Attn: Dr. B. A. Haatunion 1
Mr. A. H. Silva 1

Michigan State University
East Lansing, MI 48824
Attn: Dr. J. Asmussen 1
Dr. M. C. Hawley 1

General Dynamics
Kearney Mesa Plant
P. O. Box 1128
San Diego, CA 92112
Attn: Dr. Ketchum 1

Ford Aerospace Corp.
3939 Fabian Way
Palo Alto, CA 94303
Attn: Mr. Robert C. Kelsa 1

Hughes Aircraft Co.
Space and Communication Group
P. O. Box 92919
Los Angeles, CA 90009
Attn: Dr. M. E. Ellison 1
Dr. B. G. Herron 1

The Aerospace Corporation
Space Sciences Lab.
P. O. Box 92957
Los Angeles, California 90009
Attn: Dr. Y. T. Chiu 1

	Copies
The Takagi Research Laboratory Department of Electronics Kyoto University Yoshidahonmachi Sakyo-ku Kyoto 606 JAPAN Attn: Dr. Toshinori Takagi	1
Department of Aeronautics Faculty of Engineering University of Tokyo 7-3-1, Hongo, Bunkyo-ku Tokyo, JAPAN Attn: Prof. Itsuro Kimura	1
Prof. Tom Maul P. O. Box 98182 Tsim Sha Tsui Post Office Kowloon, Hong Kong British Crown Colony	1
Mr. Susumu Masaki Department of Electronics Tokyo National Technical College No. 1220-2 Kunugida-cha, Hachioji 193 Tokyo, JAPAN	1
Mr. Curtis Haynes Tektronix Inc. M.S. 50-431 P. O. Box 500 Beaverton, Oregon 97077	1
Dr. Pradosh Ray Tuskegee Institute School of Engineering Tuskegee Institute, Ala. 36088	1
Dr. John Barber International Applied Physics Inc. 7546 McEwen Road Dayton, Ohio 45459	1
Dr. Ron Hawke Lawrence Livermore Laboratory Livermore, California 94550	1
Dr. Richard A. Marshall University of Texas Taylor Hall 167 Austin, Texas 78712	1

	Copies
Dr. V. V. Zhurin Computing Center of the USSR Academy of Sciences Vavilova 40 117333 Moscow, B-333 USSR	1
Dr. M. Krishnan Dept. of Applied Physics P. O. Box 2159 Yale Station New Haven, Connecticut 06520	1
Mr. John Brophy G.S. 91P Martin Marietta Corp. P. O. Box 1681 Vandenburg AFB, CA 93437	1
Lt. Phil Roberts AFRPL/LKDH, M.S. 24 Edwards Air Force Base CA 93523	1
Dr. Ed Goldman Physics International Co. 2700 Merced Street San Leandro, CA 94577	1